Universidade de Lisboa
Faculdade de Ciências
Departamento de Física

Demosaicing Multi-Energy Patterned Composite Pixels for Spectral CT

Iva Margarida Vilas-Boas Ribeiro

Mestrado Integrado em Engenharia Biomédica e Biofísica
Perfil em Engenharia Clínica e Instrumentação Médica

Dissertação orientada por:

Prof. PhD Yannick Boursier, CPPM, Aix-Marseille Université, CNRS/IN2P3, Marselha, França
Prof. PhD Nuno Matela, Departamento de Física, Faculdade de Ciências da Universidade de Lisboa, Lisboa, Portugal

2016

Abstract

Computed Tomography is a diagnosis technique that uses X-ray radiation to create images of structures. This technique consists in reconstructing a quantitative map of the attenuation coefficients of the object sections from multiple projections using reconstruction algorithms. Since the attenuation coefficient is not unique for any material, the differentiation and classification of different tissue types by Computed Tomography has revealed to be extremely challenging. The solution has been provided through the development of an energy sensitive CT scanner, known as Spectral CT. This technique takes in consideration that the transmitted radiation carries more information than intensity changes, that the x-ray tube produces a wide range of energy spectrum and that the attenuation of radiation depends not only on the material but also on the photon energy. Spectral CT uses the attenuation characteristics at more than two energies which makes it possible to differentiate various elements in the body, based on their material density or atomic numbers. Therefore, this technique uses the new detector technology, the hybrid pixel detector. This detector allows the energy threshold setting. Combining the physical properties of different materials and the possibility of setting the energy threshold in the detectors, a new spectral imaging technique is used, K-edge imaging. This technique explores the discontinuity in the photoelectric effect, which is generated when photons interact with matter, and those interact with the shell electrons. Therefore, the Centre de Physique des Particules de Marseille developed a micro-CT and a simultaneous PET/CT scan based on hybrid pixel detector. The ability of tuning the energy threshold of each pixel independently was exploited to develop K-edge imaging and the proof of concept has been established on phantom and on living mice. In the context of pre-clinical imaging, objects are moving and the several acquisitions must be performed simultaneously to allow the registration set. For this purpose, CPPM had been working with composite pixels made of 9 (3× 3) pixels with 3 different thresholds. This solves the motion artefact problem at the price of loss in spatial resolution. Therefore, the research project of this work aims at performing K-edge imaging on moving object at full spatial resolution. The problem is seen as an Inpainting problem where unknown measure must be estimated from partial measurements. A huge literature exists in the Inpainting, and especially in the field of Demosaicing, which is particularity of interest in this research project. The project consists in a study of the sampling scheme of spectral CT images and to evaluate the performance of simplest methods with respect to noise and spatial resolution. More sophisticated techniques of Inpainting and Demosaicing were tested, which were developed specifically for spectral CT images by incorporating prior on image. Therefore, an evaluation performance of all the reconstruction methods was successfully made, and a state-of-art was established. In this research project, in order to create the composite pixels concept, a set of dynamic strategies of patterning composite pixels was achieved in order to define optimal protocols of acquisition.

keywords: Inpainting, Demosaicing, Image reconstruction, Spectral CT, hybrid pixel detectors, K-edge imaging

Resumo

O desenvolvimento da Tomografia Computadorizada foi realizada na combinação de duas áreas científicas, computação e imagiologia com base em raios-x. Em 1895, o cientista Wilhelm Roentgen descobriu os raios-X: fotões de altas energias provenientes de transições eletrónicas nos átomos. Estes são radiações eletromagnéticas que se propagam à velocidade da luz e são ionizantes. Devido às suas propriedades, os raios-x foram imediatamente rentabilizados como uma ferramenta para explorar a composição da matéria. Os fotões interagem com a matéria por dois mecanismos dominantes, dependendo da energia da radiação eletromagnética: efeito fotoelétrico e efeito de Compton.

O efeito fotoelétrico corresponde à interação dos fotões com os eletrões que se encontram nas órbitas de maior energia do átomo. O fotão transfere toda a sua energia para o eletrão, sendo parte dessa usada para superar a energia de ligação do eletrão e a energia restante é transferida para o mesmo eletrão sob a forma de energia cinética.

O efeito de Compton corresponde à interação do fotão com o eletrão que se encontra numa das órbitas de menor energia. Depois da interação, o fotão é desviado e o eletrão é ejetado do átomo. O fotão desviado pode voltar a interagir com a matéria sob o efeito de Compton ou o efeito fotoelétrico, ou simplesmente não a interagir com a matéria.

Os raios-X têm a sua intensidade diminuída em função das interações que ocorrem com o material que as absorve. A atenuação da energia destes acontece de maneira exponencial em função da espessura do material absorvente. Devido às propriedades físicas provocadas pelos raios-X, esta radiação foi estabelecida como uma ferramenta médica.

A tomografia convencional consistiu numa técnica de diagnóstico na qual a aquisição de imagem é realizada a partir de um filme radiográfico, que resulta da projeção das estruturas anatômicas tridimensionais em imagens bidimensionais, com sobreposições de informação anatómica. Em 1970, os cientistas Hounsfield e Cormack desenvolveram uma técnica, a Tomografia Computadorizada, que possuía logo de início a vantagem de corrigir o problema da sobreposição de informação. A Tomografia Computadorizada reconstrói as estruturas internas de um objeto a partir de múltiplas projeções utilizando algoritmos de reconstrução. A diferenciação e classificação de diferentes tipos de tecidos tornou-se extremamente desafiante nesta técnica, devido ao facto de que mesmo que dois materiais difiram em número atômico, dependendo da densidade de massa ou concentração, eles podem aparecer idênticos na imagem. Desta forma uma das soluções foi o estudo da Tomografia Computorizada Espectral, sendo esta uma técnica promissora no desenvolvimento da imagiologia pois potencia a deteção e caracterização dos tecidos anatómicos além dos níveis atualmente atingíveis com técnicas de TC convencionais. A TC espectral leva em consideração que a radiação transmitida transporta mais informações para além de mudanças de intensidade e que o coeficiente de atenuação depende não só do material, mas também da energia do fotão. A TC espectral difere das outras técnicas no sentido em que utiliza as características físicas dos materiais em estudo em mais de dois espectros de energia. Através da aquisição de imagens em diferentes níveis de energia, a técnica é capaz de diferenciar os vários elementos do corpo com base na densidade dos materiais ou nos números

atômicos destes. As diferenças entre os vários tecidos são exibidas através de distintas cores na imagem final.

Uma tecnologia importante utilizada na CT Espectral é a dos detetores de contagem de fotões, conhecidos por detetores híbridos. Estes detetores têm a particularidade de separar o espetro incidente em múltiplos espetros, cuja forma depende dos limiares de energia impostos. Estes detetores operam num modo de contagem, ou seja, em vez de operarem em modo de integração tal como os detetores convencionais, estes efetuam a contagem individual dos fotões da radiação incidente a partir de limiares de energia estipulados. A influência do ruído eletrónico afeta a energia medida de cada fotão, contudo tendo em conta que estes detetores efetuam a contagem de fotões, o ruído eletrónico deixa de ter uma influência tão significativa na qualidade da imagem adquirida.

"K-edge Imaging" é uma das abordagens utilizadas em sistemas de TC espectral; explora as propriedades físicas de agentes de contrastes utilizados em tomografia computorizada e as suas respetivas propriedades físicas. Os elementos utilizados para os agentes contrastes são elementos pesados e altamente atenuantes, e cujo efeito fotoelétrico ocorre ao mesmo alcance das energias utilizadas em TC. Deste modo, cada um desses elementos pesados tem um salto característico na sua atenuação de raios-X, o qual corresponde à energia que ocorre o efeito fotoelétrico. Como os eletrões envolvidos no efeito fotoelétrico pertencem à orbital K, o salto característico é designado por "K-edge". "K-edge Imaging" explora a escolha do espetro de energia aplicado de forma a abranger o salto característico destes elementos para identificar e localizar componentes específicos.

No CPPM, o grupo imXgam desenvolveu uma micro-TC e uma PET / TC simultânea que incorpora a nova tecnologia de detetores híbridos desenvolvida pelo centro: o detetor XPAD3. Esta tecnologia não só permite trabalhar em modo de contagem de fotões, mas também é capaz de selecionar informação energética sobre os fotões detetados; consequentemente as capacidades do detector XPAD3 foram exploradas para desenvolver "K-edge Imaging".

Os artefactos que resultam de várias aquisições estão relacionados com o movimento. Para resolver esse problema, o CPPM desenvolveu um conceito de píxeis compostos, que consiste numa matriz de píxeis (3×3) com 3 diferentes limiares de energia. Embora, os píxeis compostos resolvam os artefactos de movimento, as imagens adquiridas perderam a resolução espacial. Assim, o projeto deste trabalho tem como objetivo a realização de "K-edge Imaging" em objetos em movimento em plena resolução espacial. Este projeto aborda o problema como um problema "Inpainting", onde as medidas desconhecidas para cada limiar de energia serão estimadas a partir de medidas parciais. Há uma vasta literatura sobre o problema "Inpainting", assim como noutra área de processamento de imagem, o "Demosaicing". Estes são métodos de restauração que removem regiões danificadas ou reconstroem porções perdidas da imagem. O problema "Demosaicing" tem um interesse particular para este trabalho em virtude do método recuperar informação de imagens coloridas (imagens RGB).

A utilização do método "Demosaicing" em imagens adquiridas por sistemas TC é praticamente inexistente, pelo que o objetivo deste projeto foi avaliar não só os métodos de restauração convencionais, mas também adaptar e avaliar o método "Demosaicing" às imagens adquiridas por sistemas TC. Desta forma, as imagens espectrais foram tratadas como imagens coloridas: cada imagem adquirida por um limiar de energia foi configurada como uma cor. A imagem resultante foi submetida ao processo de recuperação que consistiu em acoplar as três imagens obtidas por cada limiar de energia em uma imagem de cor(imagem RGB).

Este trabalho exigiu, em primeiro lugar, o estudo do esquema de amostragem de imagens espectrais e a avaliação de desempenho dos métodos mais simples em relação ao ruído, ao fator de subamostragem e à resolução espacial. As técnicas mais sofisticadas como a "Inpainting" e "Demosaicing" foram desenvolvidas e avaliadas especificamente para imagens espectrais tomográficas. Após a avaliação destas, foi realizado um "estado de arte" que comparou os métodos e, consequentemente, fez uma análise de qual o método mais adequado para imagens de TC espectral.

A segunda parte deste projeto consistiu no estudo do padrão que os píxeis compostos devem seguir, de forma a definir um protocolo de aquisição. Para tal, foram testados dois tipos de padrões: regular e aleatório. A ideia de píxeis compostos foi obtida criando uma matriz com vários componentes que dependem do número de limiar de energias que se quer utilizar. Conforme mencionado, no CPPM é utilizado uma matriz de pixels com três limiares de energia, desta forma, neste projeto, a possibilidade de aumentar o número de limiares de energia foi também testado.

Os objetivos do projeto foram alcançados uma vez que a avaliação dos métodos foi realizada e conclui-se que a nova abordagem apresentou melhores resultados que os métodos padrão. Conclui-se que as imagens adquiridas pelo método "Demosaicing" apresentam melhor resolução espacial. Relativamente ao padrão dos píxeis compostos verificou-se que em ambos a reconstrução apresentou bom desempenho. A análise do aumento de número de limiares de energia apontou para bons resultados, observados no uso de 4 níveis de energia, porém a nova abordagem "Demosaicing" teria de ser reformulada.

De forma a alcançar os objetivos, este tema foi dividido em vários capítulos. No segundo capítulo foram introduzidos os conceitos físicos envolvidos na tomografia espectral, desde a produção dos raios-X até ao desenvolvimento da técnica propriamente dita. O terceiro capítulo abordou como o "estado de arte" foi efetuado, documentando o que foi realizado atualmente no campo em estudo. Nos capítulos 4 e 5 apresentou-se os materiais e métodos utilizados, assim como exposto as suas aplicações,e de forma mais particular a matemática e a programação envolvidas. No capítulo 6 apresentou-se os resultados alcançados e as respectivas observações. No último capítulo sumariou-se os resultados obtidos e as conclusões retiradas a partir destes.

Palavras-chave: Tomografia Computorizada Espectral, "Demosaicing", "Inpainting", reconstrução de imagen, Detetores Híbridos, Detetores de contagem, "K-edge Imaging"

Acknowledgements

First and foremost, I would like to express my gratitude to both my supervisors. I wish to thank most sincerely to Yannick Boursier for engaging me in new ideas, demanding a high quality of work and patiently encouraging me to improve my skills. I am extremely thankful to Mathieu Dupont for helping me and sharing his computing knowledge with me, and specially for solving some computing problems that I had along the internship. I am very happy to say that for the last 6 months my experience under their supervision has been not just academically rewarding but also intellectually exciting and fun.

I wish to thank my internship program coordinator, Nuno Matela for all the support, comments and involvement throughout this learning process.

My sincere thanks to Isabell Bones for the advice and for all the useful discussions concerning my project. I wish to thank all Centre de Physique des Particules de Marseille colleagues for their welcome and pleasant work atmosphere.

Finally, I would like to thank all my friends from Portugal, and especially all the new people that I met in Marseille, who contributed to make this internship a rewarding life experience.

Last but not least, to my family for their unconditional love and support, especially to my mother.

Contents

List of Tables

List of Figures

List of Abbreviations

kVp	Peak kilovoltage
keV	kilo-electronvolt
ML-EM	Maximum-Likelihood Expectation Maximisation
CT	Computed tomography
DECT	Dual-energy computed tomography
CPPM	Centre de Physique des Particules de Marseille
FS	Frequency selection
TV	Total variation
L.Int.	Linear Interpolation method
In. TV	Inpainting Total Variation method
In. Sobo	Inpainting Sobolev method
Dem. FS	Demosaicing by frequency selection
Dem. TV	Demosaicing by Total Variation minimization

Chapter 1

Introduction

Since x-ray is an electromagnetic radiation, it was immediately associated as a tool to explore the matter composition of different materials. Computed tomography consists in reconstructing the internal structure of an object from multiple projections using reconstruction algorithms. The differentiation and classification of different tissue types is extremely challenging, due the fact that even though two materials differ in atomic number, depending on the mass density or concentration, they can appear identical.

The solution has been provided through the advancement of spectral imaging. This research field led to the development of the energy sensitive CT scanner. Spectral CT takes in consideration that the transmitted radiation carries more information than intensity changes, that the x-ray tube produce a wide range of energy spectrum and that the attenuation of radiation depends not only on the material but also on the photon energy. Spectral CT differs from the other techniques in the sense that it uses the attenuation characteristics at more than two energies, and within narrow energy ranges. By acquiring images at different energy levels, the technique is able to differentiate the various elements in the body based on their material density or atomic numbers.

An important technology used in Spectral CT is photon counting detectors that separate the incident spectrum into multiple binned spectra whose shape depends on the energy threshold setting of the pulse height analyser. Hybrid pixel detectors are a type of photon counting detector that allows the energy threshold setting. The choice of thresholds is done according to the knowledge of physical characteristics of the tissues in analysis. Therefore, K-edge Imaging is one of the approaches used in spectral CT systems, where more than three measurements for each voxel are acquired. This approach explores the discontinuity in the photoelectric effect. This discontinuity is generated when photons interact with matter, and those interacting with the shell electrons. Photons will be attenuated when electrons are freed in the lowest energy shell of the absorber. The lowest energy shell is called by K-shell.

The simultaneous PET/CT scan developed at Centre de Physique des Particules de Marseille is based on a new technology of x-ray camera named hybrid pixel XPAD3 camera. The hybrid pixel detectors are the new generation of detectors used in computed tomography. This technology not only allows to work in photon counting mode but it is also able to capture some energy information on the detected photons. Hybrid pixel detectors have the particularity of denying the dark noise, which provides a better signal-to-noise ratio. The collection of energy information is made by tuning the energy threshold of each pixel independently, which is the

minimum energy that a photon has to carry in order to be counted.

Therefore, the capabilities of XPAD3 detector have been exploited to develop K-edge imaging. As explained, K-edge imaging performs several acquisitions at different energy thresholds in order to identify and localize specific components, i.e contrast agents as Iodine or silver.

One image artefact that result from performing several acquisitions simultaneously is related to the structure movement. To solve this problem, CPPM developed a composite pixels concept, which consists in a pixel matrix (3×3) with 3 different energy thresholds. The studies made showed that the use of composite pixels reduce the absorbed dose for longitudinal biological studies on small animals and make K-edge imaging more robust with regards to animal positioning. Although, composite pixels made possible to reduce the dose and solve the motion artifacts, the images acquired lost spatial resolution.

Thus, the research project of this work aims at performing K-edge imaging on moving objects at full spatial resolution. The problem that this research project approaches is seen as an inpainting problem, where unknown measures, for each energy threshold will be estimated from partial measurements. There is a huge amount of literature on the inpainting problem, as in the field of the so called demosaicing problem. Inpainting problem are restoration methods that remove damage regions or reconstruct missing portions of image. The Demosaicing probem has a particular interest for this work due the fact that the method recovers missing information from coloured images, RGB images. Both methods are seen as inverse problems that consist in filling in missing blocks in the images by predicting values of the missing data. Demosaicing problem, as mentioned, is seen as a reconstruction method for coloured images, the particularity of using this methods in the aim of this project is that the tomographic images acquired by each energy threshold will be treat as colored image, and therefore the resulted image will be a color tomographic image, RGB color.

This work required first the study of sampling scheme of spectral CT images and the performance evaluation of the simplest methods with respect to noise and spatial resolution. Therefore, more sophisticated techniques as inpainting and demosaicing will be tested, and will be developed specifically for spectral CT images by incorporating prior on images, i.e smoothness. After the evaluation of the image reconstruction techniques, a state-of-art is accomplished which compares the methods, and consequently makes an analysis of which method is more suitable for spectral CT images.

Therefore, the dynamic strategies of patterning composite pixels will be studied in order to define optimal protocols of acquisition. For this purpose, two types of patterns were tested, a regular and random pattern, for all the reconstruction methods. The idea of composite pixels was accomplished by creating a matrix with several channels, which depends on the number of energy threshold, and it is named mask. In addition to the study of the patterns of composite pixels, the analysis of number of different thresholds was also made. As mentioned, at CPPM a pixel matrix with 3 different thresholds is used nowadays, in this project, the possibility of increasing the number of energy thresholds was also investigated. Thus, for each possibility of energy threshold number, the reconstruction methods were tested and a performance evaluation was made in order to ponder if it was suitable to apply in spectral CT images.

K-edge imaging using composite pixels and reconstruction methods to perform better spatial resolution was successfully achieved with three energy thresholds settings. This way, in order to achieve these results and conclusions, this project was divided into 7 chapters.

In the second chapter, several concepts are introduced in order to understand the opera-

tion of the Spectral CT. Thus, the physic concepts and the technology involved in Computed tomography are described. Chapter 2 will conclude with Spectral CT, where dual-energy CT will be explained as an introduction and explanation of how Spectral CT started being used.

In Chapter 3, the Spectral CT approaches developed until now will be presented, followed by the explanation of the Spectral CT system used at CPPM and, therefore the studies made concerning K-edge imaging and composite pixels. Chapter 4 presents the materials used in this research, and begins with the description of the micro-CT developed at CPPM, in order to follow how the spectral CT images were acquired. In this section, the hybrid pixel detector developed at CPPM is described. Chapter 4 finishes with the masks and images that were used to simulate the composite pixels concept, and how they were applied in this project.

Chapter 5 will be used to describe the reconstruction methods used to recover missing information, including the mathematical formulations. In this chapter, the several evaluation parameters are presented. Afterwards, the experimental procedure is demonstrated, which explains the main steps this work consists of. The results achieved are presented in Chapter 6, and they are divided in five sections. The first section presents the reconstruction methods performance with the increasing of energy thresholds. The two following sections present the study of the reconstruction methods, each section will correspond to a specific composite pixel pattern. The fourth and fifth section consist in the comparison of the composite patterns and the analysis of the images, respectively. Finally, chapter 7 presents the conclusion of this research project. This includes the difficulties that had to be overcome and the possible applications that the use of this reconstruction techniques have in Spectral CT.

Chapter 2

Computed Tomography

X-ray radiation is a form of high energy electromagnetic radiation. This radiation results from the vibrations of electric and magnetic fields, whose velocity propagation is equal to the speed of light. Since x-ray radiation is an electromagnetic radiation, the processes involved in the radiation appearance are the energy quantum transitions, the acceleration of electric charges. The X-ray beam can be seen as a displacement of small amounts of energy (quanta) progressing at the speed of light. This small amount of energy is called photons.

Although certain basic properties are common to all electromagnetic radiation, the range of spectrum frequencies is so large that individual chemical-physical characteristics of different types of radiation and its impact on man are essentially different. The x-ray radiation belongs to a radiation group where the photon energy is above 11 eV, thus allowing the ionization of biological structures. X-ray radiation was discovered in 1895 by the scientist Wilhelm Roentgen. Wilhelm Roentgen was working on the effect of cathode rays, when he observed that certain rays were emitted during an electrical discharge. After verifying that when a current was applied to partially evacuated glass tube, the screen covered in fluorescent material became illuminated, [2], Roentgen reckoned that the fluorescence had to be caused by the radiation produced by its experiment, [12]. Wilhelm Roentgen called the radiation "x rays" and immediately concluded that the new radiation could penetrate various materials and could be recorded on photographic plates.

2.1 X-ray Production

The x-ray tube is the structure where the x-radiation is produced. All the tube components are contained within an evacuated vessel and are surrounded by a lead shield with a glass window, through which the X-ray beam is emitted. This structure has a cathode, which is the negative end, and an anode, which is the positive end of the x-ray tube, [12]. The cathode acts as the source of the electrons, and consists of a small helix of thin tungsten wire. To form an anode, a large positive voltage is applied to a metal target.

X-ray radiation is produced by the acceleration of a beam of high energy electrons allowing them to collide with a metal target. An electric current is passed through the negatively-charged cathode which will increase its temperature providing enough energy for the electrons to leave the metal surface. A potential difference between the anode and the cathode is applied, in such

way that the electrons produced at the cathode are attracted to the anode. The collision between charged particles and matter will produce energy with a continuous and discrete spectrum. A big percentage of the energy release by the collision is heat energy and just a small fraction is emitted as electromagnetic radiation, x-ray radiation.

2.1.1 X-ray Tube Spectrum

X-ray radiation is produced when the electrons are accelerated into a metallic target. The impact of the electron beam with the anode will produce x-rays with a wide range of energies, up to a maximum value given by the kVp.

The spectrum of x-ray radiation leaving the x-ray tube has a spectrum similar to that shown in **Figure 2.1** which shows the graphic representation of the relative number of x-rays produced as a function of their energy.

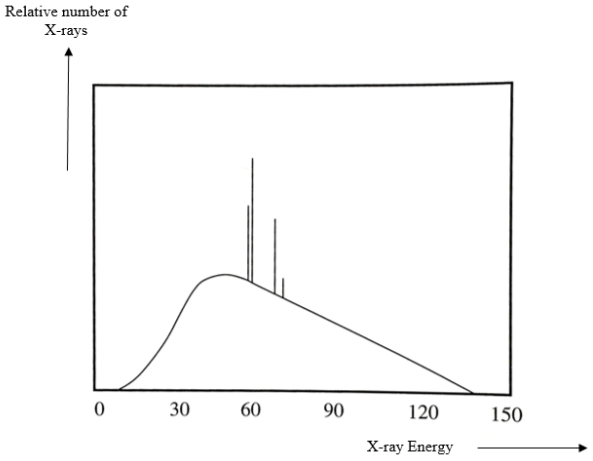

Figure 2.1: Energy spectrum of a beam emitted from an X-ray tube with a tungsten anode operating at 140 kV,[1]

X-rays are produced by two different mechanisms, one that results in a expansive spread of energies, and the other which produces distinct sharp lines, as demonstrated in **Figure 2.1**. Therefore, the impact of the accelerated electron beam from the cathode to the anode produces two types of radiation: Bremsstrahlung radiation and X-ray characteristic [13] [2].

The Bremsstrahlung radiation is produced by the deceleration of electrons. This phenomenon is responsible for the continuous part of the spectrum, and it happens due to the loss of kinetic energy from electrons passing close to the nucleus of a metal atom forming an anode. The electron kinetic energy loss that results from the deflection is converted into an X-ray called bremsstrahlung photon. The energies of the emitted photons depend on the atomic number of the nucleus, the distance of the electron-nucleus interaction and the kinetic energy of the electrons [2].

Sharp peaks are also presented in the X-ray energy spectrum, and the energy at which those occur will depend on the metal used in the anode, hence the name being characteristic radiation. The characteristic radiation is produced when the high speed electrons that come from the anode collide with one of the inner shell electrons of the metal target, and liberate an electron. The electron accelerated from the cathode collides with a tightly bound K-shell

electron in the anode, this bound electron is ejected and the resulting vacancy in the K-shell is filled by an electron from an outer shell.

The collision with electrons of the inner layers of the anode atoms produce ionization or excitation. An accelerated electron collides with a tightly bound K-shell electron, therefore an orbital electron is ejected. Then, an electron comes to occupy a higher energy level in the atom. The atom become unstable and an electron from one of the layers of greater potential energy will jump to the resulting vacancy collision, releasing a photon.

The difference between the binding energies of two shells is emitted as a single X-ray with a specific energy. The energies of the different peaks occurring in the spectrum are due to the various possibilities of interaction with the nearest core electrons, and these peaks are characteristic from the atomic that constitutes the anode. The characteristic X-ray from an L-to-K electron transition has an energy of 59 keV and from M-to-K transition an energy of 67 keV, which are represented by the sharp peaks of **Figure 2.1**.

2.2 Interaction with Matter

Diagnostic Radiology is interested in the effects on the tissues generated by their interaction with an X-ray beam, and the possible undesirable effects of radiation. This energy transfer between the photons and atoms from the absorbing medium, takes place according to various interaction processes which result in differences in attenuation that modulate the emerging intensity. The interactions with the surrounding material occur with orbital electrons. The diagnostic energy range used in Computed Tomography is between 50-150 keV and in the next section it will be demonstrated which interactions are considered for diagnostic purposes, [13] [12].

Photons are electrically neutral, unlike charged particles, and the type of interaction that they will have with atom is governed statistically by a probability of interaction per unit distance travelled, which depends on the medium traversed and on the photon energy.

Thus, when a photon interacts with a material medium, there are several mechanisms of interaction that can occur, of which the three most important are: Photoelectric Effect, Compton Effect and Pair Production. In all three cases occurs energy transfer to the electrons. The probability of occurrence of each one of these processes is determined by its cross section, which depends on the photon energy and the density and atomic number of material through which it interacts.

The interaction of a photon with a material results in energy transfer from the photon to the electron of the irradiated material. For energies lower than 100 keV, the interaction that is dominant is the photoelectric effect. In the range of incident radiation whose energy is ≥ 1 MeV the effect that dominates is the Compton effect. This effect is the deviation suffered by the interaction between a photon and an electron. For radiation with high energy $\gg$ 1MeV the effect that is predominant is the production of pairs, which occurs to very high energies and will not be described further.

Therefore, the interactions between photons and the material that will be explained and taken into consideration are the photoelectric and Compton effect.

2.2.1 Photoelectric effect

The photoelectric effect is a phenomenon in which the photons interact with an atom by withdrawing an electron out of the atom orbital. Energy from the incident X-ray is absorbed by the tissue, with a bound electron being emitted from the K-shell or L-shell. The ejected electron has an energy equal to the difference between the energy of the incident X-ray and the binding energy of the electron,[14]. The kinetic energy of the photoelectron is represented in the **equation 2.1**, which E_i is the energy of the incident photon and E_l is the binding energy of the orbital electron in the atom.

$$E_c = E_i - E_l \tag{2.1}$$

The photoelectric absorption occurs when the incident photon energy is greater or equal to the binding energy of the electron that will be ejected. The energy E_c is absorbed by successive photoelectron interactions with the environment, which is the kinetic energy transferred to the photoelectron. The contribution of different energy levels in the photoelectric effect is very uneven, being the highest the one that corresponds to the most bound electrons, which are the electrons of the K and L shells.

Following the photoelectric interaction, a non-saturated shell is created. Therefore, the atom is ionized with an inner shell electron vacancy. A higher orbital order electron comes to occupy the vacancy, creating in turn a new non-saturated shell. This shell will be filled by an electron belonging to an even lower binding energy shell. Meanwhile, the difference in binding energy levels is released as characteristic x-rays or auger electrons.

Attenuation and Absorption in Photoelectric effect

The probability of photoelectric interaction decreases rapidly as the photon energy increases. In general, the mass attenuation coefficient of photoelectric absorption (τ) varies with $1/E^3$. The mass attenuation coefficient is related to the atomic number, atomic mass of the tissue, and to the incident photon energy. In the diagnostic energy range up to 150 keV, the photoelectric effect cross-section per atom is given approximately by **equation 2.2**.

$$\sigma_{ph}(E) \propto \frac{Z^4}{E_0^3} \quad , \in [4,5] \tag{2.2}$$

Where Z is the atomic number and E_0 is the incident photon energy.

The probability of the photoelectric interactions decreases with the increasing of the photon energy, however there is an exception. For every element, a graph of the coefficient τ, as a function of photon energy, exhibits sharp discontinuities called absorption edges.

As stated, when the photon's energy is greater than the binding energy of the atomic shell, a photon undergoes the photoelectric interaction. The photon energy corresponding to an absorption edge is the binding energy of the electrons in that particular shell. This edge is described by the letter that represents the atomic shell of the electron (K,L,M,N). Therefore, when the photon energy increases, a given energy value E_l is exceeded, and the attenuation

coefficient increases sharply because now interactions may occur with electrons of the energy level E_l. Since this process is very significant for high-Z material in the diagnostic energy range, the absorption edge will be called K-edge.

Figure 2.2 presents the graphic representation of the photoelectric mass attenuation coefficients for several elements as a function of energy.

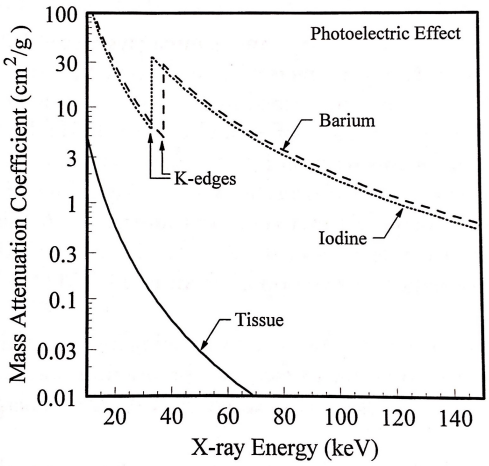

Figure 2.2: Photoelectric mass attenuation coefficients for tissue (Z = 7), iodine (Z = 53), and barium (Z = 56) as a function of energy. [2]

2.2.2 Compton effect

The Compton effect or Compton scattering is an elastic scattering of a photon by an electron. In this interaction a small fraction of the incident x-ray energy is transferred to the electron, and as a result, an electron will be ejected, and the X-ray will be deflected from its original path by an angle θ.

The classical expression to describe this process is obtained by applying the laws of conservation of energy and linear moment. The Compton equation computes the change in wavelength between the incident and scattered X-ray. Therefore, the loss of energy can be estimated by the change in wavelength, as it is showed by **equation 2.3**.

$$\Delta E = E_{X,inc} = \frac{hc}{\lambda_{inc}} - \frac{hc}{\lambda_{scat}} \tag{2.3}$$

Unlike the photoelectric effect, Compton effect probability of occurrence is independent of the atomic number. The probability of this effect is proportional to the tissue electron density, and depends on the energy of the incident X-ray.

Probability occurrence depends on the probability of the photons finding electrons loosely bound in the absorbent material.

Attenuation and Absorption in Compton effect

The attenuation coefficient of the Compton effect (σ) includes the energy loss from photons that result from the Compton effect, and also includes the losses that result from the photons that leaves the x-ray beam. The values of attenuation coefficients are proportional to the density of the material. Hence, the probability of the Compton effect is proportional to the electron density, and since Compton effect was formulated by Klein and Nishina, the cross section is given by the **equation 2.4**.

$$\sigma_a^{KN}(E_0) = Z \times \sigma_e^{KN}(E_0) \tag{2.4}$$

Where $\sigma_e^{KN}(E_0)$ is the total cross section electric of Klein-Nishina.

2.2.3 X-ray linear and Mass attenuation coefficients

The x-ray radiation has the particularity of passing through the material while depositing a portion of its. This results in an attenuation of the beam intensity, and thus in the reduction of the number of photons. The ability of a medium to mitigate is described by the linear attenuation coefficient. Attenuation is the reduction in the density of an x-ray beam resulting from the absorption or the scattering of the x-ray photon after travelling through matter. An X-ray beam passing through a homogeneous object with an attenuation coefficient of μ and a length of δx undergoes a change in its intensity. The intensity variation is given by the Lambert-Beer law whose formulation is demonstrated by the **equation 2.5**, [12].

$$I = I_0 e^{-\mu(E)\Delta x} \tag{2.5}$$

Where I_0 is the intensity of the incident radiation, I is the intensity of the radiation transmitted through the material, Δx is thickness of the material crossed and μ is the linear attenuation coefficient for a material with an atomic number Z. Thus, the attenuation of X-rays through material is determined by an exponential process with respect to the distance travelled.

The attenuation depends on the density of the structures, on the anatomical composition and on the energy spectrum of the X-ray beam. In inhomogeneous objects, the attenuation coefficient will not be constant and it will depend on the energy of the radiation. Thus, for inhomogeneous materials, the intensity of radiation after travelling through a material is shown in the **equation 2.6** . The radiation suffers attenuation with respect to the sum of the contributions along a path $\mathcal{P}$.

$$I = I_0 \cdot \exp\Big(- \int_{\mathcal{P}} \mu(E, x) dx \Big) \tag{2.6}$$

For polychromatic x-ray radiation, the intensity is described in **equation 2.7**.

$$I = \int_0^\infty I_0(E) \cdot \exp\Big(- \int_{\mathcal{P}} \mu(E, x) dx \Big) dE \tag{2.7}$$

The linear attenuation coefficient is expressed in inverse lengths units (cm^{-1}) and is dependent on the density of the absorber ρ. That is why, mass attenuation coefficient is more often used then the linear coefficient, μ_m=μ/ρ, since it is independent from the density. This coefficient is expressed in units of cm^2/g. This can be expressed as a cross section using the relationship expressed in **equation 2.8**.

$$\mu_m\left[\frac{cm^2}{g}\right] = \sigma\left[\frac{cm^2}{atom}\right]\frac{N_A}{M}\left[\frac{\frac{atom}{mol}}{\frac{g}{mol}}\right] \tag{2.8}$$

Where N_A is the Avogadro's number and M is the atomic mass. Since, the intensity of the radiation depends on the type of x-ray interactions with the material, the main interactions of radiation are photoelectric effect and Compton effect. Thus, linear attenuation coefficient can be represented by the sum of the individual contributions from photoelectric and Compton effect, as represented in the **equation 2.9**.

$$\mu = \alpha + \tau \tag{2.9}$$

Where the term α represents Compton contribution, and τ represents the photoelectric contribution. The total mass attenuation coefficient will be, as the linear attenuation coefficient, the sum of the attenuation coefficients for all the different types of photon interactions.

Based on the fact that the mass attenuation coefficient can be described as the combination of the two basic functions, μ_{ph}/ρ and μ_C/ρ, this can be replaced by a_{ph} and a_C, which represent the contributions of the photoelectric effect and Compton effect, respectively.

The attenuation coefficient as a function of energy is represented by a small number of constants that are a set of basic functions. Thus, in absence of K-edge discontinuities, the energy dependence on the linear attenuation coefficient of materials of diagnostic interest can be described by a linear combination of the two interactions described above, photoelectric and Compton effect. In the presence of elements, the description of the attenuation properties of matter will be modified. To describe the attenuation of a material that contains an element with K-edge discontinuity in the energy range applied, the decomposition will be extended by the energy dependent attenuation function of this particular element. Thus, the decomposition of the attenuation reformulated is given in **equation 2.10**.

$$\mu(E,x) = \sum_{p=1}^{n} a_p(x) f_p(E) \tag{2.10}$$

Where the values of p represent the interaction and the component or components whose discontinuity is in the energy range applied, and n the total number of interactions and components that will be included in the decomposition. And $f_p(E)$ in the case of the interaction, as stated is the photoelectric and Compton cross section, while the energy dependent attenuation function of the particular element will include the local density and the mass attenuation coefficient, $a_p(x)$ and $f_p(E)$, respectively.

2.3 Computed Tomography

Conventional tomography had some obstacles that needed to be overcome, such as the overlapping of anatomic information caused by the projection of the three-dimensional anatomic information into two-dimensional information, [12]. The superposition made entire body areas completely inaccessible to radiography, and this led to the development of Computed Tomography. The quantitative CT values of the attenuation coefficient at the level of the pixel in object cuts allows to highlight the differences between anatomic structures using density-based windows and variable width.

Based on the basic concept that it is possible to reconstruct the internal structure of an object from multiple projections, Computed Tomography allows the quantitative mapping of the attenuation coefficients of the object sections.

2.3.1 Components of Computed Tomography

Computerized Tomography components can be divided in three parts: the data acquisition system, the gantry and the operating console. Data acquisition is a method in which the patient is scanned by the x-ray tube and detectors to collect information for image reconstruction. Data acquisition system is formed by three components: x-ray tubes, collimators and x-ray detectors.

Since the goal of this project is extremely correlated with the detector technology used by CPPM, the component that will be presented is the x-ray detector. Furthermore, the technology used at CPPM will be explained in more detail.

X-ray detectors

The role of the detector in the tomography system is to transform the energy of X-rays into an electrical signal, amplifying it and scanning. The electrical signal results from the interaction of the radiation with the substance. Therefore, the x-ray energy can be converted directly or indirectly into an electrical signal, [15] [16]. The X-ray detectors can be classified according to two main approaches. One approach is to classify them according to the x-ray conversion method: direct or indirect,[15] [16]. And the second approach is to classify them by the detection mode: counting and charge integration mode, [16].

Direct detectors converts the X-ray radiation into electrical charges, so the energy deposited by the particle in the detector (semiconductor, gas) is directly converted into electric charges. Direct detection detectors require bump bonding or dedicated deposition techniques. Indirect detectors are so called because they use a material which converts X-rays incident photons into light before they are converted into electrical charges. Therefore, the indirect conversion method requires an intermediate step: the X-ray energy is first converted to photons of visible light by a scintillator, which will create charges in a photodetector.

As stated, the second approach classifies detectors as their detection patterns. The charge integration mode consists in integrating the total charge deposited during the passage of photons during the integration period. One of the disadvantages of integrating detectors is that the amount of electric charges stored in each pixel is limited, [17]. Furthermore, the dark current is integrated and is mixed with the useful signal in the storage area.

Single-photon counting detectors treat each interaction with the sensor: the photons are detected and counted individually. The radiation interacts with the detector and produces a charge which is amplified and compared to a threshold. Only interactions depositing a load greater than the threshold are taken into account. Under these conditions, the measurement of x-ray flux in each detection element is proportional to the number of photons detected rather than the total energy deposited.

Since CPPM uses the photon counting detectors, Hybrid pixel detectors will be explained in more detail.

Hybrid Pixel Detectors

Hybrid Pixel detectors are a type of solid-state detectors whose incident radiation is converted directly into electrons. They are an assembly made by coupling electrically a semiconductor detector with a microelectronic circuit to the signal readout. These detectors consist of two physical parts well separated: the sensor and the electronic circuit reading, as demonstrated in **Figure 2.3**. These two parts are pixelated, [3]. The most common sensor material is silicon, which is economically accessible compared to others. The connection between each pixel and reading cell is made through a jump ball or micro bump lead, called bump-bounding system,[3] [18]. The silicon diode is a semiconductor detector, which provides a high level of electronic integration and a more sophisticated signal processing inside the pixels. The x-ray photons will interact with the sensor and the information will be collected and transferred as deposit charge, to the readout chip. Therefore the photons, through the substrate, are converted into an electrical signal, which is transmitted to the electronic part through the solder ball.

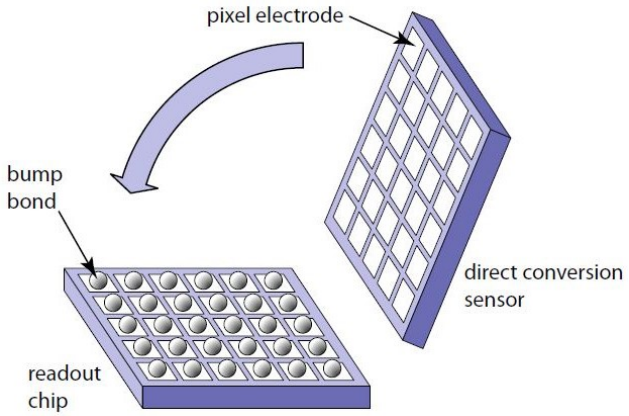

Figure 2.3: Design of a hybrid pixel detector. The pixels of sensor and readout chip are connected in a process known as bump-bonding,[3]

The conversion of photons into an electrical signal takes place at the sensor. The threshold can be regulated by the electronics connecting the hybrid pixel detector to the digital acquisition system.

This technology has the advantage of benefiting from a sophisticated electronic system that integrates a large number of functionalities and a sensor adapted to the energy from the radiation to be detected. The technology of hybrid pixels is the only technology that currently counts the individual photons workforce with the ability to select their energy. The improvement

of spectral separation and the increase of dose efficiency are others advantages of these detectors. One of the main advantages of hybrid pixel detectors is the high geometric efficiency and the fact that an energy threshold can be applied. They are also able of recording photons hits with a specific charge deposition. Since these detectors are counting mode, the influence of the electric noise will affect the measured energy of each photon, but not the photon counts. This technology opens an opportunity to use targeted contrast agent, thus become more quantitative, enabling more personalized diagnostics.

2.3.2 Contrast Agents

The use of contrast agents is one of the methods currently used to increase the contrast. These causes an increase in attenuation in the tissues traversed by X-rays, allowing a better definition of contour of the visualized structures. The contrast obtained after the administration of a contrast agent further depends on the energy of the x-ray beam used. These contrasts allow not only the increase in the contrast between various structures, but also provides dynamic functional and morphological studies of certain structures. An ideal contrast agent needs to have a set of specific physic-chemical properties. Since photon energy corresponds to a particular absorption edge that increases with the atomic number (Z) of the elements, the contrast agent chosen is based on the absorption edge.

2.3.3 Image Artefacts

Image artefacts are any structure or pattern in the image that has no counterpart in the object under study. Any imaging system displays artefacts. The image artefacts can be classified according to the reason that causes the image imperfections. Beam hardening is one of the image artefact examples caused by physical properties of the acquisition system. These artefacts are shown as bands and shadows adjacent to areas of high density. A common artifact is the aliasing distortions that is caused by using an undersampled grid for displaying the reconstructed image.

Image artefacts related with the patient is the movement artefact, which appears on images when objects which are considered to be stationary in the reconstruction present movement. This occurs as a result of either organ movements (heartbeat, breathing and swallowing) or from patient movement during the acquisition. Light larger displacements produce double images.

2.4 Image Reconstruction in Computed Tomography

There are several methods for image reconstruction, analytic and iterative algorithms. The structures that will be reconstructed are considered in this section as a 2D distribution of a function, which represents the linear attenuation coefficient of the structure in analysis. To do reconstruction it is necessary the introduction of projection concept. Projections are the measurement collected along different angles and different distances from the origin point. In order to describe the reconstruction methods, some subjects will be introduce and explained as the Radon transform and sinogram, [13] [19] [20] [21] [4].

A tomographic image is a matrix image where the arrangement of lines and columns, from the individual picture elements, are called pixels. Pixels are the area resulting from the

interaction of the rows and the columns. The volume formed by a pixel and the depth of the cut is known as voxel, where the attenuation coefficient is constant. That is, a voxel is the linear attenuation coefficient volume elements.

Linear attenuation is equal to the composition and density of the tissue inside each voxel in the patient. This way, the reconstructed value in each pixel is the linear attenuation coefficient for the corresponding voxel.

The matrix reconstructed filled with linear attenuation coefficients is transformed into a corresponding matrix of Hounsfield units. Hounsfield scale allows the quantification of the attenuation coefficients of the different materials covered by the X-ray beam in Hounsfield units (HU). The Hounsfield unit can be also called by TC number, which is calculated by the **equation 2.11**.

$$TC = \frac{\mu - \mu_{H_2O}}{\mu_{H_2O}} \times 1000 \tag{2.11}$$

Where the μ is the attenuation coefficient of the tissue in study, and μ_{H_2O} is the water attenuation coefficient. The attenuation coefficients after being converted into HU scale, are converted into a scale of grey.

2.4.1 Sinogram and Radon Transform

The object can be modelled by a function f in the *(x,y)* plane of the section. The parameters that will be introduced are the angle θ and u which is the distance to the center of rotation. The data acquired from the computerized tomography systems can be displayed before proceeding to the reconstruction methods. Sinogram is the name given to the images displayed before following the reconstruction. The horizontal axis of this type of image corresponds to different rays in the respective projection. The sinogram results from the alignment of all parallel projections along a matrix. Each row corresponds to one-dimensional projection obtained from a certain angle, and each column shows the distance measured from the center of the image. It is called sinogram because the structure appears as a sine function. The measured projection at every angle θ is denoted by $p(u, \theta)$.

Image reconstruction is the procedure of estimating an object, described by a function, from a set of projections. The x-ray radiation makes an angle of θ with the x-axis. Two new coordinate are defined *(u,v)* which result from rotating the system *(x,y)* over the angle θ. The Cartesian coordinates *(x,y)* are transformed according to the transformation **equation 2.12**. Thus, the set of expressions that define the line showed in **Figure 2.4** are described in the **equation 2.12**. The expression of the line can be written in the form of parametric line, where the parameter u and v is used.

$$\begin{pmatrix} x \\ y \end{pmatrix} = \begin{pmatrix} cos\,\theta & -sen\,\theta \\ sen\,\theta & cos\,\theta \end{pmatrix} \begin{pmatrix} u \\ v \end{pmatrix} \tag{2.12}$$

For an angle θ the intensity as a function of u, after applying the coordinate transformation given in **equation 2.12**, the intensisty formulation is given in **equation 2.13**.

$$I_\theta(u) = I_0\, exp\Big(- \int f\Big(u\, cos\theta - v\, sen\theta, u\, sen\theta + v\, cos\theta\Big)\, dv\Big) \tag{2.13}$$

For each measurement of intensity, the attenuation line is computed by the **equation 2.13**. Thus, the intensity profile is then transformed into an attenuation profile which is the projection of the function *f(x,y)* along the angle θ. Representing all the projections $p_\mu(u)$ in a 2D data set $p(u, \theta)$ is called a sinogram represented in **Figure 2.4**. The transformation of the function *f(x,y)* into the sinogram $p(u, \theta)$ is called the Radon transform, which is a projective transformation of a two-dimensional function onto the polar co-ordinate space. Radon transform of a function converts a spatial coordinate system to Radon space coordinates (u, θ). **Figure 2.4** shows the line integral of *f(x,y)* in the vertical direction which is the projection of *f(x,y)* onto the x-axis, [20].

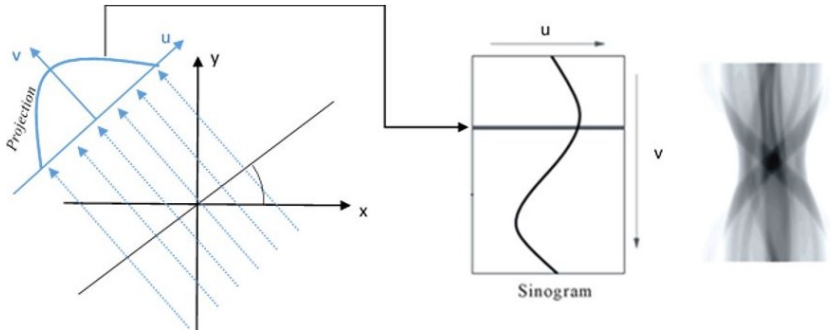

Figure 2.4: Relation between the Cartesian Coordinates and the acquisition of each projection, [4], [5]

Radon transform for a given θ is given by **equation 2.14** .

$$\mathcal{R}[f](u, \theta) = p_\theta(u) = \int f\Big(u\, cos\theta - v\, sen\theta, u\, sen\theta + v\, cos\theta\Big)\, dv) \tag{2.14}$$

2.4.2 Analytic Methods

Analytic methods are the most used in commercial computed tomography scanners. The backprojection method consists in obtaining images in different projections. Therefore, it is a mathematical process which is designed to match the acquisition process in reverse. This way, the objective of this method is to reconstruct an image from the data that has been calculated from the projections.

The simplest situation to perform backprojection method is when parallel beams are used for measuring the projections. In consequence, the angles θ use to describe the lines in the sinogram space are between $[0, \pi]$. Backprojection operation will be named by $\mathcal{B}$, which consists, of a point *(x,y)*, in the sum of the projections $p_\theta(u)$. **Equation 2.15** represents the backprojection operator.

$$\mathcal{B}[p](x, y) = \int_0^\pi p_\theta(u) d\theta \tag{2.15}$$

The final image acquired is the sum of all the backprojected views, which it a very "blurry" image. In order to solve the blurring problem encountered in backprojection, a new technique has been developed to which was given the name of Filtered Backprojection,

Central Slice Theorem

The Fourier slice theorem is an important concept in order to understand the filtered Backprojection. Taking the same concepts as Radon transform, *f(x,y)* is the object function that will be reconstructed and $p(u, \theta)$ is the projection. This method states that "the Fourier transform of parallel projection of an object function *f(x,y)* taken at angle θ gives a slice of the two dimensional transform of *f(x,y)* , $\mathcal{F}(u, v)$, subtending an angle θ with the u axis" [23].

Radon transform is an operator that operates in the space coordinates, in order to do image reconstruction it is also needed to perform in the frequency domain. The operator used is the Fourier transform. Indeed, it establishes a link between the 1D Fourier transform of the projections and transformation 2D of the image *f(x,y)*.

Thus, the Fourier slice theorem has three main steps, which are the calculation of the Fourier transform of the projection, sequentially the construction of the Fourier transform of *f(x,y)* from the Fourier transform of the projection, and finally the calculation of the inverse Fourier transform which provides the desired function *f(x,y)*.

The 1D Fourier transform can be written using the definition of the projection, which is given in **equation 2.16**.

$$P_\theta(v_u) = \int_{-\infty}^{\infty} \int_{-\infty}^{\infty} f(ucos_\theta \, - \, vsen_\theta, \, usen_\theta \, + \, vcos_\theta) \, e^{-i2\pi u v_u} \, du \, dv \tag{2.16}$$

When rewriting the **equation 2.16** into Cartesian coordinates, the resulting equation is equal to the 2D Fourier transform. This way, the central slice theorem can be summarize by the **equation 2.17**.

$$\mathcal{F}_1[p_\theta](v_u) = \mathcal{F}_2[f](v_u \, cos\theta, v_u \, sen\theta) \tag{2.17}$$

Filtered Backprojection

With filtered Backprojection, the data acquired is mathematically filtered before being backprojected onto the image matrix. The new filtered projection is obtained by applying the inversion of the Fourier transform. The superposition of all the Backprojection information will provide an approximate picture of the attenuation coefficients of the several tissues. The filtered backprojection has three main steps: the calculation of the Fourier transform of the projection; back transform of the high-pass filtered of the projection resulted from the first step; and apply the backprojection.

Thus, as a first step to acquire the original image *f(x,y)* from the projection, the inverse Fourier transform is applied. After the conversion into polar coordinates, the central slice theorem showed in **equation 2.17** is applied. Consequently, the image represented by the function *f(x,y)* is obtained by backprojection using filtered projections, in which the filter used

is a ramp filter ($H(v_r) = |v_r|$). In order to keep the generality about the filter, this was replace by a general filter H. Expression $h = F_1^{-1}[H]$ is used, which in the frequency space is expressed by a convolution in the spatial domain. Thus, the final solution resulting from the use of h is expressed in **equation 2.18**, which is the final solution of filtered backprojection for the parallel beams.

$$f(x,y) = \int_0^{\pi} (p_\theta * h)(u)\, d\theta \tag{2.18}$$

2.4.3 Iterative Methods

The objective of the iterative methods is to find a solution by successive estimations. This methods are based on attempts to maximize or minimize a target function determined by several analytical iterations. The projection data is predicted based on assumptions about the attenuation coefficients of all voxels. Iterative image reconstruction consists of three components that describes the information, a function that quantifies the correlation between the estimated image and the information obtained, and finally the third component which is an optimization algorithm that determines the next estimate image based on the primary estimate, [22]. The iterative methods are divided into two types of methods, the algebraic methods and the statistical methods.

The algebraic reconstruction techniques divide the space in order to be rebuilt in a finite number of cells, which are not overlapping. The estimation of the attenuation coefficients of each cell can be made by linear equations, provided that the radiation beam attenuation measurements are obtained at different positions. The set of M linear equations represent the projections, with unknown constants N, which are the linear attenuation coefficients. By solving the set of N linear equations and estimating the values of the N unknown linear attenuation coefficients, it is the tomographic image is reconstructed.

Statistical iterative algorithms can work in three different domains: in the domain of the raw data projections, in the domain of the volumetric images or during the iterative reconstruction process. One of the algorithms used is the Maximum-Likelihood Expectation Maximisation algorithm (ML-EM), which allows the calculation of unknown data. In each iteration, it will be characterized by two stages, expectation and maximization. In the expectation stage, the algorithm seeks to estimate unknown image, and in the maximization the algorithm seeks to maximize the likehood function, derived from the Poisson statistics.

2.5 Spectral Computed Tomography

One of the next goals of the Computed Tomography research field is the development of energy sensitive CT scanner. Spectral CT takes in consideration that the transmitted radiation carries more information than intensity changes, that x-ray tube produces a wide range of energy spectrum and that the attenuation of radiation depends not only on the material but also on the photon energy. This technique obtains data for multiple energy intervals during a single scan by using an energy-discriminating detector. Spectral CT differs from the other techniques

in the sense that it uses the attenuation characteristics at more than two energies, and within narrow energy ranges.

Photon counting detectors are used in this technique since the incident spectrum is separated into multiple binned spectra whose shape depends on the energy threshold setting of the pulse height analyser. Hybrid pixel detectors are a type of photon counting detector that allows the energy threshold setting. The choice of the energy thresholds is done according to the knowledge of the physical characteristics of the tissues being analysed. As mentioned in the photoelectric effect section, the attenuation coefficients are the basis for the separation of the elements in CT. Spectral CT combined the particularity of the hybrid pixel detectors and the discontinuity of the photoelectric effect in order to separate different materials. This discontinuity is related to the K-shell energy which will be explored by K-edge imaging technique which is one of the spectral CT approaches.

As it was explained, different materials have different response depending on the energy of the incident radiation. Thus, different materials will have different responses according to the X-ray energy spectrum. Physical basis functions as the photoelectric effect and Compton effect can be represented as a linear combination, furthermore, any material can be also represented as a linear combination of different materials.

Spectral CT permits the differentiation between different tissues types such as bone, muscle, fat and a contrast agent. This technique also allows studying the contributions of the Compton and photoelectric effects [23] [24]. In multi-energy CT, the user is able to choose the range of energies in order to identify the materials. The x-ray attenuation depends primarily on this two interaction with matter mentioned before, which can be expressed in a linear combination. In order to identify a certain material, the attenuation coefficient of the material can be modelled as a linear combination. Several studies showed what kind of materials should be used in order to be able to detect them in CT.

The key technology used for spectral CT is the energy-resolving photon-counting detector. Thus, the main difference between the dual energy CT and spectral CT is the detectors used, which in spectral CT are the hybrid pixel detectors. This technique allows material identification and quantification. As it was mentioned before, hybrid pixel detectors are designated to discern the photon energy so that spectral information can be obtained from a polycentric x-ray radiation. Ideal hybrid pixel detectors give more energy information, since this is recorded as the number of counts within different energy windows or bins. This way, at least two energy bins are necessary, when it exists two energy bins dual energy information is provided. In order to have spectral information, the number of bins is increase, which also provides a better material decomposition estimation. Thus, spectral CT measures the attenuation at two or more energies which allow the discrimination of different tissues based on the energy behaviour.

Multiple energy bins allow the use of multiple basis functions, which will require the use of contrast agents as Iodine. This way, to verify the presence of Iodine in a structure, and for this contrast agent be recognize in the reconstructed image, the energy bins used should be above and below its K-edge. The idea of using the K-edge concept brings to the principle of K-edge imaging.

In conclusion, spectral CT is a new technology which arises from the same concepts as dual energy CT. Spectral CT is a more sophisticated technique because of the use of photon counting detectors, the hybrid pixel detectors, which have the ability of counting single photons and discriminate the photons into pre-defined energy windows based their energy. The photons

have spectral information which provide more information on the composition of the structures in analysis. The main advantages of using Spectral CT in detriment of other techniques is that each energy is acquired simultaneously so there are no recording problems between different energies; this technique was able to solve the overlapping of energies which posed a problem with Computed tomography and dual-energy CT that will be mentioned in the next section.

2.5.1 Dual energy CT: the origin of Spectral CT

As it was shown in the previous sections, each material has a characteristic X-ray attenuation which depends on the atomic number, density and incident energy of the x-ray radiation. Computerized tomography describes the structures with only one value such that different materials might show very similar attenuation. Using $p_\theta(u)$, from **equation 2.14** where the projection for a polychromatic radiation is described, when the log is taken out of the equation, it will be non-linearities of the line integral, which will be reflected in the reconstructed image as beam hardening. This artefact limits the accuracy of attenuation measurement in CT imaging.

Computerized tomography is limited by the fact that CT numbers don't vary very much with beam energy for soft tissues. Consequently, it is possible to differentiate the different materials by applying different x-ray spectra. In order to do a precise differentiation between different tissues one needs to apply different ranges of energy, hence the development of the dual energy CT technique, [25] [26]. This technique studies the different ways x-ray photons interact with matter and how to extract information which can help to further locate the characteristics of the scanned object, [26].

Dual-energy techniques discriminate the energy at the source level. As said, two acquisitions are performed successively with two different energies. As stated, this technique is good when the structure in analysis is static but in realistic cases, it will create spatial mismatch. The technology that discriminates the energy at detector level uses scintillator detectors, which were shown not to be efficient since the energy separation is poor, [27].

Dual-energy CT is also known by the abbreviation of DECT, whose concept was developed at in the very beginning of computed tomography history, [25]. The main principle of dual-energy CT is based on the principle that high and low photon energies will cause diverse behaviours in the tissues which will make possible to differentiate the materials. In CT the two effects considered are photoelectric and Compton effect and the probability of these effects depends on the energy, this way at least two measurements at different energy levels are needed. DECT is used to differentiate the tissues by exposing them to two different X-ray spectra, or using a detector with different energy ranges. Therefore, the system has two X-ray sources which allows to measure simultaneously the x-ray attenuation at low and high energy levels such that two attenuation values are present in each voxel. The technique is based on the difference between materials absorption at different x-ray photon energy.

This way, dual energy CT uses two pairs of x-ray tubes and detectors, which rotate around the target. The choice of energies is related to the attenuation values of the materials under analyses. Attenuation values at a certain energy will be used to differentiate the material from the surrounding materials. One of the discoveries made in the field was that materials with larger difference in the atomic numbers are easily differentiated. The dual energy techniques provide atomic number measurements of a material in addition to density measurements.

As it was mentioned before, the mass attenuation coefficient of a material can be con-

sidered as the composition of two contributions, the photoelectric and Compton effect. To determinate the individual contributions of the effects, two different photon energies are needed, a low and high photon energy, [26]. Thus, taking the **equation 2.10** the low and high energy are represented in **equation 2.19** and **equation 2.20**.

$$\left(\frac{\mu}{\rho}\right) = (E_L) = a_{ph} f_{ph}(E_L) + a_C f_C(E_L) \tag{2.19}$$

$$\left(\frac{\mu}{\rho}\right) = (E_H) = a_{ph} f_{ph}(E_H) + a_C f_C(E_H) \tag{2.20}$$

Figure 2.5 shows the overlap between the two generated spectra, one at low energy and the other at high energy, 80 kV and 140 kV respectively. And only two different energy data sets are practically feasible, which will limit the number of identifiable materials.

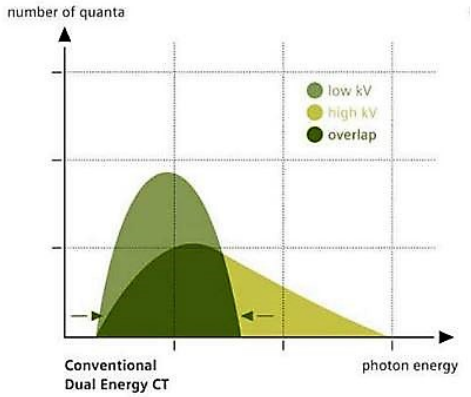

Figure 2.5: Energies used in Dual CT, with the corresponding overlap between the two energy ranges used, [6]

The overlap makes material characterization more difficult, since the high energy spectrum contains low energy photons which will add more noise. Thus, a solution to overcome this issue is to decrease the overlapping between the different energy spectra. This way, photon counting detectors were created in order to discriminate energy.

Dual-energy CT led to the development of the Spectral CT technique, which was normally used to suppress beam hardening or to discriminate to some extent between elements whose atomic number is below 20. By acquiring images at more than two different energy levels, the technique will not only be able to differentiate the elements but will also discriminate the element contributions from the interaction contributions. Thus, the technique that combines the use of more than two energy ranges and the photon counting technology is called Spectral CT.

2.5.2 K-edge Imaging: general idea

K-edge Imaging is one of the approaches used in spectral CT systems, where more than three measurements for each voxel are acquired. This approach explore the discontinuity in the photoelectric effect. As explained, the discontinuity is generated when photons interact with matter, and those interact with the shell electrons. Photons will be attenuated when electrons

are freed in the lowest energy shell of the absorber. The lowest energy shell is called K-shell. The photoelectric effect only occurs when the emitted energy is identical or bigger than the energy of the K-shell electron, as explained in detail in 2.2.

Contrast agents have a crucial role in K-edge imaging, since the K-edge energies of these materials are in the diagnostic energy range. Thus, K-edge imaging makes possible the transformation of CT into a true molecular imaging technology. As it was shown in Dual energy CT, the attenuation of the x-ray with matter can be described as a linear combination of basis functions, which represent physical effects. K-edge imaging beyond using the physical effects also use as basis functions the absorbing materials information. Thus, the attenuation of photon caused by different absorber materials is a linear combination of their respective basis functions. The presence of contrast agents introduces a discontinuity, the so-called K-edge. This way, depending on the number of contrast agents that are analysed, the attenuation will be described at least by three basis functions.

Figure 2.6 shows the principle of K-edge imaging, where Iodine is considered as the contrast agent whose K-edge is equal to E_K. As only one energy threshold can be set per pixel, two separate acquisitions with two different thresholds are required, E_K^+ and E_K.

The measurements made at each pixel present in the hybrid pixel detector follows the three equations below, **equation 2.21**, **equation 2.22** and **equation 2.23**.

$$N(E_K^+) = \int_{E_K+\Delta E}^{\infty} N_0(E)\, exp\Big(- \int_{\mathcal{P}} \mu(E,x)dx \Big)\, dE \tag{2.21}$$

$$N(E_K) = \int_{E_K}^{\infty} N_0(E)\, exp\Big(- \int_{\mathcal{P}} \mu(E,x)dx \Big)\, dE \tag{2.22}$$

$$N(E_K^-) = \int_{E_K-\Delta E}^{\infty} N_0(E)\, exp\Big(- \int_{\mathcal{P}} \mu(E,x)dx \Big)\, dE \tag{2.23}$$

Thus, K-edge technique is applied by performing the subtraction of **equation 2.21**, **equation 2.22** and **equation 2.23**. K-edge imaging relays on the influence of the atomic number on contrast sensitivity. Since the attenuation of materials decrease when increasing X-ray energy, the subtraction effectively removes materials while enhancing the attenuation jump due to the K-edge. This way the number of detected X-rays inside the energy window chosen is obtained by subtracting the acquisition with the higher threshold from the acquisition with the lower threshold. The resulting equation which variables are represented in **Figure 2.6**, are given in **equation 2.24** and **equation 2.25** .

$$N^+ = N(E_K) - N(E_K^+) = \int_{E_K}^{E_K+\Delta E} N_0(E)\, exp\Big(- \int_{\mathcal{P}} \mu(E,x)dx \Big)\, dE \tag{2.24}$$

$$N^- = N(E_K^-) - N(E_K) = \int_{E_K-\Delta E}^{E_K} N_0(E)\, exp\Big(- \int_{\mathcal{P}} \mu(E,x)dx \Big)\, dE \tag{2.25}$$

This way, the **equation 2.24** and **equation 2.25** represent how the attenuation coefficient is different for materials with K-edge. The example given to apply K-edge uses Iodine and water, where Iodine is the contrast agent and water is used in order to represent soft tissues. Iodine has its K-edge at 25.5 keV which is represented in **Figure 2.6** by the variable E_K. The spectrum was divided into two windows of energy by the energies described: E_K^+,E_K^-, E_K.

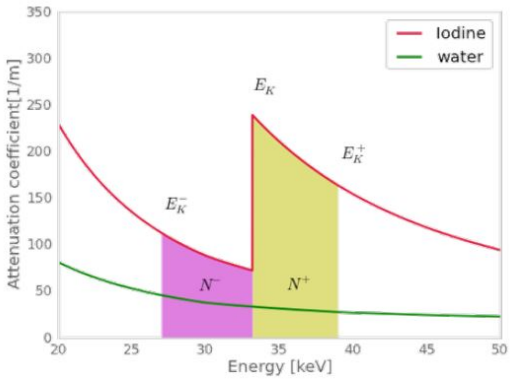

Figure 2.6: Illustration of the E_K around the K-edge of the material under study, [7]

Thus, it was identified the K-edge energy of the contrast pharmaceutical, and then that component was subtracted in order to achieve an equivalent contrast-free image and an image where only the contrast agent is visible, without performing another scan.

Therefore, due to the discontinuity in the attenuation, Iodine represents the third basis function. As it was explained in 2.2, besides the physical interactions, materials can also be represented by a linear combination of physical basis functions. Given the example in **Figure 2.6**, the third basis material is required in order to represent objects containing the K-edge material. Taking **equation 2.10**, using contrast agents which has K-edge in clinical range, the equation that translated the attenuation is given by **equation 2.26**.

$$\mu(E,x) = a_{ph}(x)\, f_{ph}(E) \;+\; a_C(x)\, f_C(E) \;+\; \sum_i a_{K_i}(x)\, f_{K_i}(E) \tag{2.26}$$

The third element of **equation 2.26**, can be added as many terms in K-edge, since it depends on the number of contrast agents used.

Chapter 3

Background of the study

The second chapter explained how the passage of x-ray radiation through an absorber gives information about the element composition, and the evolution and the improvement of computerized tomography.

Recent studies have considered that the use of analytical formulations and numerical simulations in order to calculate the photoelectric and Compton coefficients are important to distinguish different tissues. This way, the acquisition of spectral information is obtained concerning the spectrum used and the type of detector to detect the radiation. Several clinical applications have been established for dual-energy CT based on the differentiation or quantification of materials. Material differentiation is used to separate low and high Z-number materials, which in this case is done by using the photoelectric and Compton basis function shown in Chapter 2. Material quantification allows the reconstruction of non-enhanced images.

Spectral CT has been discussed since at least 1976, and in the meantime the technique has been improved and developed by several research groups. The leading manufacturers are developing their own Spectral CT systems. Therefore, Chapter 3 will contain a description of the studies made in Spectral CT until now. Accordingly, a summary of the different approaches to obtain spectral data will be produced. This project was elaborated in the Centre de Physique des Particules de Marseille. Thus, the research in this chapter was done in the context where the CPPM is inserted comparing with different approaches mentioned. For about ten years, the imaging team had been developing a photon counting detector, which today is in its third generation. Around the detector, the team also has developed a flexible system of micro-CT, the PIXSCAN. This system has demonstrated its ability to compete with the standards in the field of computerized tomography.

In this chapter, the different studies made at the CPPM that contributed to the thesis project will be detailed. The concept of Spectral CT and K-edge energy will be referred in order to sow which advances were made.

One topic referred previously was that Spectral CT couldn't overcome entirely the images artifacts related with motion artifacts. One solution proposed by [7] is the use of composite pixels, which are a setup of pixels with different energies. In this chapter, the experiments made with composite pixels will be shown with the purpose of confirming this as good solution and as an introduction of the main topic of this research project.

3.1 Spectral CT system approaches

As said previously, the firsts approaches to differentiate materials using the attenuation characteristics of different materials and the energy dependence started in 1970s. These are multi-energy techniques which are based on the energetic dependence of X-ray material absorption that provides material information. Several groups contributed to the development of Spectral CT, which was made in detector and source technologies, image reconstruction, material decomposition and performance evaluation.

In the study [28], in order to acquire energy information, they took into account that the energy response of the detector had to be calibrated. The existing techniques for energy calibration were not convenient, thus the research group developed an automated technique. This technique calibrates the energy response of the pixels in a detector that runs with minimal user intervention. The detector used for this study was Medipix3RX.

Li et al. [29] developed a scheme of hybrid detectors and a tensor-based algorithm to reconstruct spectral CT images. The architecture of the hybrid detectors combine the dynamic-threshold-based counting and integrating mode. The advantage of this detector is that the energy threshold can be changed during a spectral CT scan.

Oyang et al. [30] analysed spectral CT system design which uses a conventional x-ray source with multiple balanced k-edge filters. Spectral CT uses a new technology of detectors, which is the most recent technology used in multi-energy CT systems: photon-counting detectors. Photon-counting detectors allow the acquisition of several energy levels per image. As previously said, photon-counting detectors measure the amount of energy deposited by the photons and increments a counter associated to the energy. Thus, for each energy range, called bins or thresholds, the detectors will detect the individual x-ray photons correspondent. Photon-counting detectors currently in use have up to eight energy thresholds. The photon counting detector that will be specified in this thesis will be the XPAD3. This was developed by CPPM and it comes from the work of the CERN DELPHI and ATLAS. XPAD3 will be explained in more detailed in the Chapter 3.

In 3.1.1 and 3.2 of this Chapter, the two main different approaches of the Spectral CT approaches will be shown being that the CPPM approach will be shown in detail, since this is the one upon which this argument is based.

3.1.1 Philips Research: Spectral CT acquisition approach

In the research project described in [23], an experimental proof of an extension of the dual-energy method to a higher number of basis components was made. In [24] a study was made with the main purpose of investigating which energy-sensitive photon counting devices were able of revealing quantitative information about the composition of an absorber. The group involved measured and achieved images showing the local density of a contrast agent in the framework of dual-energy pre-processing. Thus, the study that will be presented in this section is a confirmation of the simulations presented in [24]. This was based on the Spectral CT technique using more than one contrast agent, and a set of energies. The photon counting detector used was a single-line photon-counting CdTe array manufactured by GammaMedicaIdeas (Northridge, Ca., USA).

Thus, the spectral CT scanner was based on a rotating gantry that allows convenient multi-slice scanning. The two contrast agents used were iodine and gadolinium based, [23]. The layout of the phantom used is presented in [23]. Therefore, the PMMA phantom hosted contrast agents filled tubes surrounded by calcium-hydroxyapatite in a gel matrix. Each tube was filled with three different concentrations of each contrast agent.

The energy dependence of the linear attenuation of materials can be approximated by a linear combination of the photoelectric effect, Compton effect and by the energy-dependent attenuation functions of the two elements. Taking **equation 2.26** linear attenuation coefficient can be rewritten, where $a_{Ki}(x)$ is equal to $a_{Gd}(x)$ and $a_I(x)$; and f_{Ki} is equal to $f_{Gd}(E)$ and $f_I(E)$, which are the local density and the mass attenuation coefficient of gadolinium and iodine, respectively. In this case, where two contrast agents are used, it is necessary to perform four measurements. The photon counting detector used applied energy discrimination by six threshold values for each individual pixel.

Equation 2.7 shows the acquisition model for polychromatic radiation, the photon counting detector used in this study applies this acquisition equation, **equation 3.1**.

$$I = \int_0^\infty I_0(E) \cdot \exp\Big(- \int_{\mathcal{P}} \mu(E,x)dx \Big) dE \tag{3.1}$$

The study [23] presents the results of the spectral decomposition. Four basis function were used to describe four attenuation processes: photoelectric absorption, Compton scattering, attenuation by iodine and attenuation by gadolinium. In conclusion, the study proved that more than two heavy metals can be distinguished and quantified independently from a single scan.

3.2 CPPM approach

At CPPM, a micro-computed tomography (micro-CT) prototype PIXSCAN equipped with a hybrid pixel camera based on the XPAD3 chip bump-bonded to silicon sensors was developed. The description of the components and operation of the micro-CT and the XPAD3 detector will be made in the Materials in Chapter 4. XPAD3 are hybrid pixel detectors, whose pixels perform digital conversion of photons signal through certain thresholds. XPAD3 has the particularity of fine-tuning the threshold of each pixel independently. Thus, these detectors have a single threshold per pixel that can be set to a few keV to about 35 keV, [31].

The capability of hybrid pixels detectors to select photon energy is exploited in clinical imaging, specially using the K-edge effect. As mentioned in Chapter 2, for values close to the K-shell binding energy of a certain element, the attenuation coefficient acts differently in comparison with the surrounding materials.Since the prototype used at CPPM, XPAD3, allows the choice of an energy threshold, K-edge imaging was performed in order to compare images taken at different energy thresholds. Thus, the results are obtained by subtracting two acquisitions taken with the pixel thresholds set at two different energy ranges. In the next section, the studies made to test the K-edge imaging procedure will be detailed.

CPPM uses the technique described above applying the equations defined in Chapter 2, **equation 2.21**, **equation 2.22** and **equation 2.23**. The images that result from this procedure

are called K-edge images, where one is able to identify the contrast agent content that appears with positive or negative values depending on the subtraction made.

Studies made by CPPM represents an undeniable proof of this method. However it will be shown that the images reconstructed using a specific energy window are pretty noisy because of the large variance in the window images that results from the sum of the variance of the single acquisitions. Since at least two acquisition are made, movement artifacts are a problem related to this technique.

Several solutions are exposed in [31] to try to solve the problems presented above. With regard to noise, the solution found was to increase the detection efficiency by using CdTe sensors instead of silicon sensors. Concerning the movement artifacts observed in the images, [7] explored the chance of performing only one acquisition with pixels set at different thresholds along a certain pattern to form composite pixels.

These are the results acquired using the principle of the K-edge imaging method, where it was took in consideration the photoelectric and Compton effect, and the contrast agents. CPPM did several studies regarding the composite pixels, which will be explained and demonstrated in the following section.

3.2.1 K-edge Imaging

In medical imaging, contrast pharmaceuticals that contain highly attenuating heavy metal elements are used, to see the anatomy in order to do the diagnosis of many conditions. This is due the K-edge being a feature of the X-ray attenuation spectra of the elements.

Thus, K-edge imaging is acquired by changing the pixel threshold around the K-shell binding energy of the materials under study. The imXgam group published papers [7] [32] [33], which explain and demonstrate the use of K-edge to study the materials and effects. This will be discussed in the **section 3.2.1**, the separation of photoelectric and Compton effects, using the K-edge concept.

Photoelectric and Compton effect

The Photoelectric effect occurs when specific energy radiation is incident on a surface and causes the ejection of electrons. Because of the K-shell concepts, each component has a specific energy where the photoelectric effect happen. The Compton effect is known as the scattering Compton effect, since a part of the photon energy is transferred to the electron, and the rest is scattered. This way, the photoelectric effect will depend on the atomic number of the materials, and it will be responsible for most of the contrast in Micro-CT images.

The Compton effect is one of the responsible effects for the noise present in the images. Thus, by separating the two effects will reduce the beam hardening artifacts that degrade the image quality. In the paper [32], it is described the separation of the Photoelectric effect and the contrast agents.

The polychromatic acquisition model in paper [32] add the parameter noise. The noise was modelled as Poisson noise, and it can be approximated to the Gaussian noise. In the experiment, a cylindrical phantom of water with two aluminium balls was used in order to

generate beam hardening. The separation of the photoelectric effect and the Compton effect was possible, since they are energy independent. The results achieved by this study [32] used the ML-EM reconstruction, where a filtration was performed using three different types of elements: Aluminium, Niobium and Copper. Comparing the those images, the authors observed that the beam hardening is seen between the two Aluminium balls, which is possible to verify in the two first images by the presence of bright lines that connect the two balls. In the third image, the beam hardening is cancelled.

Contrast Agents

As said previously, the contrast agents are used to differentiate components. In paper [32], the authors studied the separation of the two different contrasts agents, Iodine and Silver, whose the K-edge values are 33.2 keV and 25.5 keV, respectively. The experimental setup was two phantoms, one with a cylindrical form with eight inserts, and the second phantom, had three twisted rubber pipes. The inserts and the pipes were filled with certain materials. Three CT scans for each phantom, with three energy thresholds were performed. The three thresholds produced two ranges of energies, which were set by the **equation 3.2**, **equation 3.3** and **equation 3.4**.

$$E_1 = (E_K - \Delta E_1) \tag{3.2}$$

$$E_2 = E_K \tag{3.3}$$

$$E_3 = (E_K - \Delta E_K) \tag{3.4}$$

The comparison of the differences $(E_1 - E_2)$ and $(E_2 - E_3)$ allows the visualization of the selected contrast agent. In the study [32], the authors divided in three images the data acquired by each energy presented in the equation above. Therefore, it was verified that after performing the differences $(E_{2Ag} - E_{3Ag}) - (E_{1Ag} - E_{2Ag})$, the structures that contain silver solution appears as positive CT numbers. The same was done for Iodine, which the parameter that changes is E_K

3.2.2 Composite Pixels

Spectral CT has been used because of the advantage of choosing the range of energy. The analysis of the structures in this technique requires several acquisitions. Between the acquisitions it was noticed the presence of edges effects. **Figure 3.1** represent the two images resulting from two acquisitions. Comparing the two images of **Figure 3.1** , the author concludes that the mouse movement between two consecutive scans results in edge effects. Additionally, in **Figure 3.1b** it is observed that the ureters are better defined. While, in **Figure 3.1a** it is visible to presence of negative values around the kidney due to the mouse movement.

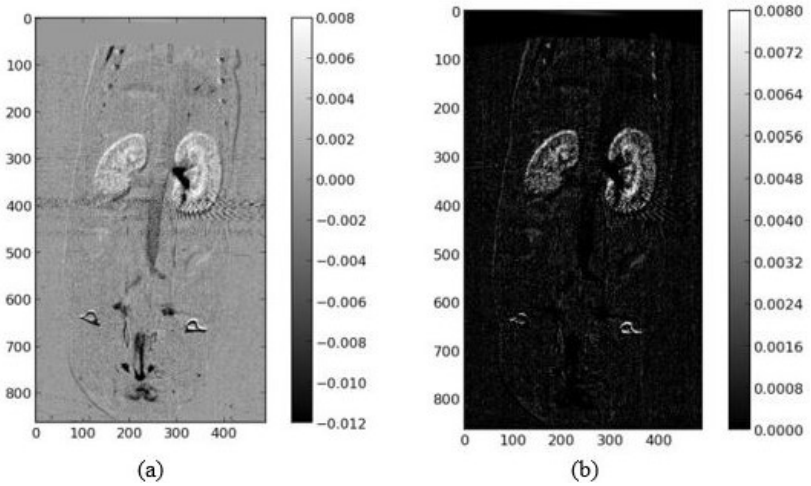

Figure 3.1: Coronal slices of an Iodine K-edge image, (a) positive and negative values, and (b) only positive values. [7]

Artifacts degrade the quality of computed tomography images and can be caused, for example, by the movement of the structures. One of the solutions for those common artifacts is the use of composite pixels. The composite pixels are an ensemble of pixels that are set in different thresholds. Thus, instead of computing several acquisitions with one threshold per acquisition, only one acquisition was computed, in which the pixels are set for more than one threshold. The **equation 2.24** and **equation 2.25** shows the CPPM approach.

In the experiment performed by the imXgam group at CPPM, the principle of K-edge imaging and the composite pixels was used [7]. Iodine and silver were used as contrast agent due to their high K-edge energy. Three attenuation coefficients are presented in **Figure 3.2** water, silver and iodine. The K-edge energy is specific to a chemical element, which is visualized in the images of **Figure 3.2** by the abrupt increase of the photoelectric cross-section. The images show that Iodine and Silver show the increase of the photoelectric cross-section at different energies, 33.2 keV and 25.5 keV, respectively. Whereas **Figure 3.2b** shows that contrast between water and Iodine is better in the green energy range. The first range of energies has values between 25.4 keV and 33.2 keV, and the second range, represented in green, varies between 33.2 keV and 40.2 keV.

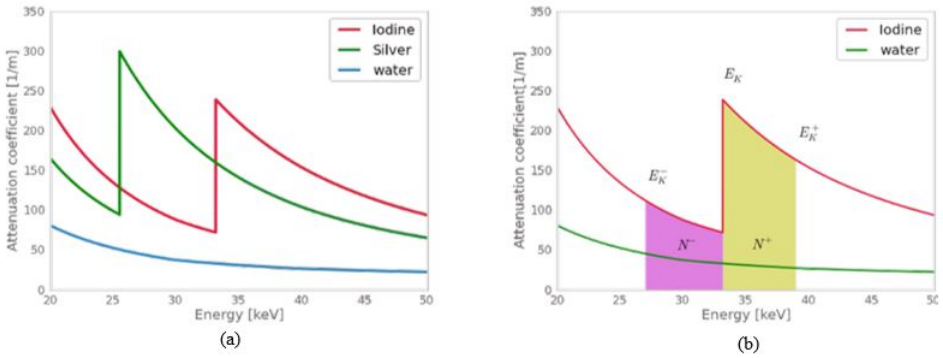

Figure 3.2: Graphic representation of the linear attenuation coefficients as a function of energy of (a) Iodine, Silver and water, and (b) Iodine and water.[7]

The imXgam group had to do two separate acquisitions with three thresholds (E_K^+, E_K^-, E_K) , in which the two energy windows were bound by the three threshold values. Then, in order to get the K-edge images of the contrast agents, Iodine and Silver, the difference between the reconstructed images was computed. This difference is expressed in the **equation 3.5**.

$$N^+ \; - \; N^- = \int_{E_K^-}^{E_K^+} N_0 \, exp\Big(- \int_\Gamma \mu(E,x)dx \Big) dE \tag{3.5}$$

K-edge imaging done in the experiment [7] consists of an acquisition in which the pixels had three thresholds. The author of the paper tried three different patterns of composite pixel threshold setting: in columns, in rows and in tartan.

The pixels were set in a series of three by three. The features of XPAD3 will be explained in detail in next chapter. This way, it was defined that 390 μm composite pixel counts as the average of the counts of the three pixels of the composite pixel that is set at each energy. It is illustrate in **Figure 3.2a** the set of composite pixels with 9 pixels. The goal of the author was studying the best pattern of composite pixels, and which results were better between one acquisition and all the acquisitions.

The experiment was divided in two parts, [7]. In the first part Iomeron was injected intravenously in a mouse, and in the second part a phantom which was filled with Iodine, silver nitrate and water was used. Several acquisitions were made, in order to evaluate the composite pixels. The acquisitions were of two types; one where the pixels were set in one of the patterns and all the pixels had an energy threshold and the second type consisted of three acquisitions where each one of them had one threshold using one of the referred patterns. Then, the difference between the three acquisitions was computed, in order to compare it with the single acquisition using patterns. Therefore, in [7] the images that were presented are the ones acquired after the mouse had been injected intravenously with Iomeron; and the K-edge images obtained from the three sequential acquisitions, after computing the differences between the images with N^+ and N^-.

Next, the author performed the same procedure but using phantoms in order to test the three types of patterns. The phantoms were used to evaluate the patterns since the movement factor that causes noise doesn't exist. The analysis of the results presented in [7] reveals that there are no significant differences between the three patterns of thresholds.

The method used to evaluate the results was CNR, which is the contrast to noise ratio. The pattern that presented the best CNR is the composite pixels in columns. The CNR of the image resulting from the three scans is $\sqrt{3}$ times larger than with composite pixels. This way, it is concluded that in terms of evaluation, the composite pixels, acquisition in one scan seems to be much better than the acquisition in three different scans.

3.3 Image Reconstruction

The aim of CT algorithms is to reconstruct an attenuation map from the projection measurements. Those measurements suffer from background effect as noise. Most of the reconstructions methods developed ignore the poly-energetic nature of the radiation. The conventional method for reconstruction from projections is an analytic method, the filtered backprojection.

The main disadvantage of this technique is the inability to account for the image noise that results from Poisson statistical variations in photon number across the image plane. Despite the disadvantages, FBP is a robust and fast approach which has been used by several research groups.

Since The first study where it was developed an iterative reconstruction algorithm, several studies have been made and have proved to have potential to improve the image quality and noise reduction. Iterative methods are able to use prior information as missing data or irregular information, [22] [34]. These algorithms were found to have more advantages when compared to the FBP-based methods and they allow integrating several physical models as, for example, performing the modulation of the artefact causes. Statistical algorithms incorporate counting statistics of the detected photons into the reconstruction process. ML-EM is the traditional statistical algorithm normally used, and the CPPM used it in [32], and Philips Research Europe in [24]. The reconstructed images obtained with this method have tendency to be noisy as the number of iterations increases.

Several research groups implemented Total Variation regularization as [35], where they used to duality-based algorithm. That paper suggests the application of gradient projection (GP) algorithms to the dual formulation. Thus, the use of model-based iterative reconstruction, which uses the prior information needs a number of iterations that depends on the measured object. However the demonstrated results proved that there was a dose reduction, [36] [37].

Iterative reconstruction methods have shown to have more advantages than analytic reconstruction methods. However, the acceptance of iterative reconstruction methods is a topic that several research groups are still working on. This is because reconstructed images showed different noise patterns and some artefacts expressed themselves differently comparing to analytical reconstruction methods. The state-of-art on this subject concerns the reconstruction method during the acquisition of CT images. Iterative reconstruction is performed when the patient is submitted to the radiation, and the acquisition system is implementing this reconstruction in order to visualize the images. Therefore, as stated in several articles, iterative reconstruction showed to be a good method to reconstruct the images, [38] [39] [36] [37] .

In this work, the spectral CT images are acquired using the filtered backprojection method. Iterative reconstruction has been proved to be a reliable method in acquiring tomographic images using prior information. Since the main goal of this research project is to estimate unknown measurements from partial measurements in the tomographic images, iterative reconstruction methods will be used to recover the missing information. One of the methods proved to be very successful is the Total Variation regularization, and in the next section it will be shown how this method was applied, not in the acquisition of CT images, but on their recovery.

Chapter 4

Materials

The objective of this project, as stated, is to study the composite pixels and improve the K-edge imaging at full spatial resolution. Since the images used to perform the methods were acquired using CPPM technology, the technology developed, PIXSCAN and XPAD3 will be detailed. After applying the reconstruction methods, a 3D reconstruction method developed by the CPPM is also applied. In order to evaluate the different methods, several images were used. These images have different features when compared to one another; some of them have more details and others are smoother. In the previous section, in addition to showing the procedure employed to evaluate the best method, it was also possible to correlate the method to the image features. This way, three images were used: simulated phantom image, the MOBY image, and real data images acquired by CPPM technology.

There is also reference made to the use of masks, being these used to recreate composite pixels. In this section, the masks used will be shown, as well as how they were applied to the images.

4.1 Micro-CT at CPPM

CPPM developed a micro-CT system named PIXSCAN, which is a small animal X-ray CT scanner based on an ultra-fast hybrid pixel detector, XPAD3. This system acquires 360 images that correspond to the projections, which are reconstructed using the 3D reconstruction software developed by the CPPM.

4.1.1 XPAD3 camera

As has already been mentioned, the photon counting approach is capable of discerning and process each single photon in addition to counting them. The hybrid approach allows the choice of energy according to the x-ray energy. XPAD3 is the third generation of X-ray photon counting imaging chip to be connected to a pixel sensor. This detector was developed by the imXgam group at the CPPM in collaboration with the group of Institute Néel in charge of the D2AM beam line at ESRF and the detector group at SOLEIL.

The XPAD3 characteristics are given in the **Table 4.1**, [4] [16]. The main components of the chip are: a matrix of 9600 pixels which are organised in 80 columns of 120 cells each, a digital interface that allows the transmission of the data and to control the pixel behaviour, and the third part is the functional part which has general purpose blocks.

Table 4.1: Characterizations results of XPAD3

	XPAD3
Number of pixels	9600
Pixel size	$130 \times 130\ \mu m^2$
Counting rate	$\leq 10^6$ photons/pixel/second
Cheap readout	$<$ 1ms

Each pixel is divided into two sub-cells, one for the analogue front-end electronics and the other for the digital data processing and the readout. Both parts are surrounded by guard rings in order to isolate them one from the other. The front-end collects charges from the sensor, which is converted into voltage pulse being this voltage then converted into current by the operation transconductance amplifier. The second part is the selection stage, where a current mode compensation for fixing the energy threshold is used. The third and last part is the digital part, where data counting, data overflow and configuration data is managed.

The XPAD3 model that is integrated in the micro-CT system used at CPPM has 8 modules of 7 chips. Each chip follows the characteristics described on the Table, which causes the camera to have an area of 120 x 75 mm^2. In the **Figure A.2** and **Figure A.1** of **Appendix A** is presented the images that represent the real picture of the XPAD3 detector and the XPAD3 camera enclosed in a box.

4.1.2 PIXSCAN prototype

The PIXSCAN is a cone beam micro-CT installed in a box which prevent X-ray exposure of the surrounding area, [40] [11]. In principle, the micro-CT has three components, the hybrid pixel detector, a rotating support and the X-ray source, as seen in the **Appendix A** by **Figure A.3**. During the acquisition, the object is rotating in order to change the angle of projection desired by the user.

4.2 Images

In order to evaluate the different reconstruction methods, images with different characteristics were used. To discover the best method to recover the missing data and provide good spatial resolution, it was necessary to evaluate the methods in different aspects: smoothness, amount of detail, edges and colour. Thus, four images were used: MOBY, simulated phantom and real data acquired by the CPPM technology.

4.2.1 Simulated Phantom

Images which contain small amount of detail were used to evaluate the reconstruction methods. These images are simulated phantoms, which resulted from the program developed by Mathieu Dupont, at CPPM. Some tools were developed in order to perform these simulations, a library from NIST data was created which consists on a database that lists the cross sections of the periodic table elements of a program responsible for handling the data. All the codes made to simulate the phantoms were in Python, [4].

Two tools were developed: a volume creation tool and a projection/reconstruction tool. The reconstruction method chosen was an analytic method: FDK, as presented in Chapter 2. The phantom created for this work has six spheres with different compositions. The different composition was made in order to simulate an acquisition of a human body using contrast agents.

The projections are made from the volumes built volumeCPP and therefore from 3D volume, thereby the calculations of the intersection distances is performed in a voxel matrix in three dimensions. For each energy bin E of the spectrum $I(E)$, the volume will be calculated using the procedure described above. Then, the final projection is the sum of the projections calculated for each bin, whose algorithm is shown in [4]. The scales of the projections are given in number of photons, where $\sum_j I_{o,j} = 2.22 \times 10^6$ in the polychromatic case. In order to simulate realistic acquisitions, noise was added to the data around the average $I_{o,j}$ for each bin. This procedure was made for 360 projections, and therefore, it was applied a reconstruction method.

Figure B.1 presents the configuration of the phantom created, that contains 2 balls of Iomeron, 2 balls of silver nitrate, 1 ball with water and 1 ball with bone. The configuration of this phantom is presented in **Appendix B.1**.

The three energy spectrum $I(E)$ used were chosen based on the material used inside of the spheres. This way, the three ranges applied were: 21.0 – 25.5 keV, 25.5 – 33.2 keV and 33.2 – 40 keV. As stated in Chapter 2, the choice of energies is based on the K-edge energy of the materials that will be visualized in the reconstructed images. The energy ranges used include two material K-edge, Silver that has a K-edge at 25.5 keV and Iodine at 33.2 keV For each range of energy, 360 projections was simulated. **Figure B.4a** represents the simulated phantom image that results after applying the composite pixels concept. This image is a coloured image, which has three dimensions, as stated, the first corresponds to the number of rows, the second to the number of columns and the third is the colour channels. Therefore, this image consists in coupling the three images acquired with the three energy ranges presented. Besides the analysis of these images, in this work, the impact of reconstruction methods in the images that results from the 3D reconstruction methods will be studied. Therefore, the original Simulated phantom images that results from the 3D reconstruction method and the images acquired at each energies are presented in **Appendix B.1**. The coloured image was recreated by coupling the three images acquired at the three energy ranges.

4.2.2 MOBY phantom

MOBY phantom was used in order to simulate a real acquisition of a mouse. This phantom was developed for the evaluation and optimization of small animal imaging. Imaging techniques have emerged very quickly, which brought the need for a tool that can be used in technique

testing, evaluation and comparison. Thus, highly realistic phantoms are required so the results achieved be an indicative of what would occur in actual patients. Several 4D extended phantoms have been developed by Dr. Paul Segars, [41]. Thus, MOBY provides a virtual model of the mouse's anatomy and physiology. Since the exact anatomy of the phantom is known, the main concern will be just quantitatively and improve devices and techniques. CPPM used the MOBY phantom and used this to simulate a mouse to which was injected intravenously with Iomeron. The simulation consist in 360° projections, the coloured MOBY image acquired at projection 1° is demonstrated in **Appendix B.2**. For this project, it was used the 360° projections to test the techniques, which were followed by 3D reconstruction using the reconstruction software. The images acquired have 3 dimensions (x, y, z), where z represents the energy band.

As in the previous section, MOBY image was acquired at three different energy ranges, 21.0 – 25.5 keV, 25.5 – 33.2 keV and 33.2 – 40 keV. The maximum value of the MOBY images that will be used to perform normalization is 6.33×10^5.

The 3D reconstructed image that will be used as the reference image in order to evaluate the 3D reconstructed images is present in **Figure B.5b** which is the coloured image. The 3D reconstructed MOBY images result from the 3D reconstruction method developed by Mathieu Dupont.

4.2.3 Real Data

This work was made in order to evaluate the reconstruction methods, and see which one should be used according to the type of image that is being analysed. The images showed above are images with no presence of noise and easy to manipulate. This way, it was important the use of real data that was acquired using the CPPM technology. The images acquired using PIXSCAN are presented in the **Appendix B.3** in **Figure B.6**. In these images, the noise was not simulated, which means that it was not applied a random function to the image. The images showed in **Figure B.6** represent the projection of the upper view of several cylinder shaped objects and **Figure B.6b** presents the 3D cylinder image that resulted from the 3D reconstruction program developed at the CPPM. The cylinder structures contain Iodine, Silver nitrate and Copper sulfate, which is demonstrated by the several colours present in **Figure B.6b**. Therefore, the green structures are related to the Silver nitrate, the purple ones to Iodine and the other two to Copper sulfate. The different colours are caused by the use of the composite pixels which will be explained in the Discussion Chapter. This image presents several circles lines that result from the result of the 3D reconstruction of artifacts caused by the pixel configuration of the XPAD3 detector.

4.3 Mask

As stated in the previous section, before performing the reconstruction methods, a mask was applied to the images. These masks were used in order to recreate the concept of composite pixels. This way, as mentioned, masks were used initially to evaluate how many ranges of energy should be applied.

Since the main goal of this project is to test patterns of composite pixels, one pattern that

is important to use because of the amount of literature that exists on it is the Bayer filter. This pattern has three channels and it is used in most part of digital cameras. The cameras have a monochrome sensor which is covered by a color filter array (CFA) such that the incoming light is spectrally sampled. The process involved in the acquisition of these filters takes in the concept of composite pixels. The Bayer filter array is the most popular type of mosaic, where half of the pixels have a green colour, the colour to which the human eye is more sensitive. The red and blue colour are arranged in rows and columns, with one missing pixel in each direction. This mask is commonly used to test the Demosaicing methods.

Then, two types of masks with 3 channels were used: a mask with random pattern, and other with a regular pattern. The random pattern was created using Matlab, which was made just one mask with a random pattern. The random pattern is commonly used in processing imaging in order to reduce the aliasing artifact. With regard to the mask with regular pattern, the Bayer colour filter array (CFA) was used. **Figure 4.1** presents the masks used, the first is the mask with the regular pattern (Bayer CFA), and the second represent the mask with the random pattern.

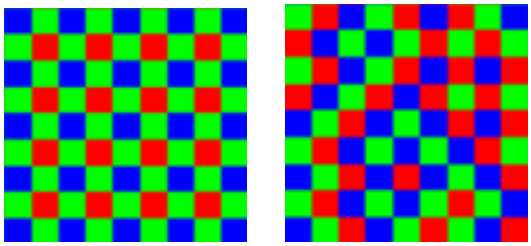

(a) Regular pattern: Bayer mask **(b)** Random pattern

Figure 4.1: Masks that simulate the composite pixels

Figure 4.2 represents the division of the Bayer filter into three sub-masks. In this work, sub-mask and mask will be two important concepts. Thus, mask is the type of filter used and the sub-masks depend on the number of channels / colors that the filter has. The Bayer filter has three colors, and so three sub-masks.

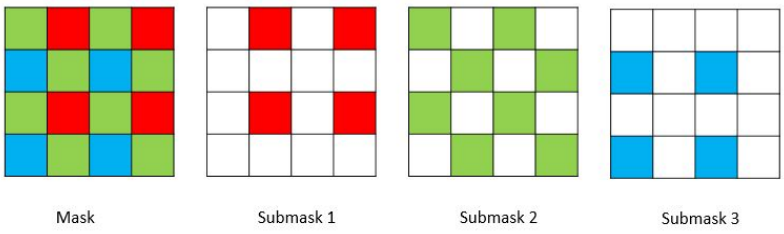

Figure 4.2: Simulated Bayer mask and corresponding sub-masks

In this study, the colors and the fact that the green color is more sensitive to the human eye is irrelevant. These filters will be used since they showed to have very good results when Demosaicing methods are applied, where the missing color components at each pixel are estimated. This way, each color will indicate an energy range and therefore the pixels with green color that represent a specific energy range will provide more information.

Chapter 5

Methods

In this section the methods and procedures used in order to improve the visualization of the images acquired by the CPPM technology will be demonstrated. The main goal of evaluating the reconstruction methods is to define an optimal protocol, where after acquiring the images, the best reconstruction algorithm will be performed. This Chapter has two parts, in the first the reconstruction methods applied in this project will be addressed; the second part consists in the experimental procedure that is in the basis of this project was described.

5.1 Reconstruction Algorithms

Clinical images which are acquired by detectors are subjected to several artefacts such as noise, missing data and artifacts related to the patient. Therefore, after the acquisition of these images it is necessary to perform some processing in order to recover and improve the quality of the image in such way that a neutral observer would not notice any artifacts. This way, several methods were applied to study which method is better to use in the images acquired by the XPAD3 detector in order to acquired better spatial resolution. In this section, reference will be made to the three reconstruction algorithms: Linear Interpolation, Inpainting and Demosaicing.

The general definition of interpolation refers to the recovery of the values of missing locations and it is one of the fundamental operations in image processing, since it helps improving low resolution images of CT scans. Interpolation methods are divided into two categories, deterministic and statistical interpolation techniques. Deterministic interpolation techniques assume a certain variability between the points, and statistical interpolation techniques approximate the signal by using methods that minimize the estimation error. The division can also be made taking into account the way that the interpolation treats the image information. Thus, interpolation methods can be grouped into two categories, adaptive and non-adaptive methods. Adaptive methods are based on the type of features that will be recovered, this way, they depend on what the method will interpolate, for example sharp edges. Non-adaptive methods treat the pixels equally.

Although in this work was used one type of deterministic and non-adaptive interpolation method: Linear Interpolation. Demosaicing and Inpainting methods are adaptive interpolation methods. **Figure 5.1** represents a scheme where it is presented how the interpolation methods were divided in this work. Inpainting and Linear Interpolation are methods that recover missing

data using information from the same image. Demosaicing methods, as will be described in the next section, interpolate the missing data using pixels from different images. As shown in the **Appendix B**, each image will be decomposed in three images that will be called, in this work, bands. In the Demosaicing methods the interpolation of the final image will be done using the correlation of pixels from the three bands: $(x, y)_{I1}$, $(x, y)_{I2}$ and $(x, y)_{I3}$, while, as stated, linear interpolation and Inpainting methods will recover using information from the same band.

To introduce the reconstruction methods, the inverse problem concept will be presented. This consists in mapping objects of interest and acquire information about these objects. Since the goal of the reconstruction methods used in this work is to recover missing data, the methods will be seen as an inverse problem. The mapping objects are the missing pixels which will be recovered using the partial measurements.

The methods used to interpolate missing data are demonstrated in **Figure 5.1**. The Inpainting methods that will be described are Sobolev and Total Variation minimization, and Demosaicing will be the only method described that recovers missing data across different images. Two approaches will be presented: Demosaicing by frequency selection and Demosaicing using total variation minimization.

The reconstruction methods were applied using Matlab as a programming language. In this section, the methods theory and how these methods were implemented in code will be explained.

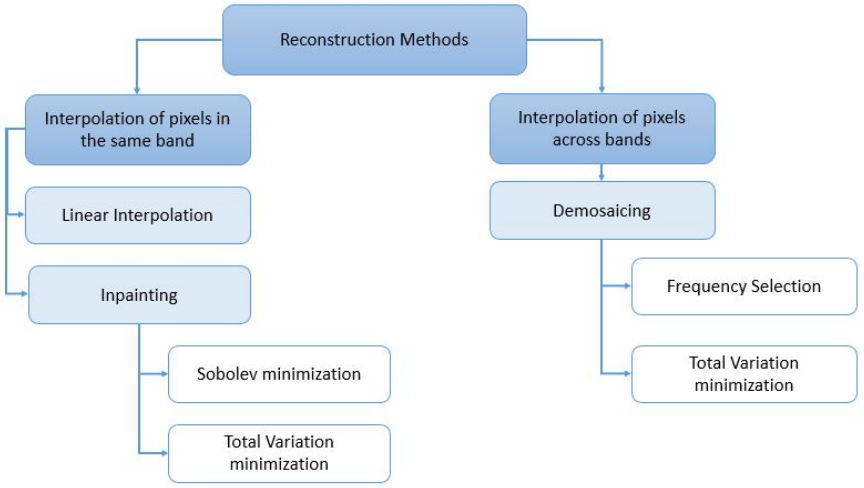

Figure 5.1: Scheme of the Reconstruction methods used in this project

5.1.1 Linear Interpolation

Linear interpolation is the most common method used in Tomography to recover missing data. This method consists in defining a function that takes specific values at specific location. Linear interpolation is the simplest method of getting values at positions in between the data points, which are joined by a straight line segment. Each segment can be interpolated independently. As stated, the software used to perform the algorithm was Matlab. First, it was applied a function which saved the coordinates where the sub-mask has value zero. For example in **Figure 4.2**, the function will save the coordinates of the not coloured pixels. For each sub-mask,

the coordinates will be saved. A vector z , with dimension $(L, 1)$ is created and will be filled with image values of the corresponding coordinates where the sub-mask is zero.

After selecting the points that want to be interpolated, the interpolation function is applied. For this purpose, the griddata function was used it was chosen the simplest method, the linear interpolation.

5.1.2 Inverse Problems

Inverse problems are, in general, "ill-posed" and incomplete, so it becomes necesssary to add information to achieve the solution formulation, [42] [43]. In this setting, the methods try to recover a high resolution image $f_0 \in \mathbb{R}^N$ of n pixels from a set of $p \leq n$ noisy linear measurements. Thus, the mathematical formula that translates the inverse problems is given in **equation 5.1**.

$$y = \Phi f_0 + \delta \in \mathbb{R}^P \quad \delta \sim \mathcal{N}(0, \sigma^2) \tag{5.1}$$

Where Φ is a linear operator that accounts for missing pixels so that the measured data y only captures a portion of the original data f that wishes to be recovered. Thus, in this work the operator consists in the pixels with zero value, which come from the masks that are applied to the images. The parameter δ represents the additive noise that is applied in the images in order to simulate real data acquired. Since the methods are seen as linear models, the noise is assumed as random variables which are uncorrelated and all have zero mean and the same variance.

To solve an ill-posed problem, prior knowledge about the images that will be restored is needed. The prior information should help in the recovery of the missing information. Regularization operator is commonly used as prior information which is responsible for ensuring the smoothness of the solution, causing the problem to become well-conditioned. Thus, the ill-posed problem of recovering an approximation of image f_0 from noise measures $y \in \mathbb{R}^P$ is regularized by solving a convex optimization problem, [42]. Therefore, the regularized solution f^* of the inverse problem is written in variation form as the formula given in **equation 5.2**, [42] [44].

$$f^* \in \underset{f \in \mathbb{R}^N}{\operatorname{argmin}} \frac{1}{2} \|y - \Phi f\|_\Omega^2 + \lambda J(f) \qquad \Omega = \{(i,j) \mid y(i,j) = f(i,j)\} \tag{5.2}$$

Where $\|y - \Phi f\|^2$ is the data fitting term and *J(f)* is a convex prior. The parameter λ is a Lagrange multiplier which is related to the importance of the two terms and its setting is a non-trivial task in practical situations. This parameter has positive values and measures the trade-off between a good fit and a regularized solution and Ω represents the space of good pixels. Thus, the solution found depends on the type of regularization chosen, which will consist in the minimization of the parameter, *J(f)*.

Inpainting

Image Inpainting methods are restorations methods used in order to remove damage or reconstructing missing portions of images, [42] [45]. This procedure allows the recovery of images where some data is missing or the removal of unwanted elements present in the image, in order to approximate the original appearance. Inpainting algorithms are solved as an inverse problem, since it corresponds to interpolate missing pixels in an image using information from the surrounding pixels, [45] [46]. Thus, this operation corresponds to the following masking operator given in **equation 5.3**.

$$\Phi f_{ij} = \begin{cases} f(i,j) & \text{if (i,j)} \in \Omega \\ 0 & \text{if (i,j)} \notin \Omega \end{cases} \tag{5.3}$$

Where $i, j = 1, \ldots, n$ translates the pixel of the image that one wants to recover. This operation consists in reading the pixels, determining which are the pixels that will form the final image that one wants to recover, and the pixels that don't have information which will have a value of zero. Thus, Inpainting operation is modelled by a diagonal operator over the spatial domain, and it is an orthogonal projector $\Phi^* = \Phi$.

Recovering the information as an Inpainting problem has advantages when compared to simpler alternatives. One approach that is less complicated and doesn't need a lot of computation, is facing **equation 5.1** as a least square problem, which solution is given by **equation 5.4**.

$$f^* \in \underset{f \in \mathbb{R}^N}{\operatorname{argmin}} \|y - \Phi f\|_\Omega^2 \tag{5.4}$$

The Least Square method takes in consideration the statistical features of the noise and pixels that belong to the Ω domain. Since the missing pixels are out of the Ω domain and are not taken into account in the minimization, they will remain constant at the value given at their initialization. The principle used in least square problems does not consider the information of missing information, which will not generate any improvement in the recovery of missing data since it doesn't give any additional information about the image.

This way, Sobolev and Total Variation regularization were tested. Each method tested images with the presence and absence of noise. Inpainting using Total Tariation and Sobolev as a non-constrained problem as well the mathematics involved will be explained. The second approach treats the Inpainting as a constrained problem, which involves complex mathematics formulations and due to that a toolbox created which is found in [47] [48]. This toolbox was used in order to avoid the problem of the first Inpainting approach: the computing time to solve the regularization problem that took over 2 days to find a solution. Therefore, the explanation of this toolbox is demonstrated in the **Appendix E**, where it is presented the main concepts and mathematical formulations involved.

Sobolev Method

The simplest prior model assumes a uniform smoothness of the image. An example of this type of ill-conditioned model is the Sobolev regularization, [42] [44]. The Sobolev image prior is a quadratic prior given in **equation 5.5**.

$$J^{sob}(f) = \sum_{x} \|\nabla_x f\|^2 \tag{5.5}$$

Thus, recover problems can be formulated as a convex optimization problems. Where $\nabla_x f$ is a finite difference approximation of the gradient f at pixel x. The gradient vector at point x is defined in **equation 5.6**.

$$\nabla f(x) = \left(\frac{\partial f(x)}{\partial x_1}, \frac{\partial f(x)}{\partial x_2}\right) \tag{5.6}$$

The parameter ∇ is defined as a vector differential operator, when applied to a scalar field, it is called gradient. Since the image $f(x)$ is a vector field, the scalar product of ∇ with the image, the resulting operation is called as divergence of the vector field. The operation is called Laplacian. Thus, this operation was performed using the gradient and divergence function. The functions used are presented in **equation 5.7**. This way, in **equation 5.7** is the gradient of the Sobolev regularization.

$$Laplacian \;=\; \Delta f(x) = div\left(\frac{\partial f(x)}{\partial x_1}, \frac{\partial f(x)}{\partial x_2}\right) \tag{5.7}$$

In order to test the method, it was applied to two situations, a noiseless and noisy case. In the noiseless case, to constrain the solution to lie in the space $\{f \in R^N \;\; y = \Phi f\}$, an orthogonal projector is used, as demonstrated in **equation 5.8**.

$$\forall x, \;\; P_y(f)(x) = \begin{cases} f(x) & \text{if x} \in \Omega \\ y(x) & \text{if x} \notin \Omega \end{cases} \tag{5.8}$$

Since $J(f)$ is differentiable and convex, the solution of **equation 5.2** can be computed through a gradient descent. This way, taking into consideration the orthogonal projector, the Sobolev regularization given in **equation 5.5** is solved using a projected gradient descent. Thus, the algorithm iterates until achieving the convergence, the solution is given in **equation 5.1.2**.

$$f^{(k+1)} \;=\; P_y\left(f^{(k)} \;+\; \tau \Delta f^{(k)}\right) \tag{5.9}$$

Where P_y is the projected gradient descent, τ is a free parameter that has positive values which is the step-size. This parameter should be adapted to the noise level, whose increasing its values imply a more aggressive denoising. In a practical situation, it was necessary to test several τ values, since it depends on the type of image that is being used and the level of noise. There is not a direct relation between the noise and this value. The operation $\Delta f^{(k)}$ is the

differential operator and is given by the divergence of the gradient of a function. This way, the operation $\Delta f^{(k)}$ is calculated by the expression given by **equation 5.7**.

The formulations used to perform the Sobolev regularization with presence of noise use the same assumptions as the previous scenario, however it doesn't use the orthogonal projector since the constraint of the solution belongs to the space $\{f \in \mathbb{R}^P \;\; y = \Phi f + \delta\}$. The regularity operator $J(f)$ is differentiable and convex, thus gradient descent is the operation used to achieve the solution of the **equation 5.2**. This way, the Sobolev regularization formula in the noisy cases is given by the **equation 5.10**.

$$f^{(k+1)} = f^{(k)} \; - \tau \Big(\Phi^*(\Phi f^{(k)} - y) \; - \lambda \Delta f^{(k)} \Big) \tag{5.10}$$

Where the descent step size $\tau > 0$ should be small. The value of λ is very difficult to tune, since it will depend on the level of noise and the type of image that one wants to recover. Thus, it is necessary to make several attempts on the value of λ since this weigh the influence of the data fitting term and the regularization term, which is adapted to the noise level and to the regularity of the unknown image. This task is not trivial, which makes very difficult to find the best value of λ. Due to the difficulty of finding the best value, the minimization of the regularity parameter will be calculated in a different way. The regularity parameter will not be seen as differentiable, which makes the simple gradient descent not usable to solve **equation 5.2**. This way, the algorithm purposed by [47] uses an optimization algorithm which is presented in the **Appendix E**.

The stop criteria used in the iterative algorithm was the difference between the resulting SNR of the two images as to be lower than 1×10^{-3}. A loop, which computes the Inpainting method until the condition is satisfied, is generated. Thus, at the end of the loop the SNR of the resulting image produced, which value is saved as SNR_B is computed. In the next iteration of the loop, it is computed the SNR of the resulting image, which is the SNR_A and until the difference between these two values is bigger than1×10^{-3}, the iteration will continue.

The stop criteria for when the images have noise is the same, but a maximum number of iteration is added. As stated, the goal of this method is to achieve the convergence, **Figure 5.2**, shows a graphic representation of the gradient descent method that is applied in the regularization.

The number of iterations was a problem that had to be faced during the implementation of these methods. This because the step size chosen was not the same for all the images used, and when it was chosen it was necessary to verify if the convergence would be attainable. The stopping criteria was satisfied for all images due to the number of iterations but the convergence was not always reached. This happened because it was not found the perfect step size value in order to achieve the final value, originating what is demonstrated in **Figure 5.3**. After applying the methods to several images and after several attempts, it was concluded that it would be impossible to find convergence of the images with the same number of iterations, therefore an average number of iteration was created for all the images.

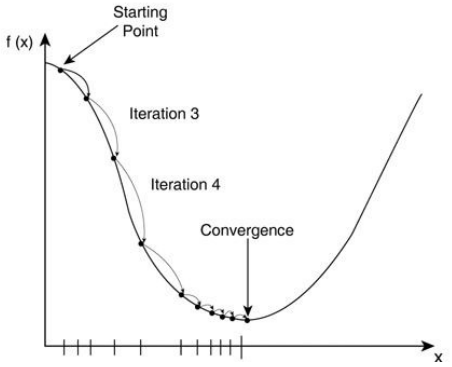

Figure 5.2: Successive steepest descent iterations showing the improvement in the estimates until the process converges at the global minimum, [8]

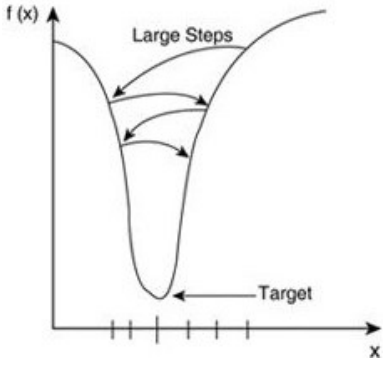

Figure 5.3: Problems with the learning rate:oscillation, [8]

Total Variation Method

As stated, the goal of this work is to recover missing data from the images acquired by the detectors. The relative ease of implementation of smooth minimization methods as Sobolev regularization, has traditionally favoured the use of differentiable images. However, typical data in CT have sharp features that should not be smoothed with the regularization, [42] [46] [49] [50] [44]. This brought the emergence of theoretical studies that face constrain as non-differentiable which make the image recovery problem more appropriate. These methods have the ability of restoring sharp features that is, of minimizing the unjustified oscillation without blurring sharp features.

Total Variation regularization was introduced by Rudin, Osher and Fatemi, named as ROF model, and it takes into account the discontinuities in images. This regularization is given in **equation 5.11**, [49] [50].

$$J^{TV}(f) = \sum_{x} \|\nabla_x f\|_{TV} \tag{5.11}$$

The gradient of the Total Variation regularization for a non-zero f, [46] [49] [51] [50], is given in **equation 5.12**.

$$Grad\, J^{TV}(f) \;=\; div\Big(\frac{\nabla f}{\|\nabla f\|}\Big) \tag{5.12}$$

The Total Variation regularization defined in **equation 5.11** is a convex but non differentiable function of the image f, so the regularization problem given by **equation 5.2** cannot be solved using a gradient descent. The gradient computed by the **equation 5.12** is not defined at a pixel x has $\nabla f(x) = 0$. Thus, Total Variation prior is difficult to minimize, and its gradient is not well defined. This singularity can be avoided by re-defining the TV regularization parameter by adding a small positive constant. Therefore, a smoothed total variation prior J^{ϵ}_{TV} is used to solve the **equation 5.2**. This prior as Sobolev method, uses a gradient descent, **equation 5.13**, [46].

$$J_{TV}^{\epsilon}(f) \;=\; \sum_{x} \sqrt{\|\nabla_x f\|^2 + \varepsilon^2} \tag{5.13}$$

J_{TV}^{ε} is differentiable with respect to f and $\sqrt{\|\nabla f\|^2 + \varepsilon^2}$ is a smooth function. This way, the gradient of J_{TV}^{ϵ} is given by **equation 5.14**.

$$Grad\, J_{TV}^{\epsilon}(f) \;=\; div\Big(\frac{\nabla_x f}{\sqrt{\|\nabla_x f\|^2 + \varepsilon^2}}\Big) \tag{5.14}$$

Thus, this modified TV regularization is a differentiable function, and therefore the gradient and the Hessian of the modified objective function represented in **equation 5.2**, is given now in **equation 5.15**.

$$f^* \;\in\; \underset{f\in\mathbb{R}^N}{\operatorname{argmin}} \; \frac{1}{2}\,\|y - \Phi f\|_{\Omega}^2 \;+\; \lambda J_{TV}^{\epsilon} \tag{5.15}$$

The trade-off in choosing ϵ is the quality of restoration of image edges versus the speed of convergence. The smaller the parameter ϵ is, the higher the quality of the recovery of image edges, [51]. Though, the convergence of the iterations is slow, since **equation 5.13** is closer to the original non-differentiable objective function in **equation 5.11**. This way, choosing a small ϵ makes the function closer to a minimization of the total variation, but makes the computational unstable.

As stated, two scenarios were tested, the noiseless and the noise case. In the noiseless case, the same assumptions are made as in the Sobolev regularization. For smoothed TV regularization, the problem is solved using projected gradient descent,[51], $GradJ_{TV}^{\epsilon}(f)$. The formula used to solve is given in **equation 5.16**.

$$f^{(k+1)} \;=\; P_y\left(f^{(k)} \;+\tau\times\; div\left(\frac{\nabla f^{(k)}}{\sqrt{\|\nabla f^{(k)}\|^2 + \varepsilon^2}}\right)\right) \tag{5.16}$$

For the smoothed total variation regularization to converge, the value of $\tau < \epsilon/(4 - 1\times 10^{-1})$ needs to be imposed. This shows that smaller time steps and thus a slower algorithm is required, thus confirming the fact that the computation time is very long. Both parameters are correlated with the noise, but as stated, in practical situations it is very difficult to find the best values taking in consideration the type of features that want to be recovered. The operation $\Delta f^{(k)}$ is calculated by the expression given by **equation 5.7**. When the images have noise, the orthogonal projector is no longer applied since the constraint that the solution belongs to the space $\{f \in \mathbb{R}^P \;\; y = \Phi f\}$ is not correct.

The formula describing the iteration to achieve the convergence of total variation regularization is given in the **equation 5.17**, [42].

$$f^{(k+1)} \;=\; f^{(k)} \;-\; \tau\Phi^*(\Phi f^{(k)} - y) + \lambda\,\tau\; div\left(\frac{\nabla f^{(k)}}{\sqrt{\|\nabla f^{(k)}\|^2 + \varepsilon^2}}\right) \tag{5.17}$$

Where $\epsilon > 0$ and the choice of the parameters λ and τ are needed. The value of all the parameters depends on the type of image used, thus making it necessary to make several attempts to evaluate which one showed best results. In noisy images, the value of ϵ was in general 1 or very close to 1, and the value of τ was usually between $(\epsilon/(4 - 1 \times 10^{-1}) \cdot 1 \times 10^{-1}) < \tau < (\epsilon/(4 - 1 \times 10^{-1}))$. Due to the difficulty of finding the values of λ, a vector of values which has possible values numbers for this parameter was made. Because of the number of parameters that are needed to find the best value in order to reach the convergence, these methods are very time consuming and a big memory is needed.

The stop criteria used to perform the total variation regularization was the same used in the Sobolev regularization. The same situation explained with regard to the value of step size and the number of iterations was observed, this way, it was also applied a maximum number of iterations.

Demosaicing

Digital cameras form coloured images using a monolayer matrix of photocells, in which each element is covered with a colour filter, [52] [53] [54]. Each pixel contains information about only one of the colours, while the colour image contains all the components for each pixel. The most common filter used is the Bayer Filter. In this filter, each pixel contains information about one colour (red, blue or green), and each pixel of the colour image will contain all the three colours. In digital cameras, each colour filter is associated to a single pixel and to a corresponding photo sensor of the pixel, which reads a specific colour wavelength centred on a particular desired colour (blue, red or green). The combination of all the colour filters forms a colour filter array (CFA). Thus, digital cameras place a colour filter array in front of the sensor which records just one colour at each pixel site. The captured image is a mosaic of a single-colour pixel, [53] [54].

CFA- based camera architecture and the captured mosaic images trigged the development of an algorithm that recovers the original three colour channels for each image pixel. The name given to these algorithms is Demosaicing. Therefore, Demosaicing consists in the process of restoring the missing colour information in such an image through color channel crosssing, [53]. To estimate the colour of each pixel in a true colour image, it is necessary to determine the values of the two missing colour components at each pixel in the CFA image.

The snag of using the method referred before is that it treats the images independently, when in reality the three images are highly correlated. Thus, the use of these method leads to the emergence of artifacts such as blurring and generation of false colour, also referred to colour aliasing. One solution used to solve these artifacts is the concept of computing hue as the ratio of two colours. Several studies showed that it is more reliable to interpolate colour ratios instead of R, G and B. There is a huge amount of literature on Demosaicing, however most of these methods are developed under the assumption of noise-free data, whose performance has shown not to be reliable since their non-linear mechanisms are generally not robust to noise.

To understand how the Demosaicing method is applied to this work, it is important to do a brief summary of the colour interpretation and how this contributed to the development of the Demosaicing methods. In the case of the human virtual system, [55], it is known that it uses three different photoreceptors with three different spectral sensitivities in order to reproduce colour

sensation. Taking this assumption, an artificial system needs to acquire the energy of three spectral bands and to display it with a three spectral band modulation in order to reproduce colour sensation. Due to the fact that only one colour sensitivity per spatial location is available (mosaicked image), the spatial and chromatic information are mixed.

In this work, an approach made by Laurent Condat is presented, which uses a frequency analysis of the spatio-spectral sampling induced by the CFA. In this approach the images are seen as noisy images, thus the Demosaicing is performed together with denoising. This approach uses spatial Fourier transform information to develop a colour Demosaicing algorithm by selecting appropriate spatial frequencies. The frequency analysis of the sampling pattern induced by the Bayer CFA provides a simple way to reconstruct the luminance and chrominance channels. Thus, the main operations of this algorithm is linear filtering operations and denoising of the grayscale luminance image.

Luminance and chrominance signals will be defined, and how the mix of spatial and chromatic information is modelled as a spatial multiplexing of colour will also be explained. Since the method performed in this work uses the spatial Fourier transform to develop Demosaicing, the property of localizing luminance and chrominance frequencies in the Fourier domain will be demonstrated. Hence, this work will demonstrate the two algorithms developed by Laurent Condat and explain how they were applied to the same.

Luminance and Chrominance

Digital cameras and their image formation model were crucial in the production of the Demosaicing algorithm assumptions. As stated, colour images are defined by three-colour components at each spatial location. Then, a colour image I can be defined by three colour components C_i at each discrete spatial location, [55], thereafter this can be expressed as a vector of three dimensions for each pixel, as demonstrated in **equation 5.18**, .

$$I = \left\{ C_i(x,y) \ , \ i \in [R,G,B], \ \ (x,y) \in \ \mathbb{N}^2 \right\} \tag{5.18}$$

Each colour vector C_i coincides with the sampling of spatially (x, y) and spectrally variable input illuminance through a spectral sensitivity function, [55]. In Demosaicing algorithms, luminance is the information carried by the green pixels. The fact that the Bayer filter has more green colour contributes for the improvement of the spatial acuity. Thus, luminance is a scalar intensity image that contains achromatic information of the original image. The luminance signal can be estimated from $C_i(x, y)$ using the sum or the mean of the three colour components. Chrominance is the remaining three-dimensional vector that results after the extraction of the scalar luminance from the original vector. This way, the colour image I can be represented by the sum of a scalar (luminance) and a three dimensional vector representing the opponent colours (chrominance), which formula is presented in **equation 5.19**, [55] [53].

$$I \ = \ \{C_i(x,y)\} = \Phi(x,y) \ + \ \Psi_i(x,y) \tag{5.19}$$

This way, the mathematical formulation of the spatial multiplexing, also called the CFA

image, is given by **equation 5.20**, where $R(x, y)$ is a scalar image which has only one colour component per spatial location, [53].

$$R(x, y) = \sum_i C_i(x, y)\, m_i(x, y) \tag{5.20}$$

Where $m_i(x, y)$ are three orthogonal sub-sampling functions taking value of 1 if the colour i is present at position $(x, y) \in \mathbb{N}^2$ and 0 otherwise. These functions are also called modulation functions, which in the particular case of the Bayer CFA, $m_i(x, y)$ can be found in [55]. The modulation functions can be related with the probability of colour, p_i, in the CFA by the **equation 5.21**, [55].

$$m_i(x, y) = p_i(x, y) \; + \; \tilde{m}_i(x, y) \tag{5.21}$$

Where $\tilde{m}_i(x, y)$ is a modulation part with null mean value. Therefore, the CFA image, given by **equation 5.21**, can be rewritten as follows in **equation 5.22**.

$$R(x, y) = \sum_i p_i C_i(x, y) \; + \; \sum_i C_i(x, y)\tilde{m}_i(x, y) \tag{5.22}$$

The first part $\sum_i p_i C_i(x, y)$ is the luminance and $\sum_i C_i(x, y)\tilde{m}_i(x, y)$ is the chrominance, [55] [10]. As presented, the luminance term is not multiplied by the modulation function due to the fact that it is defined with full spatial resolution. The second term called chrominance, contains colour information that is spatially sub-sampled.

Therefore, **equation 5.22** proves that the spatial multiplexing of colour can be divided into two signals. The first signal is represented by the first term, luminance, this one doesn't depend on the spatial location, which makes it the term with the highest spatial frequency. Chrominance, the second term, changes with spatial location and defines a spectral difference, unlike luminance. Since luminance is a scalar, the percentage of the three colours that makes up the luminance estimator should be constant over all the spatial locations, [53] [10]. The studies presented in [56] show that in the case of Bayer CFA the luminance, $C_L(x, y)$, is defined as $(C_R(x, y) + 2C_G(x, y) + C_B(x, y))/4$. Colour measurements of each photoreceptor type were selected and multiplied by the modulation function in order to achieve the chrominance signal, [55] [10]. Thus, the expression of the CFA image can be rewritten using the luminance and chrominance signals, this is given in **equation 5.23**.

$$R(x, y) = \; C_L(x, y) \; + \; C_{chr1}(x, y)(-1)^{x+y} \; + \; C_{chr2}(x, y)\Big((-1)^x - (-1)^y\Big) \tag{5.23}$$

Where $C_L(x, y)$ is the luminance component, and C_{chr1} and C_{chr2} are the chrominance components. As demonstrated in [55] [56], the chrominance signal is composed by three opponent chromatic signals equivalent to red minus cyan, green minus magenta and blue minus yellow.

Given the **equation 5.23** of the spatially multiplexed colour image, the Fourier transform is computed in the images as given in **equation 5.24**.

$$\hat{R}(x,y) = \sum_i \hat{C}(f_x, f_y) \ * \ \hat{m}(f_x, f_y) \tag{5.24}$$

Where $\hat{\cdot}$ represents the Fourier transform and $*$ the convolution operator. The Fourier transform is also applied in the modulation functions, which localize luminance and chrominance in the frequency domain. Fourier representation is used to place the Bayer CFA into a spatial frequency representation which consists in placing the three colours onto a square grid. **Figure 5.4** shows the example used in the algorithm used in this work, where the amplitude frequency spectrum of a single-colour per pixel image is sub-sampled according to the Bayer CFA. Nine regions are identify in **Figure 5.4** and **Figure 5.5**, where the energy is concentrated. The center region corresponds to the luminance and the border regions to the chrominance. **Figure 5.4** is the Fourier representation of the spectrum of a mosaicked image. The frequency location of luminance and chrominance signals in the Fourier domain allow the estimation of these components by simply selecting the corresponding frequency domains, [10] [56].

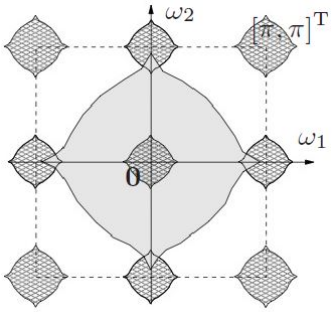

Figure 5.4: Schematic representation of the spectrum of a mosaicked image, [9].

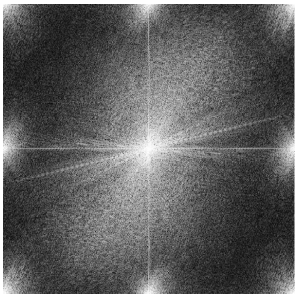

Figure 5.5: Spatial frequency representation of an image acquired through the Bayer CFA, [10]

Luminance is estimated by low-pass filtering, while chrominance is estimated by a high-pass filtering, **equation 5.23**. Thus, the high-pass filter on the colour spatially multiplexed image given by **equation 5.22**, results in a multiplexed version of the chrominance. The luminance presented before ($C_L(x,y)$) is an example of a luminance filter used in [9], therefore in the Demosaicing algorithm that will be presented and used in this work, the notation used to describe luminance and chrominance is different. In the next section where the algorithm used will be explained, it will also be specified the notation used by Laurent Condat, [57].

Demosaicing by Frequency selection

One notation is that the boldface letters denote vectors, $\mathbf{k} = [k_1, k_2]^T \in \mathbb{Z}^2$, where (k_1, k_2) are equivalent to the location (i, j) and (x, y), as was referred in the previous section. A colour is a vector of $\mathbb{R}^3$ and a canonical R,G,B basis of the colour space is defined by $R = [1, 0, 0]^T$, $G = [0, 1, 0]^T$ and $B = [0, 0, 1]^T$.

The colour image $\mathbf{u} = (u[k])_{k \in \mathbb{Z}^2}$ is defined as the ground truth to be estimated by the Demosaicing algorithm. The formula that express the colour of the pixel at a certain location includes the a variable $\mathbf{u}$ which is the colour of the pixel at location, and $\mathbf{k}$, and u^R, u^G and u^B

that are the components of u in the R,G,B basis. The expression that express a colout by the Demosaicing method is given in the **equation 5.25**, [57].

$$v[\mathbf{k}] = u^{X[\mathbf{k}]}[\mathbf{k}] \; + \; \delta[\mathbf{k}] \tag{5.25}$$

Where $X[\mathbf{k}] \in R, G, B$ is the colour of the filter in the Bayer pattern at location $\mathbf{k}$, and $\delta[\mathbf{k}]$ is the image noise and has the same property has stated in the inverse problems section. The orthonormal basis corresponding to luminance, red-green and blue-yellow chrominances are defined in the [58].

Therefore, taking the notation used before, the luminance presented by L is equivalent to $C_L(x, y)$, however, as stated, in this work, the notation used to describe these components is different than the one used in [57]. This way, the proposed basis is arbitrary but convenient to describe the spectral properties as demonstrated in the previous section, where it was also demonstrated that luminance and chrominance is a good system to characterize the Bayer CFA and that the mosaicked image is the sum of the modulated luminance and chrominance of the colour image to be estimated. In the same way, it was likewise demonstrated how the Fourier transform was applied to the colour image, **equation 5.26** demonstrated the Fourier transform of the image v, [57].

$$\begin{aligned}\hat{v}(\mathbf{w}) = \hat{u}^L(\mathbf{w}) + \frac{\sqrt{6}}{4}\hat{u}^{G/M}(\mathbf{w} - [\pi, \pi]^T) + \frac{\sqrt{2}}{4}\hat{u}^{R/B}(\mathbf{w} - [0, \pi]^T) - \\ \frac{\sqrt{2}}{4}\hat{u}^{R/B}(\mathbf{w} - [\pi, 0]^T) + \hat{\delta}(\mathbf{w})\end{aligned} \tag{5.26}$$

The frequency analysis of the spatio-spectral sampling induced by the Bayer CFA is demonstrated in **Figure 5.4**, and consists in separating the three images u^L,$u^{R/B}$ and $u^{G/M}$, taking into consideration the noise. Paper [9] denotes v_0 the noise-free mosaicked image and v the colour image referred previously. Therefore, another notation will be done in order to describe the image that results from the Demosaicing, in which d_0 is referred to the v_0 demosaiced and d corresponds to v. The formulation that results is demonstrated in the **equation 5.27**.

$$d = d_0 + e \tag{5.27}$$

Where e is the colour noise image, which has three components e^L,$e^{R/B}$ and $e^{G/M}$, and each has a spectral density presented in [9]. The noise realization of the chrominance is independent, which makes it easier to remove the noise.

The filter used is a Wiener filter, whose coefficients are given by the vector x solution of the linear system of size 81×81, the formulation of this equation is given in [9]. This filter estimates the denoised chrominance directly.

This approach, proposed in its rigourous form by Dupois was extended to the noisy case. Thus, the Demosaicing method by frequency selection is divided into four steps which are presented in [57] and consist: estimate the G/M chrominance and R/B chrominance by modulation and convolution with a low pass filter presented by $h_{G/M}$ and $h_{R/B}$, respectively; the subtraction of the denoised chrominance images from v, and re-modulation; and the denoise process of the image d^L.

Demosaicing by frequency selection solves a variational problem. This way the variational interpretation of Demosaicing by frequency selection is given in **equation 5.28**.

$$\mathbf{d} = \underset{d}{\operatorname{argmin}} \ \mu\|\nabla d^L\|_{l_2}^2 + \|\nabla d^{G/M}\|_{l_2}^2 + \|\nabla d^{R/B}\|_{l_2}^2 \quad \text{subject to } d^{X[\mathbf{k}]} = v[\mathbf{k}], \ \forall \mathbf{k} \in \mathbb{Z}^2 \tag{5.28}$$

Where a discrete gradient vector is introduced using finite difference as given in **equation 5.29**.

$$\nabla u[\mathbf{k}] = \Big[u[\mathbf{k}] - u[k_1 - 1, k_2] \ , \ u[\mathbf{k}] - u[k_1, k_2 - 1]\Big] \tag{5.29}$$

This finite difference is equal to zero when it involves a pixel outside the image domain. The parameter μ given in the **equation 5.29** controls the balance between the smoothness of the luminance and the chrominance in the resulting image. If the value of μ is zero the demosaiced image d will be a monochrome image, since all the frequency energy of v is assigned to d^L, thus the image resulting will be a grayscale image plus a constant colour. If the value μ is one, the Demosaicing process will reconstruct the R,G,B channels independently and the global solution is obtained by the interpolation of each channel, this way, it will not take into account the cross-correlations between the R,G,B channels. The value μ should be between zero and one, and there is no mathematical formula to choose μ, thus the best value is chosen empirically by trial and error.

The problem of performing Demosaicing by Frequency Selection is that when the value of μ is reduced, the noise of the image v is almost entirely assigned to the luminance channel d^L, which will result in image sharp colour transitions, over-smoothed edges. Thus, a non-quadratic regularization named Total Variation, was developed which as it was stated in the Inpainting method, keeps sharp edges, [54] [57].

Demosaicing using Total Variation Minimization

With regard to the **equation 5.28**, it is noticeable that no colour axis is privileged and the problem formulation is independent of the chrominance basis chosen, thus achieving the equality given in **equation 5.30**, [58].

$$\|\nabla d^{G/M}\|_{l_2}^2 + \|\nabla d^{R/B}\|_{l_2}^2 = \|\nabla d^C\|_{l_2}^2 \tag{5.30}$$

The other method created by Laurent Condat is a Total variation formulation of the colour image, [58], which is given in the **equation 5.31**.

$$\|d\|_{TV} = \mu\|\nabla d^L\|_{l_1} \ + \ \|\nabla d^C\|_{l_1} \tag{5.31}$$

The **equation 5.31** can be rewritten by the **equation 5.32**.

$$\underset{d}{\operatorname{argmin}} \ \|d\|_{TV} := \mu\|\sqrt{(\nabla_x d^L)^2 + (\nabla_y d^L)^2}\|_{l_1} + \sqrt{(\nabla_x d^{G/M})^2 + (\nabla_y d^{G/M})^2 + (\nabla_x d^{R/B})^2 + (\nabla_y d^{R/B})^2}\|_{l_1} \tag{5.32}$$

The following equation is subject to $d^{X[\mathbf{k}]}[\mathbf{k}] = v[\mathbf{k}]$, $\forall\, \mathbf{k} \in \mathbb{Z}^2$. Thus, the main difference between the total variation approach and the algorithm describe in the previous section being the consistency with the data, so that the noise is not removed but transferred to the luminance channel d^L. As stated, total variation method is a non-quadratic, convex and not differentiable function, which makes impossible the application of the conventional smooth optimization techniques.

Since the procedure described in the previous section cannot be applied due to the fact that the solution is non-quadratic, the method used by Laurent Condat to obtain the colour image is described in [58]. The second step after applying the minimization given in the **equation 5.32** is to denoise d^L.

5.2 Experimental Procedure

As mentioned, the main goal of this project is to perform K-edge imaging on moving objects at full spatial resolution using composite pixels. Therefore, this research project studied methods that estimate data from partial measurements in order to evaluate which one would provide better spatial resolution in spectral CT images. The other subject that will be studied is patterning composite pixels. These subjects that will be studied were achieved by performing and using metrics that allowed the evaluation of the image spatial resolution. The evaluation metrics used are SNR, PSNR and MSSIM, which SNR is the abbreviation of signal-noise ratio; PSNR is peak-signal-to-noise ratio; and MSSIM is the mean Structural Similarity Index. Therefore, the two first parameters evaluate specially the effect of the noise in the reconstruction, and the last parameters takes more in consideration the amount of contrast and detailed that the reconstructed image have. The mathematical formulation of this methods is presented in the **Appendix E**.

Therefore, several points will be analysed in order to evaluate the subjects mentioned. Although the composite pixels used at CPPM only have three different thresholds, it is known that setting more than three energy thresholds will bring advantages in the sense that more materials will be visualized. Therefore, the possibility of increasing the number of thresholds have to be tested and for each possibility, the recovery methods of the missing data will be tested. Since with the increasing of energy thresholds, partial measurements will decrease, the estimation of those measurements will be even more difficult and the image quality, consequently, will decrease. Therefore, an analysis have to be made, in order to see if even with image quality loss the increase is worth it.

The other topic addressed is the pattern of composite pixels. This research project will explore another pattern besides the regular, the random pattern. Hence, the two patterns as well as their relation with the reconstruction method for each image will be tested, in order to verify which method and pattern is the best. The research project can be divided into three

steps:

1. How many energy ranges should be used
2. Which pattern the composite pixels should follow
3. Which reconstruction method should be use in order to recover the missing data from partial measurements

The purpose of the first part of this work was to analyse the number of energy ranges that showed better results. Thus, using the simulated phantom image and several masks, where the difference between them was the amount of information available. The masks used for this purpose had a random pattern and missing pixels. This way, three types of masks were used: 1/3, 1/4 and 1/6 of information available. The processing consists in multiplying the image by the mask, and then applying the reconstruction methods. For each resulting image, two evaluation parameters were used: PSNR and MSSIM.

The Demosaicing method just uses three channels, so to evaluate the best pattern and reconstruction method, the masks applied to the images have three channels. The masks, as stated, are the simulated composite pixels, and each channel is equivalent to an energy range. Phantom, MOBY and real data images were acquired in three different energy ranges.

Before performing the mask and the noise, the images were normalized. As stated, MSSIM is an evaluation parameter, whose code used required that the images values had a range between 0 and 255. Thus, the formula applied to acquired images in this range is given in **equation 5.33**.

$$I_{ref} = \left(\frac{I_{original}}{max(I_{original})} \right) \times 255 \tag{5.33}$$

Where $I_{original}$ is the original image which contains three images, this way, the maximum of the original image is the maximum of the three images. The maximum value is from one of the images, which depends on the type of image used. After the normalization and multiplication by 255, each image will be divided into three images, and the mask will be divided in three sub-masks as demonstrated in **Figure 4.2**, where two of them have 1/3 of available information, and the other has 1/2 of available information. The pixels which contain information have value 1, and the pixels with no information have the value 0.

Since the goal of this work was to recover missing data from partial measurements acquired by the detector, it was necessary to simulate noise. Real data images were acquired from the XPAD3 detector so the addition of noise was not needed. For the MOBY and Phantom images it was needed to add noise. In order to control the quality of the resulting image and the noise, the strategy used was to define a resulting SNR ($inSNR$). The noise prediction of the images that are acquired by spectral CT scan is not possible, however several attempts can be made to predict the noise. This way, an input of SNR was introduced to control the level of noise in the image. The formula is given in equation and it is based on the equation to calculate the SNR, **equation 5.34**.

$$\sigma_N = 10^{(-\frac{inSNR}{20})} \times std(image_N), \quad N = 1:3 \tag{5.34}$$

Where σ_N is the level of noise that will be added to the image and $inSNR$ is the input chosen that will vary between 20 and 40 dB, with a step-size of 5 dB. In the cases where the methods and patterns without noise will be evaluated, the $inSNR$ will be infinite. Since each image has a different range of values, as shown before, each image will have a value of σ, thus, the N corresponds to the band/channel. Taking the example of Simulated phantom image, σ will be calculated for each image of **Figure B.2**.

Then, each energy range used in the Phantom, the MOBY and real data image was multiplied by one sub-mask. In the simulated phantom image, each colour channel was multiplied by one sub-mask. This resulted in three images which contain the original number in the corresponding pixel with number 1 of the sub-mask. The operation described is demonstrated in **Appendix C**.

To each images multiplied by the sub-mask was added noise with the corresponding σ. Thus, **equation 5.35** shows the operation made to acquire the image that will be submitted to the reconstruction methods. To simulate the noise, a random function was used which generates a normally distributed random numbers.

$$\text{final image}_N = image_N \times submask_N + noise \times \sigma_N \quad N = 1:3 \tag{5.35}$$

The next procedure is to apply the reconstruction methods to the resulting images. Inpainting and interpolation will be performed on the separated images. The Inpainting method, as stated in the previous section, was applied in two different ways. The first Inpainting method implemented was based on [42] and it was seen as a regularization problem. The issue with this technique was the computing time, as it was demonstrated in the description of the method, for each image it was necessary to find the best parameter. Thus, the need of a very big number of iterations and the necessity to make several attempts to determine the parameter that better fits the image. Therefore, the toolbox referred in the previous section was used, which explanation is presented in **Appendix E**. In the Demosaicing method, before applying the method, the three images will be united since this method is applied in coloured images. Since the image has size of (n, m) where n is width and m is the length, the resulting image will be three-dimensional after coupling the three images, thus the final image that will be submitted to the Demosaicing method will have the size of $(n, m, 3)$.

The following step is to perform image denoising, thus, the application of BM3D method [59]. The denoising was made in the same mode in all images, which the image to be denoised and the level of noise was placed as inputs, σ. The real data images are the most important images to test since they were acquired from the spectral CT at the CPPM, therefore, the denoising process was also analysed. This analysis was made using the Bayer mask as composite pixel simulation.

The image that was introduced as input in the BM3D code had to have three dimensions $(n, m, 3)$. In the Inpainting and Interpolation methods, the three resulting images were coupled in one image, in the Demosaicing method, the output has already three dimensions. In all the methods, the σ used was estimated based on the three $sigma_N$ values of the three images, thus the formula is given in **equation 5.36**.

$$\sigma = \sqrt{\sigma_1^2 + \sigma_2^2 + \sigma_3^2} \tag{5.36}$$

Then, the evaluation methods between the original image and the resulting denoising image are applied. The evaluation parameters used are the PSNR and MSSIM. This way, the evaluation parameters that were performed between the original image and denoised image will be analysed.

The evaluation parameters of the real data images consist in the average of those values in the 360 projections. The next step is to perform the 3D reconstruction and afterwards, it was once again applied the evaluation parameters between the original image and the image resulted from the 3D reconstruction software.

The procedure described was made in the same way for both patterns, random and regular. The scheme represented in **Figure 5.6** is a summary of the procedure made to the MOBY and phantom. For the real data images, since they were acquired from the XPAD3 detector, they already have noise, which rendering step 3 unnecessary for those images.

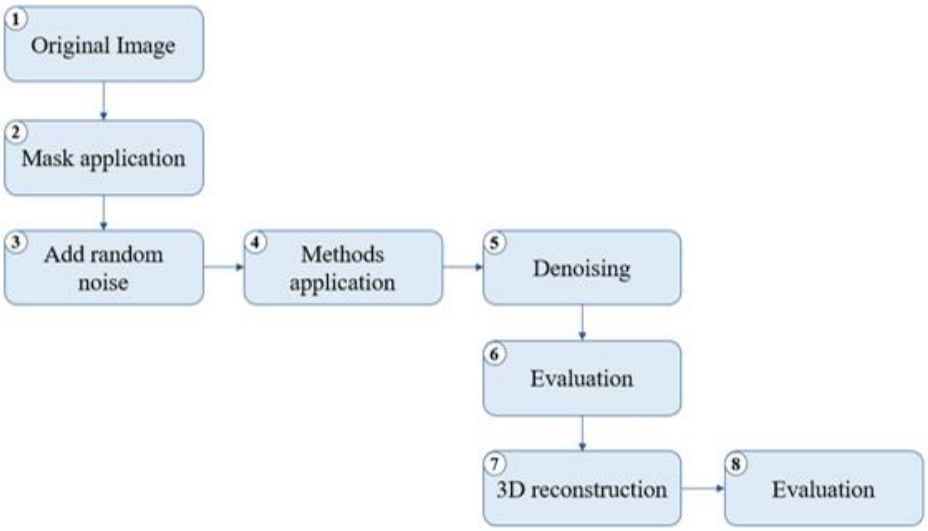

Figure 5.6: Scheme of the main experimental procedure

Chapter 6

Results and Discussion

The main goal of this research project is to achieve K-edge imaging in moving objects at full spatial resolution, therefore, the project was divided into three sections. In this chapter, the results achieved will be disclosed as well as the corresponding analysis.

With regard to the results made in order to achieve a better spatial resolution, this chapter was divided into five sections. The first one will consist in the analysis of the performance of the reconstruction methods to acquire the missing data according to different percentages of partial measurements. In the second and third section of this chapter, the reconstruction methods will be analysed in two different composite pixels patterns with three energy ranges. In the fourth section, the results between the two patterns of composite pixels will be studied, in order to achieve a comparison leading to the identification of which pattern shows a better spatial resolution. Finally, in the fifth section, an analysis of the K-edge imaging using composite pixels will be done, thus the relation between the attenuation coefficients and the colours of the images using composite pixels will be made. For each section, the performance of the reconstruction methods will be evaluated in presence and absence of noise. The input SNR used to study the methods in noisy images is 25 dB.

The following results were achieved by performing the procedures mentioned in Chapter 5. All the data that will be presented in this chapter is acquired and was taken from the Matlab software.

6.1 Missing data Analysis

One of the main advantages of the hybrid pixel detectors is that they allow the setting of an energy threshold in the pixels. At the CPPM, the hybrid pixels detectors used have three energy thresholds. As stated in Chapter 2, one of the main interests of Spectral CT is the possibility of using several energy thresholds that, when combined with the material physical properties, allow the visualization of several elements. Having this in mind, this section will test how the reconstruction methods perform with the increase of energy ranges. Therefore, three situations will be studied, composite pixel using 3, 4 and 6 energy ranges.

The methods used are Linear Interpolation, Inpainting using Total Variation Minimization and Inpainting using Sobolev Minimization. Demosaicing methods, as explained, consist in the reconstruction of a full color image, therefore they are applied to images with three color

components. Taking this method in the spectral CT images context, to each color component corresponds an energy range, thus making it impossible for these methods to be used to test more than three energy ranges.

Since the goal was to evaluate the performance of composite pixels with several energies ranges, the image used was grayscale. The image used was the simulated Phantom image, which was normalized and multiplied by 255. As stated, the simulated phantom was acquired in three energy bands but, for the analysis of the missing data, just one image/energy range was considered though. Therefore, the image that was submitted to the reconstruction methods is presented in **Figure B.2a** .

The evaluation parameters that will be used are the PNSR and MSSIM. The PSNR is computed in the same way as CPSNR, whose mathematical formulation is given in **equation D.5** and since the image is grayscale, the value of k is 1.

The analysis of the reconstruction performance depending on the number of composite pixels was made in images with noise. The input SNR used was 25 dB.

The resulting evaluation values of the reconstruction methods are presented in **Table 6.1**.

Table 6.1: Evaluation parameters with presence of noise

	PNSR			MSSIM		
	1/3	1/4	1/6	1/3	1/4	1/6
Linear Interpolation method	31.37	30.57	28.979	0.785	0.805	0.826
Total Variation method	33.92	33.49	32.72	0.839	0.869	0.900
Sobolev method	33.92	33.42	32.02	0.830	0.854	0.878

The difference between the methods performance in noisy and noiseless images is significant regarding the PSNR values. MSSIM, as mentioned in the previous Chapter, consists in the structure similarity analysis and evaluates the contrast and the spatial dependency, while PSNR consists in the signal-noise ratio. The increase of missing information decreases the PSNR values. However, the MSSIM values increase with the increase of channels.

In order to understand the increase of MSSIM values, **Figure 6.1** presents the images acquired by the best reconstruction method at the three possible number of energy channels: 3, 4 and 6. The range of values of the resulting images had negative values because of the random noise added. The display was made with a value range between -10 and 40 in order to visualize the difference between the three images.

Comparing the three images presented in **Figure 6.1**, the contrast presented in **Figure 6.1c** comparing to the original image is lower than on the other images; the structures are not well defined. Since MSSIM metric also evaluates the contrast, the decrease of contrast led to an increase of MSSIM. PSNR is the ration between the maximum value of the image and the power of distorting noise, therefore the maximum value of the image decreases with the increase of channels.

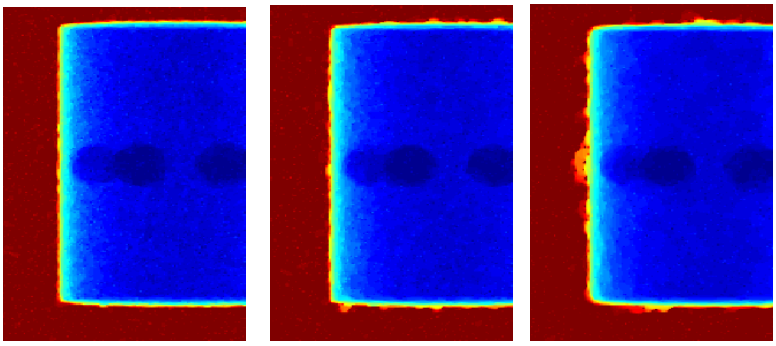

(a) Image acquired with 1/3 of available information

(b) Image acquired with 1/4 of available information

(c) Image acquired with 1/6 of available information

Figure 6.1: Images resulted from the Inpainting using Total Variation Minimization. The range of the image values was limited by -10 and 40

6.2 Mask with Regular Pattern

As stated in the procedure, the second part of this project consists in the evaluation of two possible composite pixel patterns. In this project the most important thing is not the colour of the resulting image but the amount of detail that is preserved after the reconstruction. Although, the colours presented in the image acquired by composite pixels had to be consistent, this way the colour in this scenario is important to identify the solutions that constitute the structures. The Demosaicing algorithm use concepts of chrominance and luminance, which luminance consists in the green channels of the masks and chrominance is the colour ratio. Therefore, an observation that will be discuss is the change of luminance that is, the red pixels will be used as luminance channels instead of taking the green pixels. This test is made in order to test if the change of energy channels will change the reconstruction performance.

This section is divided into four parts being the first one related to the performance of the channels modification and the last three sections consisting in the evaluation of the reconstruction methods in three different images. The methods that will be tested are: Linear Interpolation, Inpainting using Total Variation minimization, Inpainting using Sobolev minimization and Demosaicing by Frequency Selection and Demosaicing using TV Minimization. The images used are the MOBY image, simulated Phantom image and the real data.

All the reconstruction images were submitted to a 3D reconstruction in order to visualize if in 3D space they will have good spatial resolution. The 3D reconstruction is based on FBP reconstruction whose algorithm was made at CPPM by Mathieu Dupont.

6.2.1 Simulated phantom image

In this section, the simulated phantom images acquired by the five reconstruction methods will be presented followed by a detailed explanation in order to verify the main differences between the methods so to determine which one of them gives better spatial resolution. The results will be divided into two parts, the reconstruction methods evaluation when noise is added to the images, and the reconstruction methods evaluation in the situation where the images are

noiseless.

As stated in the experimental procedure and the materials of this research project, the simulated phantom images consist in three images acquired by three different energy ranges. Therefore, in the Inpainting and Linear Interpolation methods, the images will be treat individually, whereas for Demosaicing methods the images will be merged in one, representing the color image concept. Each color component that the Demosaicing method treats will be presented as an energy range.

The 3D reconstruction images will be presented as a third part of this section.

Noiseless images

The evaluation performance of the reconstruction methods is presented in **Table 6.2**.

Table 6.2: Phantom image evaluation parameters acquired with composite pixels with regular pattern and in the noiseless situation

	PNSR	MSSIM
Linear Interpolation method	41.12	0.994
Total Variation method	36.43	0.991
Sobolev method	39.04	0.996
Demosaicing by FS	41.77	0.989
Demosaicing by TV	47.42	0.999

The reconstruction method that presents better results is the Demosaicing using Total Variation Minimization. Linear Interpolation images present very good image quality compared to Inpainting using Total Variation Minimization ones. The Linear Interpolation method presents good results due to the small amount of details. **Table 6.2** shows that Demosaicing TV presents the best evaluation parameters, the followed by Demosaicing using Frequency Selection.

The images acquired by the reconstruction methods were analysed and the differences between them are not easily visible. Thus, in order to visualize which features each method manage to recover and the main differences between the reconstruction methods, the difference between the original image and the reconstructed image was displayed, $(I_{ref} - I)$. The images displayed in **Figure 6.2** are associated to the methods that showed better performance, which are Demosaicing TV, Demosaicing FS and Linear Interpolation.

The coloured pixels presented in **Figure 6.2** represent the pixels that were not recovered. The portions that were not recovered are specially found in the edges as the contour of the circles and the cylinder.

With regard to the Demosaicing methods, the range of pixel colours is more diverse in comparison to the other methods. The image acquired by the difference between the original image and the image acquired by the Demosaicing TV method is presented in **Figure 6.2a**, where it can be observed that the pixels which were not so well recovered have a red and purple color. In the colour bar presented in **Figure B.2**, it is seen that the pixels with higher values are red and the pixels with lower values have blue colour. Therefore, Demosaicing TV didn't recover the pixels with higher intensity values.

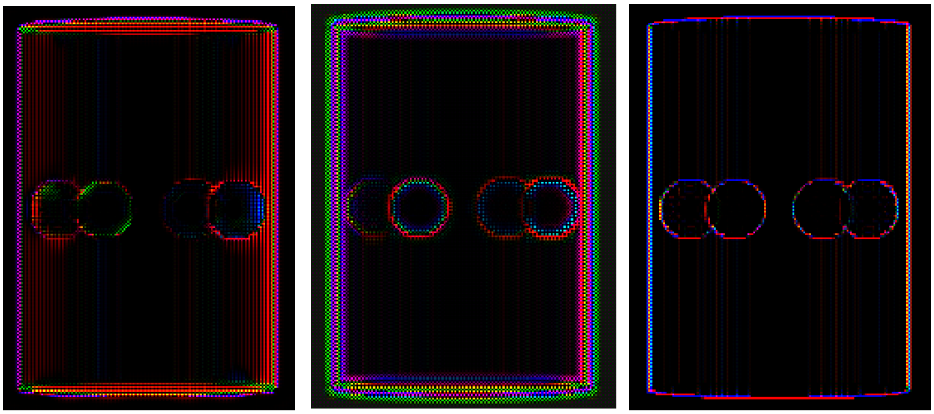

(a) Original Phantom image minus Demosaicing TV image

(b) Original Phantom image minus Demosaicing FS image

(c) Original Phantom image minus Linear Interpolation image

Figure 6.2: Images acquired by the difference between the original Simulated phantom image and the images resulted from the reconstruction methods

Figure 6.2b presents the difference between the original image and the image acquired with the Demosaicing FS method. This method was not able to recover the edges, however the pixel colours are not continuous as in the images acquired by Linear Interpolation where contouring lines are visible and the coloured pixels are sharper, as demonstrated in **Figure 6.2c**. This is a possible reason why the PSNR and MSSIM value are higher in the Demosaicing FS than in the Linear Interpolation method, as demonstrated in **Table 6.2**.

Noisy images

Table 6.3 presents the evaluation parameters values of the reconstruction methods when noise was added.

According with the evaluation performance, whose values are shown in **Table 6.3**, Demosaicing using Total Variation Minimization is the method that showed better performance, independently of the level of noise added. Demosaicing FS is the method that follows with better performance. Inpainting Sobolev is the method that presents the worst performance when high level of noise is added; however, with the decrease of noise, Inpainting TV is the method with the lowest PSNR values.

The method that shows better MSSIM values is the Demosaicing TV. The MSSIM values of the images acquired with the Inpainting TV and the Inpainting Sobolev method follow the same behaviour as the PSNR values. Inpainting TV shows better performance than Inpainting Sobolev in images with a higher level of noise. The Linear Interpolation method shows the lowest performance compared to the other methods except with low level of noise, as demonstrated in **Table 6.3**.However this method shows good results in the PSNR values, which is justified by the fact that the noise ratio is less in the Linear Interpolation image, but the structures were not well recovered.

Table 6.3: Phantom image evaluation parameters acquired with composite pixels with regular pattern and in the noisy situation

	PNSR					MSSIM				
	10	20	25	30	40	10	20	25	30	40
L.Int.	22.4	31.9	35.8	38.7	40.8	0.277	0.725	0.878	0.953	0.989
In. TV	21.2	30.0	32.6	33.6	35.2	0.525	0.883	0.947	0.974	0.990
In. Sobo	20.5	29.9	33.9	36.7	38.7	0.507	0.877	0.947	0.977	0.990
Dem. FS	27.6	35.2	38.4	40.3	41.6	0.579	0.904	0.956	0.977	0.988
Dem. TV	28.8	37.3	41.1	43.7	46.4	0.668	0.925	0.973	0.989	0.998

Since the aim of this project is to study the spatial resolution, it is important that is the structures are well defined. At an input SNR of 25 dB, Linear Interpolation showed better PSNR values than Inpainting Sobolev, however the difference was no more than 2 dB. Inpainting Sobolev will be presented instead of Inpainting TV due to the fact that its PSNR is higher, and the difference between the MSSIM acquired is low. Demosaicing FS will not be presented because of the fact that it is not visibly evident the differences between this method and Demosaicing TV. Therefore, the images that will be displayed in the **Figure 6.3** will be the images acquired by the Demosaicing TV method and Inpainting Sobolev method.

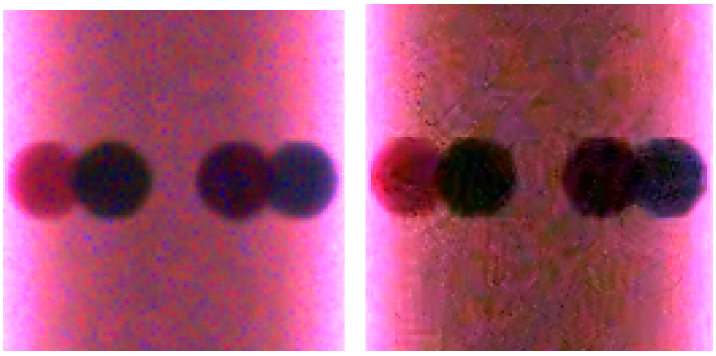

(a) Inpainting Sobolev resulted image

(b) Demosaicing TV resulted image

Figure 6.3: Simulated phantom Images reconstructed by reconstruction methods

The difference of the MSSIM value between the images presented in **Figure 6.3a** and **Figure 6.3b** proved that the image acquired by Inpainting Sobolev is more smoother than the other, which decreases slightly the MSSIM value. The image acquired by Demosaicing TV has the highest MSSIM due to the fact that the structures were well recovered as demonstrated in **Figure 6.3b**. In **Figure 6.3a**, some sharp blue coloured pixels can be seen which decreases the quality of the image. In the Demosaicing method, the colour is not well recovered, but the colours are spread and punctual coloured pixels are not identified, which results in a better image quality.

3D reconstructed images

In this section, the images that resulted from the 3D reconstruction program will be presented. Since the reconstruction methods were applied to images with noise and to noiseless

ones, the images resulting from the 3D reconstruction will be connected to these two situations. In the noiseless case, as demonstrated in **Table 6.2**, the two reconstruction methods that presented higher performance are the Demosaicing methods and the Linear Interpolation method. The 3D reconstruction images are an important observation in order to analyse if the quality of the images submitted is coherent with the quality of the 2D reconstructed images. **Figure 6.4** presents the 3D reconstructed images acquired by the Linear Interpolation method and Demosaicing TV method. The image acquired by Demosaicing FS method is very similar to the one acquired by the Demosaicing TV method which makes the illustration of the images acquired by this method irrelevant.

In the noiseless case, all the details are well recovered in **Figure 6.4a** and **Figure 6.4b**; however the image acquired by the Linear Interpolation method seems to be of better quality than the other methods, which is not justified by the 2D images acquired. The 3D image acquired by the Linear Interpolation method has better quality than the images acquired by the other two methods, whose PSNR value is 36.549 dB. The structures were well recovered by the Linear interpolation method due to the fact that the MSSIM value is above 0.9. The MSSIM values of the other two methods present reasonable quality since these values are above 0.5. The Demosaicing methods have lower PSNR due to the presence of traces that connect the balls, which is very similar to the beam hardening effect. One possible justification for these traces is the correlation between pixels from several bands used by the Demosaicing methods.

In what concerns the situation of images with noise, the methods that present better performance are the Demosaicing TV method and the Demosaicing FS method. Since the image acquired by the Demosaicing FS method is very similar to the reconstructed image acquired by Demosaicing TV, instead of displaying the image acquired by the Demosaicing FS method, the image acquired by Inpainting Sobolev will be presented. **Figure 6.4** presents the 3D reconstructed images.

Figure 6.4d presents better quality due to the higher definition of the components. In both images, green coloured pixels are identified which consist in the noise present in the images. These pixels are green due to the fact that the energy band that has more information is the second energy range, which in the RGB system represents the green channel. Therefore, the noise is higher in this channel.

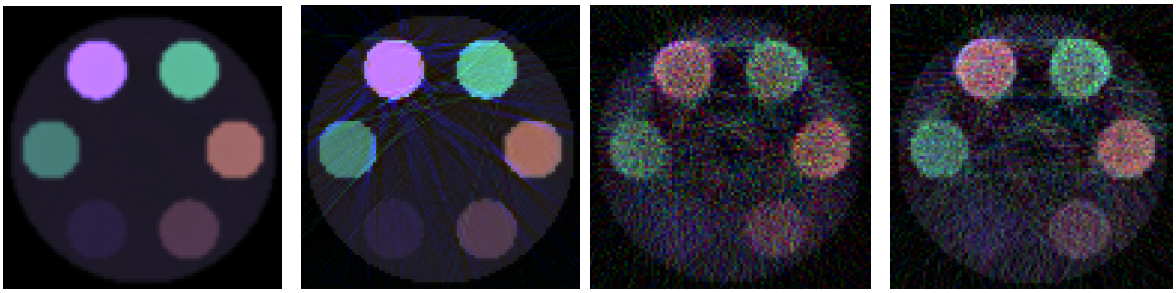

(a) Linear Interpolation image in the noiseless case

(b) Demosaicing TV image in the noiseless case

(c) Inpainting Sobolev image in the noisy case

(d) Demosaicing TV image in the noisy case

Figure 6.4: 3D reconstruction of the simulated phantom images acquired by the reconstruction methods using a regular pattern.

The PSNR values of the 3D reconstructed image presented in **Figure 6.4c** and in **Figure**

6.4d are 19.018 dB and 20.377 dB, respectively. The small difference between the two methods is due to the amount of sharp green pixels that connect the balls, as demonstrated in **Figure 6.4c**. The MSSIM values of the 3D reconstructed images are very low, being below 0.5. The MSSIM value of the image acquired by Inpainting Sobolev and Demosaicing TV is 0.1701 and 0.2002, respectively. These values are very low and justify the poor structure recovery presented in **Figure 6.4**.

6.2.2 MOBY phantom image

MOBY phantom image was used to verify if the reconstruction methods were able to recover enough information in order to see the mouse structures. Therefore, the reconstruction methods were applied to the 2D images, and then, a 3D reconstruction was made. First the images with no presence of noise will be studied and in the second part the images to which some noise was added will be analysed.

Noiseless images

The reconstruction methods performance is presented in **Table 6.4**. According to the MSSIM and PSNR values, Demosaicing using Total Variation Minimization presents the best results. As stated, in some cases the differences between the images acquired using the different methods are not easily detected.

Table 6.4: MOBY image evaluation parameters acquired with composite pixels with regular pattern and in the noiseless situation

	PNSR	MSSIM
Linear Interpolation method	45.53	0.995
Total Variation method	39.76	0.995
Sobolev method	45.49	0.9977
Demosaicing by FS	46.72	0.992
Demosaicing by TV	53.66	0.999

Figure 6.5 presents the images acquired by this difference whose reconstructed images are acquired by Demosaicing TV and Demosaicing FS. Linear interpolation will not be displayed due to the small differences between the PSNR and MSSIM values of the images acquired by the Linear Interpolation method and the Demosaicing FS.

Figure 6.5 shows the images acquired by performing the difference between the original image and the reconstructed image. The edges of **Figure 6.5a** are coloured and they are in their majority red and blue, which means that Demosaicing TV didn't recovered well the first band. Since this method uses the chrominance concept, these colours are observed due to the fact that the first band is the color ratio of red and blue.

Since the presence of coloured represent the not recovered pixels, the evaluation parameters of the Demosaicing FS showed worst results than Demosaicing TV as demontrated in **Figure 6.5b**. The structures were better recovered by the Demosaicing TV method than by

the Demosaicing FS method, which can be verified by the amount of coloured pixels in the contours presented in **Figure 6.5b**

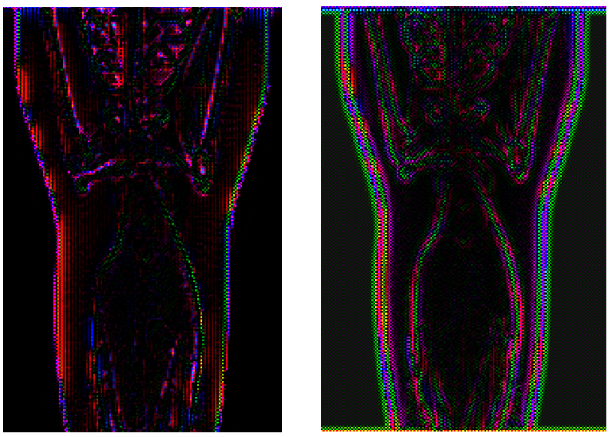

(a) Original image minus Demosaicing TV

(b) Original image minus Demosaicing FS

Figure 6.5: Images acquired by the difference between the original image and the reconstructed images

Noisy images

Table 6.5 present the PSNR and MSSIM parameters of the five reconstruction methods concerning to the MOBY image with noise.

Demosaicing TV is the method that presents better PSNR values independently of the input SNR, as demonstrated in **Table 6.5**. Linear Interpolation presents low performance in images with high level of noise, however, with the decrease of noise, the images acquired with this method have better PSNR.

The MSSIM values of the images acquired by the Demosaicing TV method present better results. Linear Interpolation method as observed in the PSNR values, present low MSSIM values in the image with high level of noise, but with the decrease of noise, the images acquired by this reconstruction start to increase, reaching PSNR values close from the other methods.

Table 6.5: MOBY image evaluation parameters acquired with composite pixels with regular pattern and in the noisy situation

	PNSR					MSSIM				
	10	20	25	30	40	10	20	25	30	40
L.Int.	22.49	32.29	36.81	40.65	44.67	0.277	0.732	0.884	0.955	0.991
In. TV	24.70	33.63	36.77	38.56	39.53	0.356	0.813	0.925	0.971	0.992
In. Sobo	24.09	33.65	37.69	40.63	42.94	0.342	0.798	0.919	0.969	0.994
Dem. FS	28.56	36.78	40.48	43.51	46.14	0.589	0.914	0.962	0.981	0.991
Dem. TV	29.55	38.27	42.42	46.13	50.98	0.686	0.931	0.971	0.989	0.997

The methods trough which the images with better quality were acquired are the Demosaic-

ing TV and the Inpainting Sobolev methods. Therefore, the images acquired by these methods are displayed in **Figure 6.6**. A comparison between the two Demosaicing method was made, and it was verified that the images were very similar and no evident differences were observed. Therefore, Demosaicing using Frequency Selection will no be displayed. At this level of noise, the image acquired by Inpainting TV presented a better MSSIM value than the image acquired by Inpainting Sobolev, however this difference is not significant. Therefore, the image acquired by Inpainting Sobolev will be displayed instead of the Total variation image due to the PSNR value. Comparing the evaluation parameters of these three methods with the images presented in **Figure 6.6**, the image acquired by Demosaicing TV presents better image quality, which is proven by the MSSIM and PSNR values. Inpainting Sobolev present an image with lower PSNR and MSSIM due to the fact that some data was not well recovered, as demonstrated in **Figure 6.6a** where some green and blue pixels are visible. Regarding the Demosaicing methods, **Figure 6.6b** presents well defined pixels on the edges of the mouse, which means that the number of iteration used was not enough to fully recover the missing information. Therefore, the PSNR and MSSIM values of the image acquired by this method are lower than the one acquired by the Demosaicing TV.

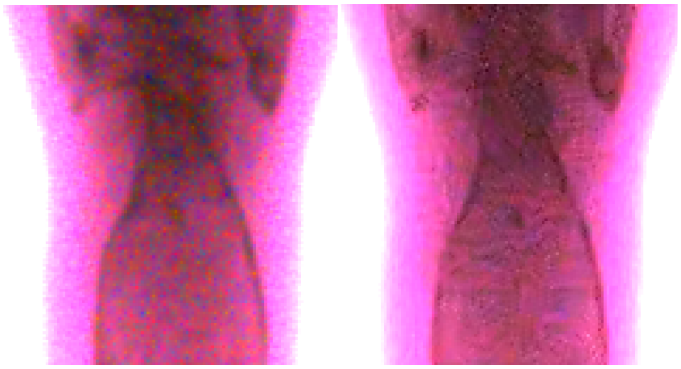

(a) Inpainting Sobolev resulted image

(b) Demosaicing TV resulted image

Figure 6.6: MOBY images acquired by the reconstruction methods

3D reconstructed images

After the analysis of the 3D reconstructed images and the corresponding evaluation metrics, it was observed that the image acquired by Linear Interpolation presented better quality than the other methods whose PSNR is equal to 34.865 dB. The PSNR values of the 3D images acquired by Demosaicing TV and Demosaicing FS are 34.730 dB and 34.085 dB, respectively. According to the PSNR values of the 3D reconstructed images, all the methods have a good and similar performance; however the evaluation of the 2D images is not identical. Therefore, in the noiseless case, the images that will be presented in **Figure 6.7** are the images acquired by Demosaicing TV and Linear Interpolation.

The MSSIM values regarding the images presented in **Figure 6.7a** and **Figure 6.7b** are 0.9682 and 0.8852, respectively. The MSSIM value of the image acquired by the Linear Interpolation method is higher than the other method due to the fact that the contrast of this image is closer to the contrast of the 3D reconstructed original image. Comparing **Figure 6.7a**

and **Figure 6.7b** one can verify that the image acquired by Demosaicing TV has a brighter colour, which is one aspect that decreases the PSNR value. Despite the PSNR value being better in the image acquired by the Linear Interpolation method, it appears that the image is too smooth and some structures are not as sharp as in the image acquired by the Demosaicing TV method.

With regard to the situation where noise was added to the images, the methods that a presented better performance are the Demosaicing TV, the Demosaicing FS and the Inpainting Sobolev methods. Therefore, the 3D reconstructed images acquired by these three methods were analysed and it was verified that the PSNR values of these methods were 28.159 dB, 28.798 dB and 24.860 dB, respectively. The difference between the PSNR values of the 3D reconstructed images acquired by the Demosaicing methods is very low, which doesn't happen with the PSNR values of the 2D images acquired by these two methods. In a pre-analysis it was seen that the 3D reconstructed images acquired by Demosaicing methods didn't show relevant differences which is confirmed by the PSNR values mentioned previously. Therefore, in images with noise, the 3D reconstructed images that will be presented in **Figure 6.7** are the images acquired by the Demosaicing FS method and the Inpainting Sobolev method.

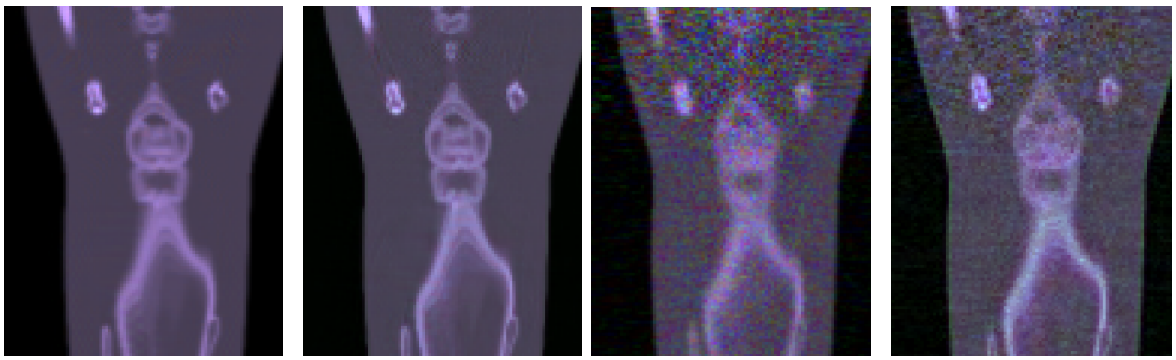

(a) Linear Interpolation image in noiseless case

(b) Demosaicing TV image in noiseless case

(c) Inpainting Sobolev image in noisy case

(d) Demosaicing FS image in noisy case

Figure 6.7: 3D reconstruction of the MOBY images acquired by the reconstruction methods using a regular pattern.

Figure 6.7c presents more green pixels than **Figure 6.7d** which corroborates the PSNR values presented above. When it comes to the MSSIM values, the image acquired by Inpainting Sobolev presents a MSSIM value equal to 0.4907. This value is much lower comparing to the MSSIM of the image acquired by Demosaicing FS (0.6267). This difference is mainly caused by the amount of green pixels in the top of the image that makes it almost impossible to observe the structures in that section.

6.2.3 Real Data

In the real data, the images are acquired by the XPAD3 detector, which means that they already contain noise. The reconstruction methods performance in these images will be an example of how the reconstruction methods perform on real data acquired by the detectors used at CPPM. And therefore, an evaluation will be made, to verify if the resulting images show

better spatial resolution than the original images. Thus, the division of this section is made into three subsections, where the two first ones will demonstrate the evaluation performance of each method for cylinder images. And in the third section, the 3D image acquisitions will be presented. For each reconstruction method, the same denoising procedure was performed.

Cylinder images

As stated, the real data images already have noise, thus, this section will present the 2D images and 3D images acquired by the best reconstruction methods. Besides the analysis of the images, the PSNR and MSSIM values will also be shown. **Table 6.6** present the parameters that express the image quality of the images acquired by the reconstruction methods.

Inpainting using Total Variation Minimization is the method that presents better performance. The PSNR values of the images acquired by Inpainting Sobolev and Demosaicing TV are very similar, as presented in **Table 6.6**. However, the MSSIM value of the images that resulted from the Demosaicing TV method is lower than the MSSIM value of the image acquired by the Linear interpolation method. This means that the level of noise in the images acquired by Linear Interpolation method is higher when compared to the other methods; however the structures were well recovered.

Table 6.6: Evaluation parameters that evaluate the quality of the Cylinder images acquired by the reconstruction methods. The mask used to recreate the composite pixel concept has a regular pattern

	PNSR	MSSIM
Linear Interpolation method	40.44	0.975
Total Variation method	42.73	0.981
Sobolev method	41.83	0.979
Demosaicing by FS	40.46	0.967
Demosaicing by TV	41.77	0.974

The images presented are the ones acquired with the methods that showed better performance in **Figure 6.8** are: Inpainting TV and Inpainting Sobolev. The image acquired by Demosaicing TV will not be displayed due to the fact that its PSNR value is very close to the Inpainting Sobolev one, thus not showing any considerable differences.

The main difference between **Figure 6.8a** and **Figure 6.8b** is the presence of sharp coloured pixels which implies that those pixels were not well recovered. **Figure 6.8b** presents several blue coloured pixels, which means that the Inpainting Sobolev method didn't recovered well the third energy range. In both images the structures are well recovered and the differences between the structures recovery is not evident which is justified by the close MSSIM values, as demonstrated in **Table 6.6**.

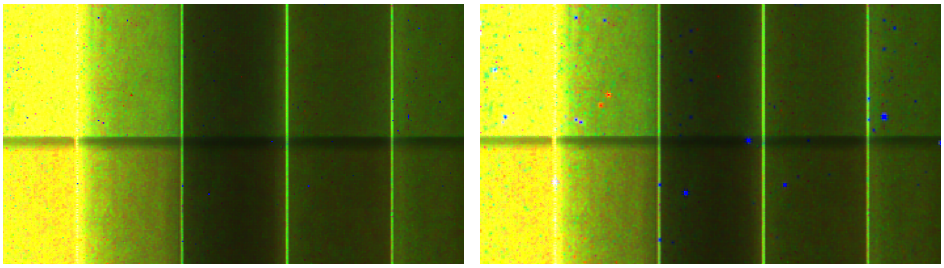

(a) Inpaiting TV image **(b)** Inpainting Sobolev image

Figure 6.8: Cylinder real images acquired by the reconstruction methods using composite pixels with regular pattern

3D reconstructed images

The methods that presented better performance were Inpaiting TV and Inpainting Sobolev and the corresponding PSNR of the 3D reconstructed images is 25.929 dB and 25.603 dB, respectively. The 3D reconstructed images acquired by these two methods are presented in **Figure 6.9**.

Figure 6.9a presents better image quality compared to the image acquired by Inpainting Sobolev due to the fact that **Figure 6.9b** presents more blue pixels in the inner circle. Both images present more artifacts when compared to the original image that comes from the approximations in the calibration of the 3D reconstructed program. It is evident that **Figure 6.9b** presents more artifacts which is backed by the darker circles.

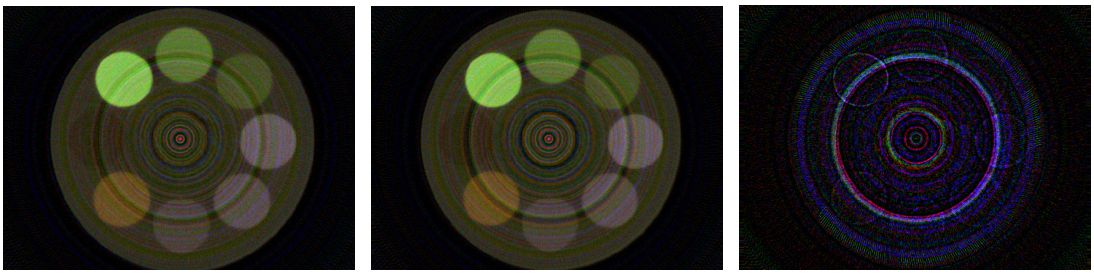

(a) Cylinder image acquired by Inpainting TV

(b) Cylinder image acquired by Inpainting Sobolev

(c) Difference between the 3D original image and 3D image acquired by Inpainting TV

Figure 6.9: 3D reconstructed cylinder images and the image acquired by the difference of the 3D original image and the reconstructed image. The composite pixels have a regular pattern

In order to see which kind of data the reconstruction method recovered, in **Figure 6.9c** it is presented the image acquired after performing the difference between the 3D reconstructed original image and the image acquired by Inpainting TV. The coloured pixels presented in **Figure 6.9c** are the data that the recontruction method was not able to recover. Therefore, it is verified that the third energy range that corresponds to the blue color component was not well recovered and that the edges of the tubes were not well reconstructed.

6.3 Mask with Random Pattern

The experimental procedure applied was the same as in the previous section, where two situations were tested, images with presence of noise and images with no noise. The results that will be demonstrated in this section refer to the simulation of composite pixels with a random pattern, therefore, the spatial resolution will be evaluated when the energy channels are configured randomly.

6.3.1 Simulated phantom image

In this section, the regular pattern was studied an a careful analysis was made, therefore, the results of all the reconstruction methods will be shown, but just the images which showed better quality will be displayed.

Noiseless images

The performance evaluation of the reconstruction methods is presented in **Table 6.7**. The simulated phantom images that were submitted to the reconstruction were noiseless.

The method that presented better performance in recovering data from noiseless images is Demosaicing TV. Overall all the methods have very good performance due the fact that the MSSIM values are very close from each other and their PSNR values are all above 40 dB.

Table 6.7: Phantom image evaluation parameters acquired with composite pixels with random pattern and in the noiseless situation

	PNSR	MSSIM
Linear Interpolation method	40.99	0.997
Total Variation method	45.35	0.999
Sobolev method	40.59	0.997
Demosaicing by FS	42.37	0.998
Demosaicing by TV	53.16	0.999

Figure 6.10 presents the images acquired by the two reconstruction methods that presented better performance. The observations seen in the image acquired by Demosaicing FS are very equivalent to the ones made in the acquired image using a regular pattern. However the Demosaicing FS image acquired using random pattern compared to the Inpainting TV image presents more unrecoverable pixels which is confirm by the lower PSNR and MSSIM values in **Table 6.7**. Comparing **Figure 6.10a** and **Figure 6.10b**, it is evident that both methods didn't recover the edges, however, the pixels that form the edges of the balls are more coloured in the Inpainting TV image. **Figure 6.10a** presents worst PSNR and MSSIM values due to existence of blue coloured pixels inside of the cylinder, which means that this method didn't recover the first and third energy range image.

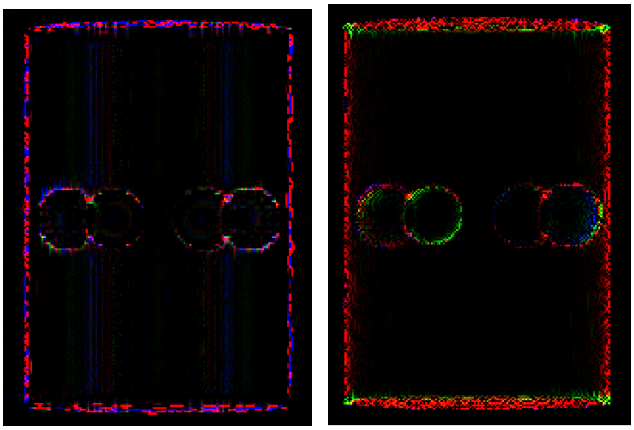

(a) Original image minus Inpainting TV image

(b) Original image minus Demosaicing TV image

Figure 6.10: Simulated phantom images acquired by the difference between the original simulated phantom image and the image acquired by the reconstruction methods. The images submitted to reconstruction are noiseless

Noisy images

Table 6.8 presents the PSNR and MSSIM values of the images acquired by the reconstruction methods.

Table 6.8: Phantom image evaluation parameters acquired with composite pixels with random pattern and in the noisy situation

	PNSR					MSSIM				
	10	20	25	30	40	10	20	25	30	40
L.Int.	22.54	32.034	35.98	38.79	40.71	0.266	0.719	0.878	0.954	0.992
In. TV	23.97	33.33	37.27	40.39	42.89	0.813	0.925	0.971	0.992	0.994
In. Sobo	23.66	32.91	36.60	38.96	40.42	0.309	0.770	0.907	0.966	0.995
Dem. FS	27.38	35.62	38.72	40.80	42.20	0.548	0.887	0.949	0.979	0.995
Dem. TV	27.46	36.65	41.09	45.11	50.15	0.538	0.892	0.958	0.985	0.998

Demosaicing TV images present better image quality independently of the level of noise. Demosaicing FS follows as the method with better performance. Linear Interpolation method is the methods that shows lowest performance comparing to the other reconstruction methods. However, this method presents better image quality when the level of noise is low. This is observed due the fact that Linear Interpolation is a very simple method, and as it was ascertained before, when the amount of partial measurements is high and the level of noise is low, this method present good performance in recovering the missing data. Demosaicing FS is the second best method concerning to the performance, however at an SNR input of 49 dB, its performance is lower compared to Inpainting TV method.

The MSSIM values of the images acquired by Demosaicing FS and Demosaicing TV are very close to each other with the variation of the level of noise, as demonstrated in **Table 6.8**.

This is concluded due the fact that the structure similarity is higher, but in the PNSR values, Demosaicing TV presents better values apart from the level of noise.

Figure 6.11 presents the images acquired by the two methods that showed better performance. These methods are: Demosaicing TV and Demosaicing FS. As stated, the images displayed are regarding to images with a level of noise controlled by a SNR input of 25 dB.

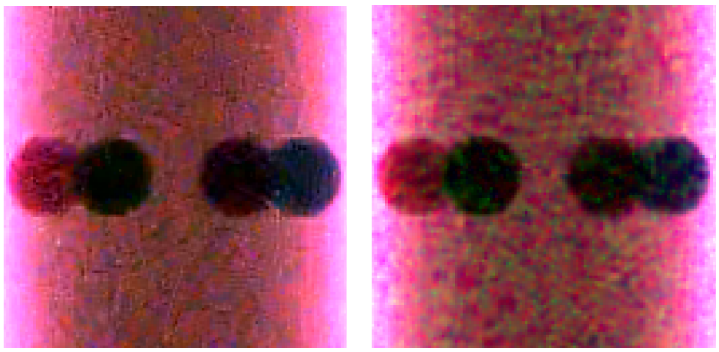

(a) Demosaicing TV resulted image

(b) Demosaicing FS resulted image

Figure 6.11: Simulated phantom images acquired by the reconstruction methods

Figure 6.11a presents better quality, which is proved by the values presented in **Table 6.8**. Comparing the two images one can see that in **Figure 6.11b** the colour was not well recovered, therefore the presence of several pixels whose colour is one of the RGB colour filter system decreases the image quality.

3D reconstructed images

The 3D reconstructed images represent a simulation of the image acquired using composite pixels which have a random pattern. The methods that presented better performance according to the quality of the 2D images are the Inpainting TV and the Demosaicing methods. Subsquently, an analysis was made between these three methods, and it was concluded that Demosaicing TV was the method that presented better performance. The image that presented better MSSIM value is the one acquired by Demosaicing TV, whose value is 0.9048. The MSSIM values of the images acquired by Inpainting TV and Demosaicing FS are 0.7846 and 0.7478, respectively. The images are presented in **Figure 6.12a** and are the ones acquired by the Demosaicing TV methods and **Figure 6.12b** Inpainting TV method, whose PSNR value is 31.806 dB and 27.396 dB, respectevily. The PSNR value of the image acquired by Demosaicing FS is 22.824, which is much lower than the other two methods, therefore it is evident the less quality that the image presents.

When comparing **Figure 6.12a** and **Figure 6.12b** it is visible that the image acquired by Demosaicing TV presents less beam hardening effect than the image acquired by Inpainting TV. The balls of the **Figure 6.12b** present less noise due to the fact that the colour is more homogeneous. These observations are confirmed by the higher PSNR value of **Figure 6.12b**.

Unlike the noiseless situation, the 3D reconstructed images that presented better quality in the noisy case are the images acquired by Demosaicing FS and Demosaicing TV. The differences

between the evaluation parameters of the images acquired by the Demosaicing methods and the Inpainting TV methods are very low. The PSNR values of the images acquired by Demosaicing TV, Demosaicing FS and Inpainting TV are 19.870 dB 19.429 dB and 19.069 dB, respectively. Therefore,the image acquired by Demosaicing TV method presents the higher PSNR value. The images that are in **Figure 6.12** are the images acquired by the Demosaicing methods in the noisy situation.

The differences between **Figure 6.12c** and **Figure 6.12d** are very low, however in the image acquired by Demosaicing FS one can see traces that connect the balls. These evidences justify the fact that the PSNR value of the image acquired by Demosaicing FS is lower than the PSNR of the **Figure 6.12d**. The structures in both images are not well recovered due to the fact that MSSIM values of the images acquired by Demosaicing TV and Demosaicing FS are 0.2087 and 0.1963, respectively.

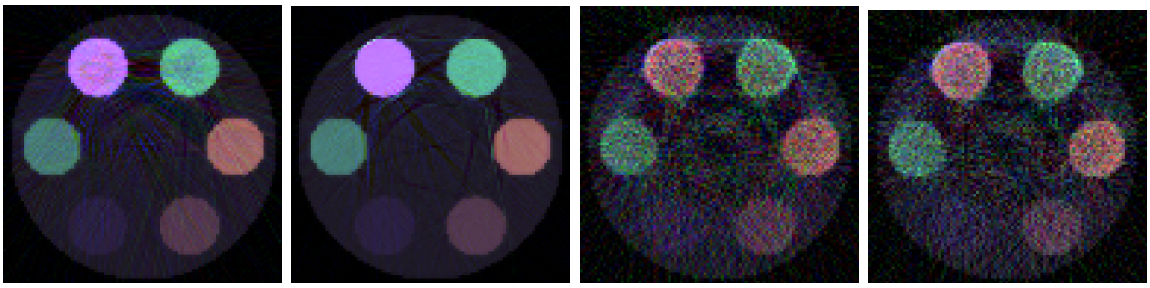

(a) Inpainting TV image in the noiseless case

(b) Demosaicing TV image in the noiseless case

(c) Demosaicing FS image in the noisy case

(d) Demosaicing TV image in the noisy case

Figure 6.12: 3D reconstruction of the simulated phantom images acquired by the reconstruction methods using a random pattern.

6.3.2 MOBY phantom image

As previously seen, this section will be divided into two parts: reconstruction methods applied to images with noise and without noise.

Noiseless images

The evaluation performance is shown in **Table 6.9**.

Table 6.9: MOBY image evaluation parameters acquired with composite pixels with random pattern and in the noiseless situation

	PNSR	MSSIM
Linear Interpolation method	45.11	0.997
Total Variation method	50.19	0.999
Sobolev method	44.93	0.997
Demosaicing by FS	47.05	0.998
Demosaicing by TV	58.99	0.999

Table 6.9 shows that Demosaicing TV is the best reconstruction and compared to the other methods, its evaluation parameters, are much greater. Inpainting Sobolev is the method with lowest evaluation parameters.

Figure 6.13 presents the difference between the original MOBY image and the image recovered by the reconstruction methods. Inpaiting TV and Demosaicing TV will be presented since they are the methods with better performance. The image acquired by the Demosaicing FS method will not be displayed due to the fact that its PSNR and MSSIM values are very close to the PSNR and MSSIM values of the images acquired by Inpainting TV.

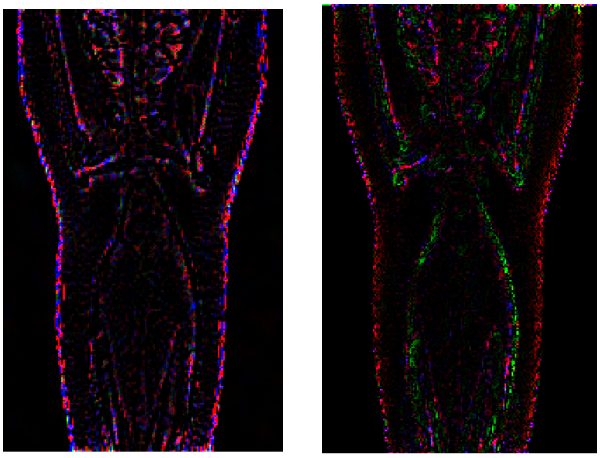

(a) Original image minus Inpainting TV image

(b) Original image minus Demosaicing TV image

Figure 6.13: Images acquired by the difference between the original MOBY image and the images resulted from the reconstruction methods

Comparing the images from **Figure 6.13**, **Figure 6.13b** presents a better image quality due the fact that the edges are less coloured than on the other images. It is noticeable the lower performance in the image acquired by the Inpainting TV, since many pixels are coloured, specially in the contours. **Figure 6.13a** presents lower image quality due to the presence of sharper coloured pixels. The edges in **Figure 6.13b** are less coloured than in the image acquired by Inpainting TV.

Noisy Images

Table 6.10 presents the PSNR and MSSIM values regarding to the MOBY images reconstructed.

Demosaicing TV presents the best results, however with the increase of level of noise which is equivalent to say at low input SNR, Demosaicing FS presents better results than Demosaicing TV, as demonstrated in **Table 6.10**. Linear Interpolation methods have low PSNR values, nonetheless at an input SNR of 40 dB, the Linear Interpolation showed better results than Inpainting Sobolev. Therefore, the methods that showed better performance are the Demosaicing TV and Demosaicing FS method. The reconstruction methods that presented lower evaluation parameters are Linear Interpolation and Inpainting Sobolev.

Table 6.10: MOBY image evaluation parameters acquired with composite pixels with random pattern and in the noisy situation

	PNSR					MSSIM				
	10	20	25	30	40	10	20	25	30	40
L.Int.	22.59	32.35	36.87	40.65	44.39	0.264	0.726	0.883	0.956	0.993
In. TV	24.01	33.39	38.10	42.05	48.51	0.313	0.782	0.913	0.968	0.995
In. Sobo	23.75	33.41	37.74	41.20	44.36	0.309	0.773	0.907	0.966	0.994
Dem. FS	27.54	36.46	40.22	43.34	46.44	0.553	0.893	0.955	0.981	0.996
Dem. TV	27.38	36.81	41.35	45.69	52.91	0.541	0.893	0.959	0.985	0.997

The MSSIM values resulting from the images acquired with the Inpainting Sobolev and the Inpainting TV methods present very similar values as demonstrated in **Table 6.10**; the same does not happen when it comes to the PSNR values. As stated, PSNR metric evaluates the signal noise ratio and this metric does not imply better perceived quality. The fact that MSSIM values are close in different methods means that the structures were equally recovered.

Figure 6.14 presents the images acquired by the two methods that showed better performance: Demosaicing TV and Demosaicing FS. The image acquired by Inpainting TV will be not displayed due to the fact that the PSNR and MSSIM are much lower than the other two methods. After a pre-analysis of the image, it was concluded that the PSNR and MSSIM values match the quality of the resulting image, which is much less than in the Demosaicing methods.

When comparing **Figure 6.14a** and **Figure 6.14b**, the quality of image acquired by Demosaicing TV is much higher than the image acquired by Demosaicing FS. The Demosaicing FS method didn't completely recover the missing information, especially the pixels from the second energy band. This observation can be made because of the presence of green pixels, therefore, the edges are more defined in **Figure 6.14a**, while **Figure 6.14b** presents not recovered pixels, and the image is very smooth.

(a) Demosaicing TV resulted image

(b) Demosaicing FS resulted image

Figure 6.14: MOBY images acquired by the reconstruction methods

3D reconstructed images

After the analysis of the evaluation parameters of the 2D reconstructed images, it was verified that in noiseless images the methods that presented better performance are the De-

mosaicing methods and Inpainting using Total Variation minimization. The 3D reconstruction program developed at the CPPM was performed in the images acquired by these three methods. Consequently it was perform the evaluation of the resulted images and it was seen that Demosaicing TV presented the higher PSNR value (36.647 dB). The images acquired using the Demosaicing FS method presented a similar PSNR value which value is 36.191 dB. The metric that evaluates the structure and constrast similarity doesn't present the same behaviour. The images that presented better MSSIM are the ones acquired by Inpainting TV, which PSNR value is 34.783 dB. In order to understand these observation, the 3D reconstructed images that will be displayed in**Figure 6.15** are regarding to the Inpainting TV and Demosaicing TV.

The PSNR of the image acquired by Inpainting TV is lower than the PSNR acquired from Demosaicing TV due to the fact that the image presented in **Figure 6.15c** is much smoother than **Figure 6.15d**. However, as stated, the MSSIM value of the image **FIgure 6.15c** is 0.9636 which is higher than the MSSIM value of the image acquired by Demosaicing TV because of the amount of contrast. The contrast of the images comparing to the original is lower in the **Figure 6.15c**.

Regarding to the situation where noise was added to the images, it was verified that the images that presented better quality are the ones acquired by Demosaicing methods and Inpainting TV method. As in the noiseless case, the reconstruction method that presented better performance in the 3D reconstruction images was the Demosaicing TV. Inpainting TV was the method that presented worst PSNR and MSSIM values. The images acquired by Demosaicing TV and Demosaicing FS had very similar MSSIM values and the PSNR values equal to 27.088 dB and 26.685 dB, respectively. Therefore the images that will be displayed in **Figure 6.15** are the two methods with higher PSNR values. In the two last images presented in **Figure 6.15** it is evident that the method that presented better performance is the Demosaicing TV. The image acquired by Demosaicing FS presents a big amount of green pixels which are justified by the low recovery performance.

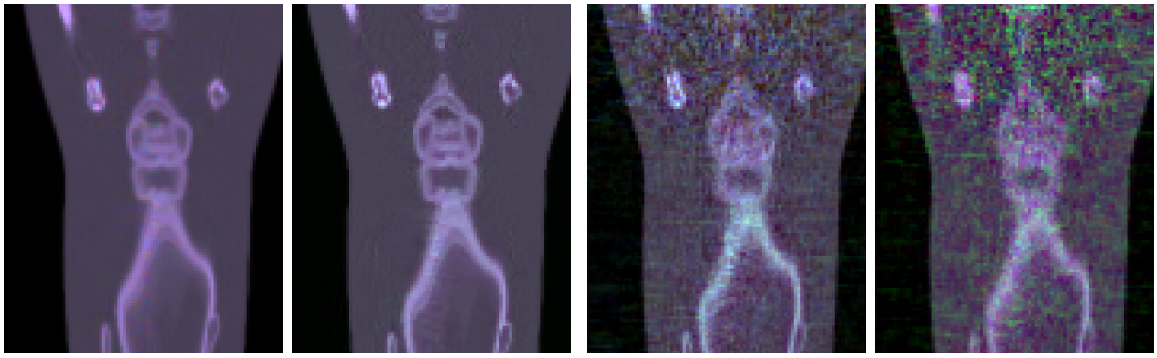

(a) Inpainting TV image image in noiseless case

(b) Demosaicing TV image in noiseless case

(c) Demosaicing TV image image in noisy case

(d) Demosaicing FS image image in noisy case

Figure 6.15: 3D reconstruction of the MOBY images acquired by the reconstruction methods using a random pattern.

6.3.3 Real Data

In this section a study of the performance of the reconstruction in the real data images using composite pixels with random pattern will be done, following the 3D reconstruction using the code made by [4].

Cylinder images

In this section it will be presented the results of the cylinder images after applying the reconstruction methods. **Figure 6.11** presents the evaluation parameters of the images acquired by the five reconstruction methods.

Table 6.11: Evaluation parameters that evaluate the quality of the Cylinder images acquired by the reconstruction methods. The mask used to recreate the composite pixel concepts has a random pattern

	PNSR	MSSIM
Linear Interpolation method	41.274	0.9754
Total Variation method	42.607	0.9801
Sobolev method	42.108	0.9786
Demosaicing by FS	41.893	0.9741
Demosaicing by TV	43.001	0.9755

Demosaicing TV is the method that presents better PSNR value, however the MSSIM value of this method is lower than the MSSIM value of the Inpainting methods. The method that presents better MSSIM value is Inpainting TV. Therefore, an image analysis will be presented in order to understand the differences between the values of the evaluation parameters. The images that are displayed in **Figure 6.16** relate to the methods that presented better performance: Demosaicing TV and Inpainting TV.

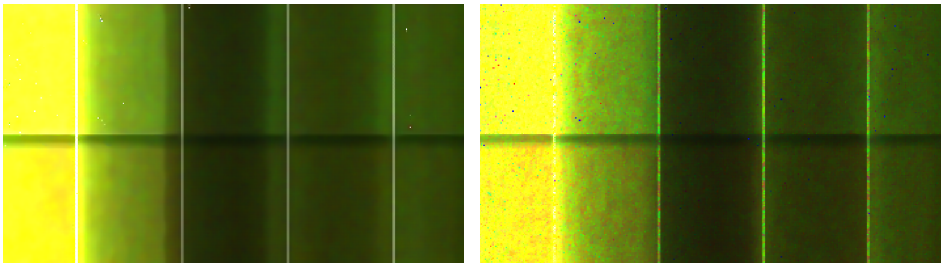

(a) Demosaicing TV resulted image

(b) Inpainting TV resulted image

Figure 6.16: Cylinder real images acquired by the reconstruction methods using composite pixels with random pattern

As stated, Demosaicing TV presents better PSNR value than the other methods, which is confirmed by **Figure 6.16a**. By comparing the image that results from the Demosaicing TV method with the other images, one can observe that the signal-noise ration is lower due the fact that the image is smoother and sharp coloured pixels are not visible unlike in **Figure 6.16b**.

However the MSSIM value of the image resulted from Demosaicing TV is lower than the other method due to the over smoothness of the image.

3D reconstructed images

The methods that presented best performance after using composite pixels with a random pattern are Demosaicing TV and Inpainting TV, whose PSNR values are equal to 25.005 dB dB and 26.711 dB, respectively. Therefore, according to the PSNR, Inpainting TV presents better spatial resolution. The 3D reconstructed images are presented in **Figure 6.17**.

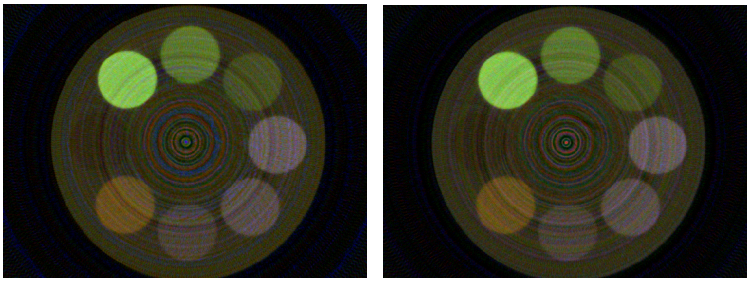

(a) Demosaicing TV image **(b)** Inpainting TV image

Figure 6.17: 3D cylinder images reconstructed image using composite pixels with a random pattern

The image acquired by the Demosaicing TV method presents a lower PSNR due to the range of colours, as shown in **Figure 6.17a** , a high number of high blue pixels can be observed compareed to the Original image. Therefore, the third energy range was recovered but the range of values that was recovered turn out higher than the original range. In the image acquired using Inpainting TV, the range of values is more similar to the original image, which is justified by the PSNR value.

6.4 Comparison between the two composite pixels patterns

In this section, for each image, a study to ascertain which mask pattern provided better quality. As in the previous section, two situations will be tested, images with noise and with no noise. Since the main goal of this research project is to conclude which method gives better spatial resolution, the images that will be compared are the 3D reconstruction images.

With regards to the Simulated phantom images, in the situation where the images are noiseless, the Demosaicing using Total Variation minimization presented better performance in the 2D reconstructed images. This was observed in both patterns that the composite pixels followed. The Demosaicing TV presented much higher PSNR and MSSIM values in both patterns comparing to the other methods. Besides this observation, it was also verified that the composite pixels that followed a random pattern presented a higher PSNR value (53.612 dB) comparing to the regular pattern (47.423 dB). However, after the 3D reconstruction, the images that presented better image quality were acquired by the Demosaicing TV method and the Linear Interpolation method according to the random and regular pattern, respectively. After the analysis of the 3D

reconstructed images, the image acquired by Linear Interpolation showed by far better quality using a Bayer pattern. However, considering the sharp differences between the PSNR values of the 2D reconstructed images between the two patterns, it was concluded that the composite pixels should follow a random pattern. Therefore, combining the observations made regarding the 3D reconstruction, it was determined that in the noiseless case the reconstruction of the Simulated phantom image should be done by the Linear Interpolation method using a composite pixels with a random pattern.

In the noisy situation, the method that presented better performance in 2D and 3D reconstruction was Demosaicing TV. The pattern of the composite pixels that provides better image quality and spatial resolution was the regular pattern. The differences between the PSNR values of the Demosaicing TV method and Demosaicing FS method was less than 1 dB. Therefore, both Demosaicing methods presented better results comparing to the other methods.

As for as the MOBY images the amount of detail is much higher than in the simulated phantom images. In the situation where the images were noiseless, the method that presented better evaluation parameters concerning the 2D images was Demosaicing TV. The difference between the performance of Demosaicing TV in the two patterns is approximately 5 dB, therefore, composite pixels using a random pattern provided better image quality. In the 3D reconstructed images, the methods that presented best evaluation were not the same in the two patterns. In the case where the composite pixels followed a random pattern, the method that showed best performance was Demosaicing TV and in the regular pattern was Linear Interpolation. The differences between the PSNR of these two methods is about 2 dB, where Demosaicing was the method that presented best performance. One important aspect that was noticed is the fact that in the random pattern the Linear Interpolation and Demosaicing FS have very similar PSNR values. This way, in noiseless images that present more detail as MOBY images, the composite pixels should have a random pattern and in order to recover the information it should be use the Demosaicing TV method.

In the situation where was added noise to the images before performing the reconstruction, one can observe that Demosaicing TV presented better results using a regular composite pixels pattern, and in the 2D reconstruction the method that presented better performance is Demosaicing FS using a regular mask. Therefore, the first observation that is made is that the reconstruction method concerning this type of image showed better results with the use of a regular pattern. Due to the results presented before, the 3D reconstructed image acquired by Demosaicing FS using a regular mask showed to be visibly better than the 3D reconstructed image acquired by Demosaicing TV.

In the 2D real data images, The images acquired using composite pixels with a regular pattern presented Inpainting TV, followed by Inpainting Sobolev. In this situation, it was verified that Demosaicing TV presents PSNR and MSSIM values close from the Inpainting Sobolev. The method that presented better performance in the random pattern was Demosaicing TV and Inpainting TV whose PSNR values are equal to 43.001 dB and 42.607 dB, respectively. One important remark is that the image that presents better quality according to the MSSIM is the Inpainting TV.

With regards of the results of the 2D cylinder images, it was seen that the random pattern presented better image quality. However after the 3D reconstruction, it was verified that in the both composite pixels pattern, the Inpainting TV method presented better PSNR values, and the pattern that provided better spatial resolution was random pattern. This image presents

better quality due to the fact that the method performed a better recovery on the artifacts caused by the detector configuration. Comparing **Figure 6.9a** and **Figure 6.17b**, it is verified that the circles caused by the detector configuration presents darker colour. Combining the low recovery of these portions with the calibration approximations of the 3D reconstruction program, it is concluded that for these set of images the best method is Inpainting TV using composite pixels with a random pattern. An important observation is that in both patterns it was ascertained that the third energy range was not well recovered which is justified by the fact that the calibration procedure is more difficult at 33.2 keV than at 25.5 keV or 21 keV. As mentioned, the third band corresponds to an energy range of 33.2 keV - 40 keV and in order to select an energy between this range, each pixel was tuned by an energy threshold. For this purpose, the tension of the X-ray source had to be limited to 40 kVp so that the maximum energy value counted by the pixel would be 40 keV. Therefore the higher the energy is, the higher is the calibration procedure.

6.5 Analysis of the Spectral images using composite pixels

The use of composite pixels in spectral images has several advantages as the reduction of the absorbed dose, it turns the K-edge imaging more robust with regards to animal positioning and allows the image reduction. Therefore, in this section will presented the 3D reconstructed images that presented better spatial resolution and their colours will be related with the solutions that the structures of each image contain. For this purpose the images that will be taken under analysis concern the situation where the noise was not applied.

Figure 6.18 shows the K-edge energies of two components: iodine and silver, which was already demonstrated.

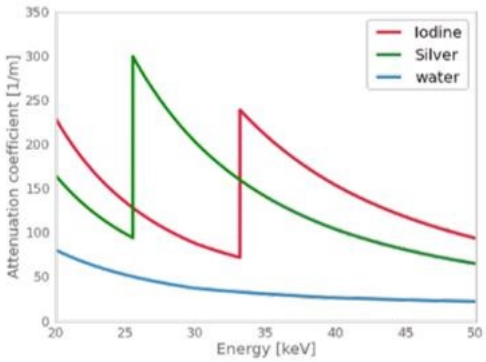

Figure 6.18: Graphic representation of the Photon Attenuation coefficients

As mentioned in the previous sections, three energy ranges were applied, where each energy range corresponds to an image. Since each energy range is related to a colour of the RGB colour system, the images that result from the reconstruction methods will be colour images. The use of composite pixels compromises the spatial resolution, therefore this work aims at in finding the reconstruction method that improves the spatial resolution. The images presented in **Figure B.4b**, **Figure B.5b** and **Figure B.6b** represent the use of composite pixels at full spatial resolution. The goal of this work consists in finding the best reconstruction method for data

recovery from the partial measurements and that way providing an image equivalent to the images referred above.

In the simulated phantom images, the elements present different colours, as demonstrated in **Figure 6.4a**. According to the analysis made in the previous section, the image that will be displayed is the 3D simulated phantom image acquired by Linear Interpolation method using a regular pattern.

The structures in green correspond to the balls that contain silver nitrate, thus after analysing **Figure 6.18** it is clear that the range that contains higher silver attenuation coefficient is the second energy range. As stated, the second energy range corresponds to the second colour component of the RGB system that is the green colour. Therefore, the structures acquired after applying the composite pixels will have green colour. The structures that have a purple colour are the ones that contain Iomeron that consists in a mixture of Iodine. **Figure 6.18** shows that the Iodine attenuation coefficients are higher in the first and third energy range, which according to the RGB colour system correspond to the red and blue colour component, respectively. Therefore by combining these two colours, the structures will present a purple colour, as demonstrated in **Figure 6.4a**. The other two structures shown in **Figure 6.4a** present an orange/brown colour. These structures contain water and bone as presented in **Figure B.1** which is confirm by **Figure 6.4a** since the high values attenuation coefficients of these elements is found in the first energy range that corresponds to the red channel.

In the 3D reconsctructed MOBY images, it is verified that the predominant colour is purple, as demonstrated in **Figure 6.15d**. After the analysis of the percentage of each colour component in each pixel it was seen that the colour that has bigger percentage is the blue colour. The colour that constitute the structure is a brighter purple which indicates that these pixels have a higher percentage of blue colour. Since this image is a simulation of a mouse injected with Iomeron, the brighter colour mentioned is justified by the fact that the Iodine attenuation coefficient is higher in the third energy range which corresponds to the blue colour component.

The 3D reconstructed cylinder image, as demonstrated in **Figure 6.17a** presents several structures with different colours whose constitution was already defined in the **Appendix B**. This image consists in the acquisition of a phantom that contains several cylinder structures in which solutions of nitrate silver were injected, iodine and copper sulfate. The energy ranges applied to the real data were the same as in the MOBY and the simulated phantom image. As in the 3D reconstructed simulated phantom image, the 3D cylinder image follows the same principle since the same energy ranges and colour components were used. The solution that was not used in the other images is the copper sulfate, whose higher attenuation coefficients are found in the first energy range, therefore its K-edge energy is 8.97 keV. As demonstrated in **Figure 6.18** after an abrupt increase of attenuation coefficient, this decreases and therefore the attenuation of this element in the other energy ranges will be lower.

Chapter 7

Conclusion

Computed Tomography is an imaging diagnostic technique that has the ability of visualizing the inner structure of an object, exploiting the position dependent absorption of the incoming X-ray radiation. The images are acquired in different projections that combine with the reconstruction algorithms, producing a 2D image of the analysed sample. One problem faced by Computed Tomography is the challenge with the differentiation and classification of different tissue types. Therefore, one technique that solves this challenge is the use of Spectral Computed tomography whose energy sensitive detector is used to deduce, from the photon energy, the material content of the sample. The advantages of using the Spectral CT over Computed Tomography are that different images can be obtained with different contrasts between the materials inside the object and the artifacts, since the non-monochromaticity of the beam is reduced.

At the CPPM, a new generation of digital X-ray detectors is being used, where this detector explores the spectral information on the detected X-rays. Several studies have already shown that K-edge spectral CT is experimentally feasible and they confirm that contrast agents can be distinguished and quantified independently from a single scan. Therefore, at the CPPM, K-edge imaging technique was exploited and there were research studies were made in order to reduce the absorbed dose on small animals and make K-edge imaging more robust with regards to animal positioning. For this purpose, the CPPM carry out several studies using composite pixels that are set at different energies at the expense of spatial resolution.

The main goal of this research project, as stated, was to perform K-edge imaging on moving objects at full spatial resolution. The strategy used to attain for this purpose consisted in performing several reconstruction methods on the images in order to reconstruct a full spatial resolution image from partial measurements. Therefore, K-edge imaging using composite pixels and reconstruction methods to perform better spatial resolution were successfully achieved.

The conclusion drawn concerning the reconstruction methods was not consistent due to the fact that the images used presented different features. Therefore, it was concluded that, for the simulated images as MOBY and Phantom, the pattern that the composite should follow in the noiseless case is random; and in the noisy case it is the regular pattern. Demosaicing TV presented very good results in both images with the exception of the 3D reconstructed simulated phantom image, where in the noiseless case, the Linear Interpolation method presented higher spatial resolution. Therefore, for noiseless and low detail images the reconstruction method that should be used is the Linear Interpolation.

With regards to the real data images, in which the noise cannot be controlled, it was seen that Inpainting TV presented better MSSIM values in both composite pixels patterns. Therefore, it is not possible to make a correlation between the simulated data and the real data results due to the incoherence of the results. In the simulated data, the reconstruction using the correlation between different images showed better results, while in the real data images it was observed that the reconstructed images achieved have a better spatial resolution when the reconstruction is made individually. This way, the choice of the reconstruction method strongly depends on the features of the images and the level of noise.

Demosaicing methods proved to be a potential method to be used in this field. However, in order to improve the performance, certain aspects should be taken into consideration: the transforms in the frequency domain may cause loss of pixels during the conversion; and image compression and image filtering significantly modify the noise distribution in an unpredictable manner.

The Demosaicing methods used in this work used prior techniques as Total Variation minimization. However, this was applied as a non-constrained problem. In the **Annexe F**, it was demonstrated that the prior techniques as a constrained problem presented better results. Therefore, one possibility of improving Demosaicing algorithm is the inclusion of prior techniques as a constrain problem.

As mentioned at the CPPM, K-edge imaging has been performed using composite pixels of 9 pixels, which implies the use of 3 energy ranges. One study conducted in this research project was the prospect of using more than three energy thresholds. The results showed that by using four energy thresholds there is not a considerable decrease in the image quality. However, Demosaicing methods were not applied to this part, since these methods are used to recover coloured images, the images used consist of three coupled images each corresponding to a colour component. Therefore, Demosaicing methods were just performed in the cases where the composite pixels had three energy ranges. One prospect for future work is the implementation of the concepts of Demosaicing methods, which consist in reconstructing the images through the correlation between pixels from different images using the frequency domain.

The main challenge faced during this research project was the computing time, and therefore this is one of the aspects that should be taken into consideration for future work. Inpainting methods took a long time to reconstruct the images, even with the use of the Toolbox presented in **Annexe E**. Another challenge that had to be faced was the fact that the image input of the 3D reconstruction program could not have negative values. Therefore, in the images to which random noise was added, after being submitted to the reconstruction they had to be manipulated in order to remove those negative values. This manipulation had to be analysed for each image, which altered the output of the reconstruction.

All the reconstruction methods applied in order to achieve better spatial resolution were performed in spectral CT images already acquired. Several studies concluded that iterative methods demonstrate impressive improvements with respect to noise reduction and image quality in general. The methods that were compared by these research studies concerned image reconstruction during CT acquisitions. Therefore, a possible study that could be made is the performance of Demosaicing methods during the spectral CT acquisitions. Since iterative methods showed better results than the analytic methods, and due to the fact that Demosaicing methods consist in ill-posed methods which are similar to iterative methods, the use of Demosaicing methods would be a good challenge to be tested during the image acquisition.

References

[1] N. Barrie Smith and A. Webb. *Introduction to Medical Imaging: Physics, Engineering and Clinical Applications.* Cambridge University Press, 2011.

[2] J. T. Bushberg, J. A. Seibert, E. M. Leidholdt, and J. M. Boone. *The Essential Physics of Medical Imaging.* Lippincott Williams & Wilkins, 2002.

[3] Edgar Kraft. Counting and Integrating Microelectronics Development for Direct Conversion X-ray Imaging. Technical report, Bonn University, 2008.

[4] Mathieu Dupont. *Tomographie spectrale à comptage de photons: développement du prototype PIXSCAN et preuve de concept.* PhD thesis, Aix Marseille Université, 2014.

[5] M. Noori and A. Sadremomtaz. Analytical image reconstruction methods in emission tomography. *Journal of Biomedical Science and Engineering*, 6(1):100–107, 2013.

[6] Dose reduction in dual source dual energy. https://www.healthcare.siemens.com/computed-tomography/technologies-innovations/ct-dual-energy/features-benefits.

[7] C. Kronland-Martinet, F. Cassol, A. Bonissent, Y. Boursier, M. Dupont, F. Debarbieux, and C. Morel. Development of k-edge spectral tomography using xpad3 composite pixels. *IEEE Nuclear Science Symposium and Medical Imaging Conference*, 2014.

[8] JavaScript editor. Introduction to optimization.

[9] L. Condat. A simple, fast and efficient approach to denoisaicking: Joint demosaicking and denoising. *IEEE International Conference on Image Processing*, page 905–908, 2010.

[10] D. Alleysson and B. C. Lavarene. Frequency selection demosaicking: review and a look ahead. *Visual Communications and Image Processing*, 6822, 2008.

[11] P. Delpierre, S. Basolo, J.F. Berar, A. Bonissent, P. Breugnon, N. Boudet, B. Caillot, J.C. Clemens, F. Debarbieux, B.Dinkespiler, R. Khouri, I. Koudobine, V. Matarazzo, C. Meessen, M. Menouni, C. Morel, C. Mouget, P. Pangaud, F. Peyrin, G. Rougon, D. Sappey-Marinier, S. Valton, and E. Vigeolas. Pixscan: Pixel detector ct-scanner for small animal imaging. *Nuclear Instruments and Methods in Physics Research Section A: Accelerators, Spectrometers, Detectors and Associated Equipment*, 571(1-2):425–428, 2007.

[12] W. R. Hendee and E. R. Ritenour. *Medical Imaging Physics.* Wiley-Liss, Inc., 2002.

[13] J. Hsieh. *Computed tomography:principles, design, artifacts, and recent advances.* SPIE and John Wiley & Sons,Inc., 2009.

[14] S. Christofides, D.R. Dance, A. D. A. Maidment, I. McLean , and K.-H. Ng. *Diagnostic Radiology Physics: A Handbook for Teachers and Students.* International atomic energy agency., 2014.

[15] P. Russo and A. Del Guerra. *Molecular Imaging of Small Animals: Instrumentation and Applications.* Springer, 2004.

[16] Arkadiusz Dawiec. *Development of an ultra-fast X-ray camera using hybrid pixel detectors.* PhD thesis, Universit é de la Méditerranée Aix-Marseille II, 2011.

[17] Paola Maria Frallicciardi, Jan Jakubek, Daniel Vavrik, and Jiri Dammerb. Comparison of single-photon counting and charge-integrating detectors for x-ray high-resolution imaging of small biological objects. *Nuclear Instuments and Methods in Physics Research*, 487(1-2):113–122, 2002.

[18] L. Rossi, P. Fischer, T. Rohe, and N. Wermes. *Pixel detector:Fundamentals to Applications.* Springer, 2005.

[19] M. S. M Yusoff, R. Sulaiman, and K. Shafinah. Image reconstruction for ct scanner by using filtered back projection approach. *Journal of American Science*, 8(6):797–803, 2002.

[20] Mats Persson. Reconstruction of spectral CT images. Technical report, Department of Physics, KTH, 2011.

[21] Luiz Gustavo da Rocha Charamba. Reconstrução de Imagens Tomográficas com uso de GPU. Technical report, Universidade Federal de Pernambuco, 2013.

[22] Marcel Beister, Daniel Kolditz, and Willi A. Kalender. Iterative reconstruction methods in x-ray ct. *European Journal of Medical Physics*, 28(2):94–108, 2012.

[23] J. P. Schlomka, E. Roessl, R. Dorscheid, S. Dill, G. Martens, T. Istel, C. B ä umer, and C. Herrmann. Experimental feasibility of multi-energy photon-counting k-edge imaging in pre-clinical computed tomography. *Insights into Imaging*, 53(15):4031–47, 2011.

[24] E. Roessl and R. Proksa. K-edge imaging in x-ray computed tomography using multi-bin photon counting detectors. *Physics in Medicine and Biology*, 52(15):4679–96, 2007.

[25] Shima Aran, Khalid W. Shaqdan, and Hani H. Abujudeh. Dual-energy computed tomography (dect) in emergency radiology: basic principles, techniques, and limitations. *Emergency Radiology*, 21(4):391–405, 2014.

[26] T. R. C. Johnson, B. Krau β, M. Sedlmair, M. Grasruck, H. Bruder, D. Morhard, C. Fink, S. Weckbach, M. Lenhard, B. Schmidt, T. Flohr, M. F. Reiser, and C. R. Becker. Material differentiation by dual energy ct: initial experience. *European Journal of Radiology*, 17(6):1510–7, 2007.

[27] V. Rebuffel, M. Tartare, A. Brambilla, V. Moulin, and L. Verger. Multi-energy x-ray techniques for ndt: a new challenge. In *European Conference on Non-Destructive Testing*, 2014.

[28] RK. Panta, MF. Walsh, ST. Bell, NG. Anderson, AP. Butler, and PH. Butler. Energy calibration of the pixels of spectral x-ray detectors. *IEEE Transactions on Medical Imaging*, 34(3):697–706, 2015.

[29] L. Li, Z. Chen, W. Cong, and G. Wang. Spectral ct modeling and reconstruction with hybrid detectors in dynamic-threshold-based counting and integrating modes. *IEEE Transactions on Medical Imaging*, 34(3):716–28, 2015.

[30] Yothin Rakvongthai, William Worstell, Georges El Fakhri, Junguo Bian, Auranuch Lorsakul, and Jinsong Ouyang. Spectral ct using multiple balanced k-edge filters. *IEEE Transactions on Medical Imaging*, 34(3):740 – 747, 2015.

[31] F. Cassol, M. Dupont, C. Kronland-Martinet, H. Ouamara, A. Dawiec, Y. Boursier, A. Bonissent, J-C Clémens, L. Portal, F. Debarbieux, and C. Morel. Characterization of the imaging performance of a micro-ct system based on the photon counting xpad3/si hybrid pixel detectors. *Biomedical Physics & Engineering Express*, 52(15):4679–96, 2016.

[32] F. C. Brunner, M. Dupont, C. Meessen, Y. Boursier, H. Ouamara, A. Bonissent, C.e Kronland-Martinet, J.-C. Clemens, F. Debarbieux, and C. Morel. First k-edge imaging with a micro-ct based on the xpad3 hybrid pixel detector. *IEEE Transactions on Nuclear Science*, 60(1):103–108, 2012.

[33] M. Dupont, Y. Boursier, A. Bonissent, F. Cassol, C. Kronland-Martinet, F. Debarbieux, and C. Morel. Component separation for spectral x-ray imaging using the xpad3 hybrid pixel camera. *Nuclear Science Symposium and Medical Imaging Conference*, 2013.

[34] L. L. Geyer, U. J. Schoepf, F. G. Meinel, J. W. Nance, G. Bastarrika, J. A. Leipsic, N. S. Paul, M. Rengo, A. Laghi, and C. N. De Cecco. State of the art:iterative ct reconstruction techniques. *Radiology Journal*, 276(2):339–57, 2015.

[35] M. Zhu, S. J. Wright, and T. F. Chan. Duality-based algorithms for total-variation regularized image restoration. *Computational Optimization and Applications*, 47(3):377–400, 2010.

[36] F. Pontana, A. Duhamel, J. Pagniez, T. Flohr, J.-B. Faivre, A.-L. Hachulla, J. Remy, and M. Remy-Jardin. Chest computed tomography using iterative reconstruction vs filtered back projection (part 1): Evaluation of image noise reduction in 32 patients. *European Radiology*, 21(3):627–35, 2011.

[37] A. Winklehner, C. Karlo, G. Puippe, B. Schmidt, T. Flohr, R. Goetti, T. Pfammatter, T. Frauenfelder, and H. Alkadhi. Raw data-based iterative reconstruction in body cta: evaluation of radiation dose saving potential. *European Radiology*, 21(12):2521–6, 2011.

[38] J. Leipsic, T. M. Labounty, B. Heilbron, and J. Earls. Adaptive statistical iterative reconstruction: assessment of image noise and image quality in coronary ct angiography. *American Journal of Roentgenology*, 195(3):649–54, 2010.

[39] J. Leipsic, T. M. LaBounty, B. Heilbron, J. K. Min, G. B. J. Mancini, F. Y. Lin, C. Taylor, A. Dunning, and J. P. Earls. Estimated radiation dose reduction using adaptive statistical iterative reconstruction in coronary ct angiography: the erasir study. *American Journal of Roentgenology*, 195(3):655–60, 2010.

[40] R. Khoury, A. Bonissent, J.C. Cléemens, C. Meessen, E. Vigeolas, M. Billault, and C. Morel. A geometrical calibration method for the pixscan micro-ct scanner. *4th International conference on Imaging technologies in Biomedical Sciences*, 4(7):7–16, 2007.

[41] Carl E. Ravin Advanced Imaging Laboratories. Carl e. ravin advanced imaging laboratories. http://deckard.mc.duke.edu/xcatmobyrobyphantom.html.

[42] Gabriel Peyré. *Advanced Signal, Image and Surface Processing*. IEEE Computing in Science and Engineering, 2010.

[43] Martin Burger. *Inverse Problems*. Institute for Numerical and Applied Mathematics, Germany, 2008.

[44] G. Peyré, S. Bougleux, and L. Cohen. Non-local regularization of inverse problems. *Computer Vision*, 5304(3):57–68, 2008.

[45] R. Vreja and R. Brad. Image inpainting methods evaluation and improvement. *Hindawi Publishing Corporation: The Scientific World Journal*, 2014(2014):11, 2014.

[46] S. Osher, M. Burger, J. Xu D. Goldfarb, and W. Yin. An iterative regularization method for total variation based image restoration. *Society for Industrial and Applied Mathematics*, 4(2):460–489, 2005.

[47] N. Perraudin, D. Shuman, G. Puy, and P. Vandergheynst. Matlab convex optimization toolbox using proximal splitting methods. *UNLocBoX*, 2014.

[48] N. Perraudin and V. Kalofolias. Unlocbox: User's guide: Matlab convex optimization toolbox. *UNLocBoX*, 2008.

[49] M. Neri and E. R. R. Zara. Total variation-based image inpainting and denoising using a primal-dual active set method. *Philippine Science Letters*, 7(2):87–103, 2014.

[50] X.-Q Zhang and J. Froment. Constrained total variation minimization and application in computerized tomography. *Energy Minimization Methods in Computer Vision and Pattern Recognition*, 3757(3):456–472, 2005.

[51] Y. Huang, M. K. Ng, and Y.-W Wen. A fast total variation minimization method for image restoration. *Multiscale Modeling & Simulation*, 7(2):774–795, 2008.

[52] O. Losson, L. Macaire, and Y. Yang. Comparison of color demosaicing methods. *Advances in Imaging and Electron Physics,*, 162:173–265, 2012.

[53] D. Alleysson, S. Süsstrunk, and Jeanny Hérault. Color demosaicing by estimating luminance and opponent chromatic signals in the fourier domain. *Color Imaging Conference*, page 331–336, 2002.

[54] I. Kunina, A. Volkov, and S. Gladilin D. Nikolaev. Demosaicing as the problem of regularization. *Eighth International Conference on Machine Vision*, 2015.

[55] D. Alleysson and S. Süsstrunk. Linear demosaicing inspired by the human visual system. *IEEE Transactions on Image Processing*, 14(4):439–49, 2005.

[56] E. Dubois. Filter design for adaptive frequency-domain bayer demosaicking. *International Conference on Image Processing*, 2006.

[57] L. Condat. A generic variational approach for demosaicking from an arbitrary color filter array. 16^{th} *IEEE International Conference on Image Processing*, 2009.

[58] L. Condat. Joint demosaicking and denoising by total variation minimization. 19^{th} *IEEE International Conference on Image Processing*, 2012.

[59] L. Dai, Y. Zhang, and Y. Li. Bm3d image denoising algorithm with adaptive distance hard-threshold. *International Journal of Signal Processing, Image Processing and Pattern Recognition*, 6(6):41–50, 2013.

[60] Z. Wang, A. C. Bovik, H. R. Sheikh, and Eero P. Simoncelli. Image quality assessment: From error visibility to structural similarity. *IEEE Transactions on Image Processing*, 13(4):600–12, 2004.

[61] Mohamed-Chaker Larabia and S. Sösstrunk. Evaluation of a hyperspectral image database for demosaicking purposes. *Proceedings of SPIE - The International Society for Optical Engineering*, 2011.

[62] Nathanaal Perraudin. Unlocbox - matlab convex optimization toolbox. https://lts2.epfl.ch/unlocbox/doc/utils/index.php.

[63] N. Perraudin. Unlocbox: A simple tutorial. *UNLocBoX*, 2014.

Appendix A

Micro-CT system used at CPPM

Figure A.1 represents a real picture of the XPAD3 camera enclosed in a box, and **Figure A.2** is the XPAD3 detector.

Figure A.1: XPAD detector selled by ImXPAD, [4]

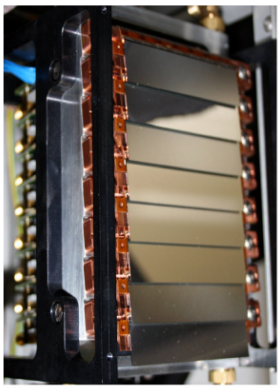

Figure A.2: XPAD3 detector,[4]

The configuration of the PIXSCAN is shown in **Figure A.3**.

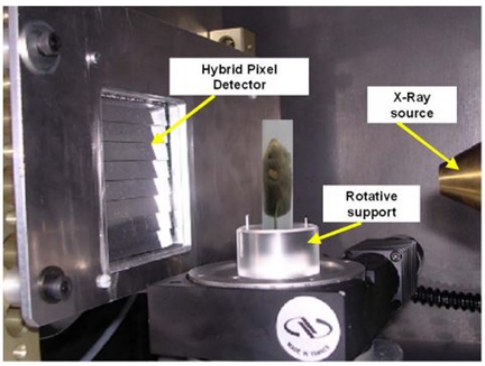

Figure A.3: Photography of the PIXSCAN, [11]

Appendix B

Images acquired at different energy ranges

B.1 Simulated Phantom image

The configuration and constitution of the simulated phantom images is presented in **Figure B.1**.

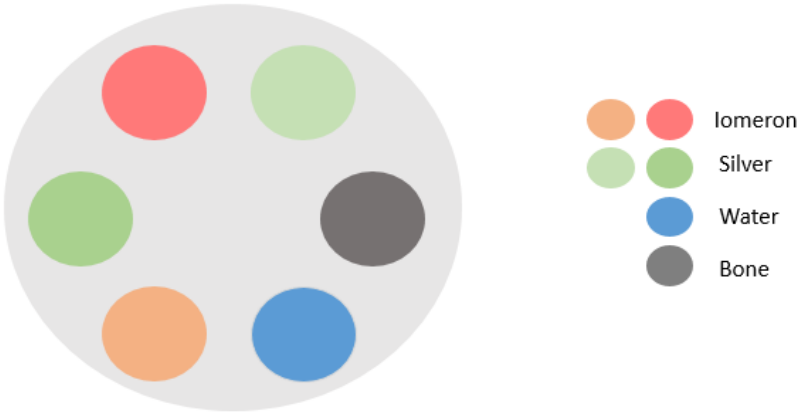

Figure B.1: Simulated Phantom with the corresponding components

In **Figure B.2** it is presented the 1° of the simulated phantom where the first three images represent the simulated phantom in each band.

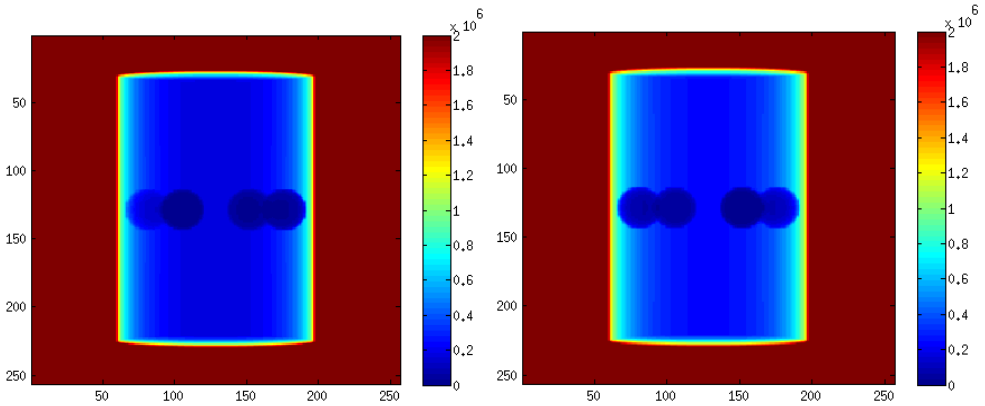

(a) Band 1: 21.0 – 25.5 keV **(b)** Band 2: 25.5 – 33.2 keV

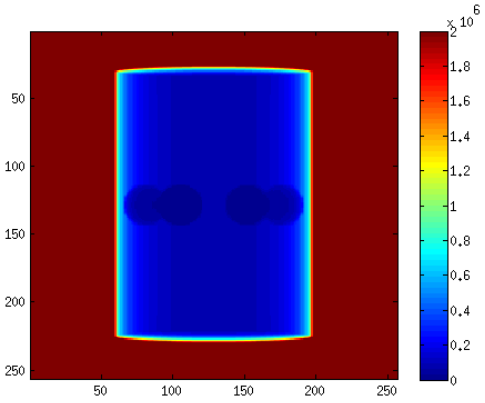

(c) Band 3: 33.2 – 40 keV

Figure B.2: Simulated phantom image

Figure B.3 presents the 3D reconstructed images of the simulated phantom image. Each image represented consists in the 3D reconstructed image acquired at each energy range.

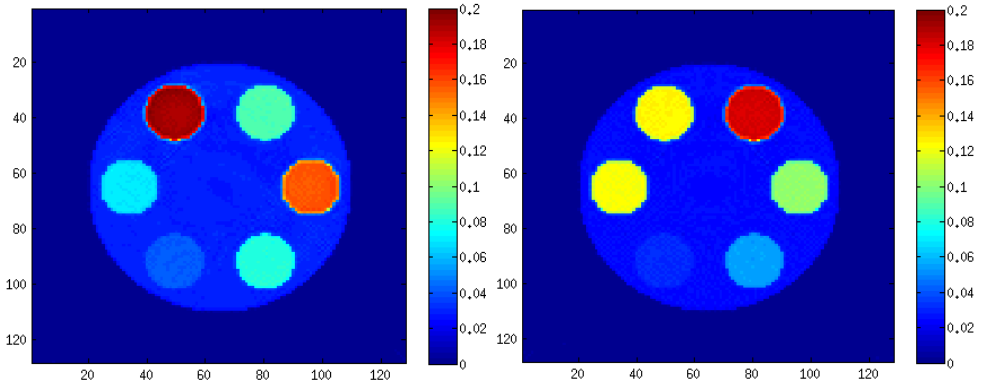

(a) Band 1: 21.0 – 25.5 keV **(b)** Band 2: 25.5 – 33.2 keV

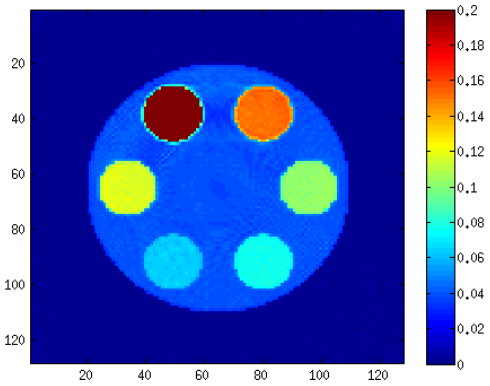

(c) Band 3: 33.2 – 40 keV

Figure B.3: 3D reconstructed images of the Simulated phantom

Figure B.4b, and as visualized it is equivalent to the illustration made in **Figure B.1**.

(a) 2D reconsctructed simulated phantom

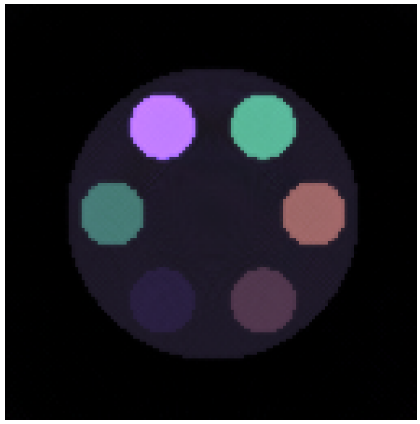

(b) 3D reconstructed simulated phantom coloured image: Multi-spectral image

Figure B.4: Coloured Images: Multi-spectral images

B.2 MOBY phantom image

Figure B.4 presents the MOBY images acquired at three different energy ranges.

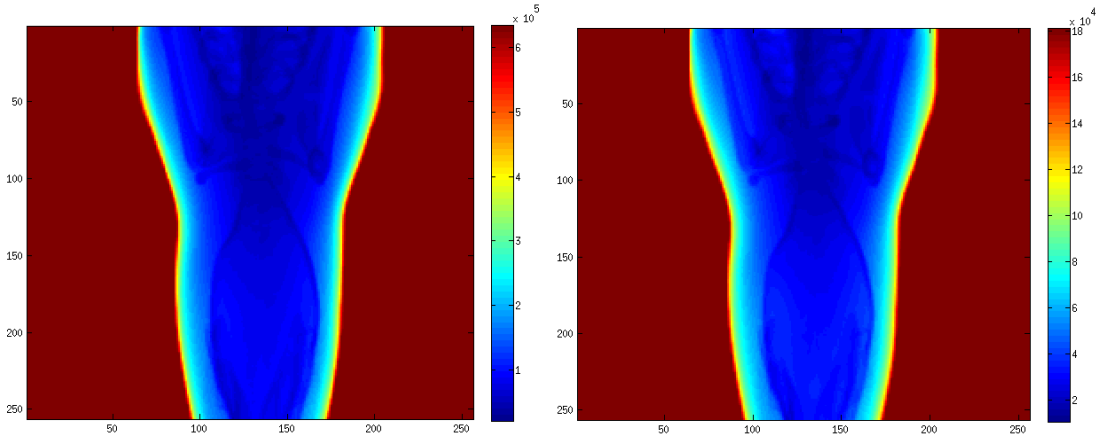

(a) Band 1: 21.0 – 25.5 keV

(b) Band 2: 25.5 – 33.2 keV

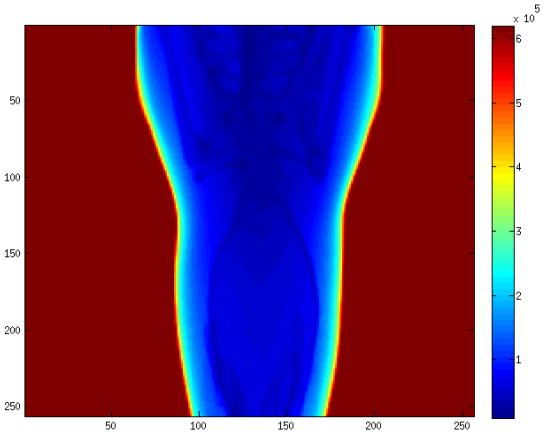

(c) Band 3: 33.2 – 40 keV

Figure B.4: MOBY image acquired at three energy ranges

Figure B.4 presents the 3D reconstruction of the MOBY images acquired at different energies.

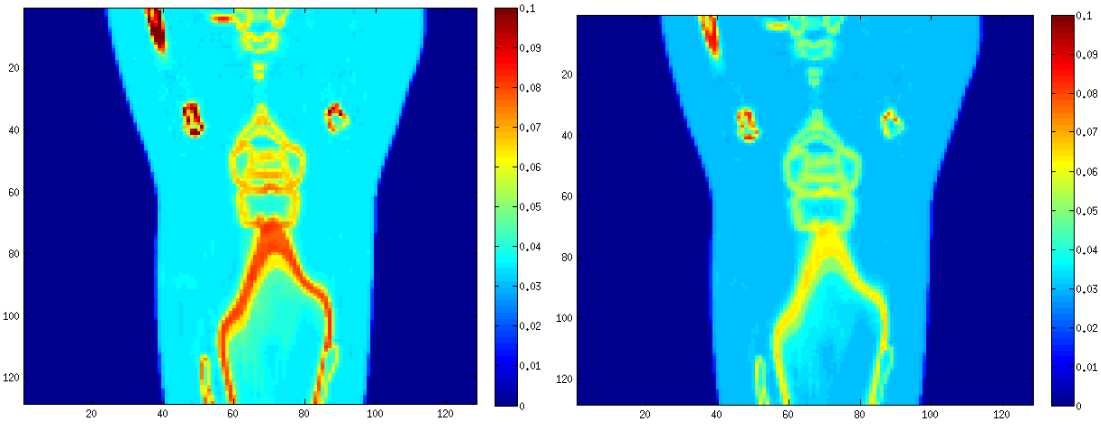

(a) Band 1: 21.0 – 25.5 keV

(b) Band 2: 25.5 – 33.2 keV

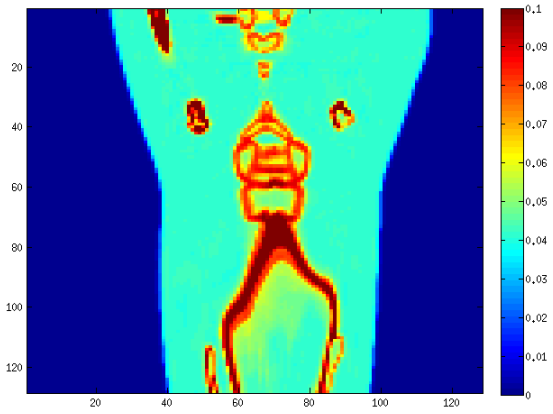

(c) Band 3: 33.2 – 40 keV

Figure B.4: 3D reconstructed images of the Simulated phantom and the resulting image after applying the composite pixels concept

Figure B.5a presents the 2D reconstructed image that is generated by the coupling of the three images acquired at three energies presented in **Figure B.4**. The **Figure B.5b** presents the coloured 3D reconstruction of the MOBY image that resulted from the coupling of the images given in **Figure B.4**.

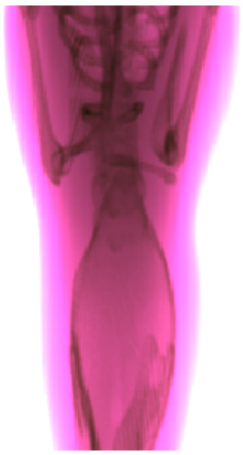

(a) 2D reconsctructed simulated phantom

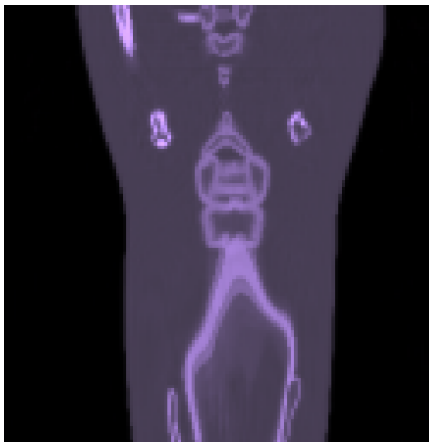

(b) 3D reconstructed simulated phantom coloured image: Multi-spectral image

Figure B.5: Coloured Images: Multi-spectral images

B.3 Real data

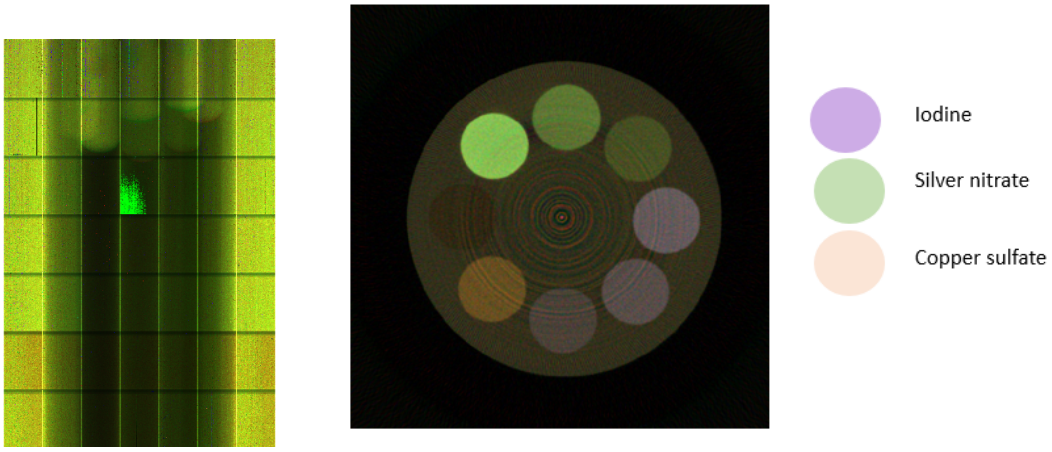

(a) 2D cylinder image

(b) 3D cylinder image

Figure B.6: Real data image acquisition obtained from composite pixels

Appendix C

Composite pixels operation

Figure C.1 represents the multiplication between the first energy range of the simulated phantom image, which is equivalent to the red channel from the RGB colour filter, and the first sub-mask, represented in **Figure 4.2**.

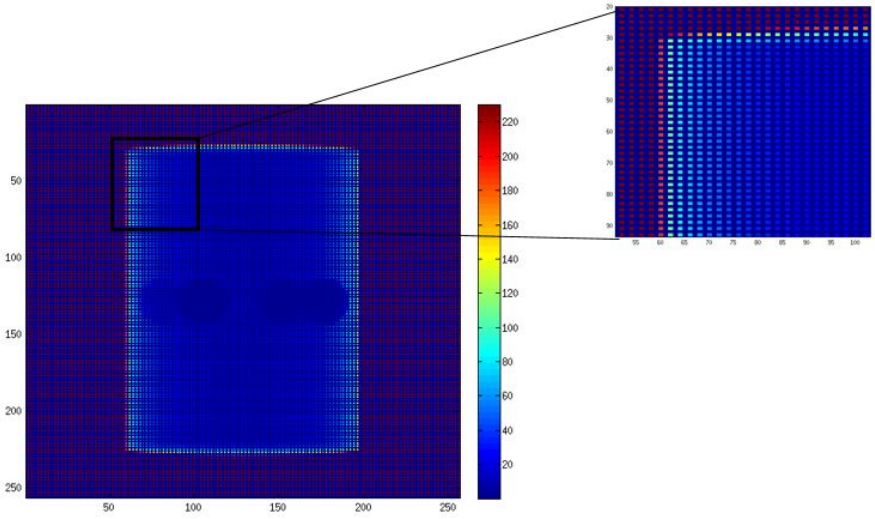

Figure C.1: Illustration of the resulting image acquired by the multiplication of one energy Band and sub-mask

This operation will be performed for each image acquired at a certain energy range. In this work, the image acquired with the first energy range will be multiplied by the first sub-mask; the image acquired with the second energy range will be multiplied by the second sub-mask; and the image acquired with third energy range will be multiplied to the third sub-mask. The sub-masks reffered above are presented in **Figure 4.2**, and the corresponding images that will multiplied are presented in **Figure B.2** and **Figure B.4**. The same is performed in the three data images acquired at three different energy ranges.

Appendix D

Evaluation parameters formulation

The evaluation parameters used in this work in order to evaluate the quality of the images are SNR, MSSIM, CPSNR and CNR. As it will be stated in the development of this project, all the images were normalized and multiplied by 255, due to the fact that the images used to perform the MSSIM evaluation algorithm have to have a maximum of 255.

SNR is the abbreviation of signal-noise ratio and the mathematical formula to calculate this parameter is given in **equation D.1**.

$$SNR = 10 \log_{10} \left(\frac{\|I_{ref}\|^2}{\|I_{ref} - I\|^2} \right) dB \tag{D.1}$$

Where I_{ref} is the original image, and I is the resulting image from the reconstruction algorithm.

The other evaluation is the MSSIM, which is the mean Structural Similarity Index (SSIM) value between 2 images, which are the original image and the image acquired by the reconstruction method. The mathematical formula to perform this evaluation was taken from [60]. This method stipulates that the images are highly structured, and their pixels exhibit strong dependencies which carry information about the structure of the objects present in the image. The MSSIM compares the structures of the reference image I_{ref} and the resulting image acquired with the reconstruction method, I. The similarity measurement is made according to three comparisons: luminance, contrast and structure. Luminance is estimated as the mean of intensity, thus, the luminance comparison function is given by $l(x, y)$. The contrast is estimated by performing the standard deviation, that way, the contrast comparison function is given by $c(x, y)$. Then, the final comparison made is the structure, for this, the image is normalized by its own standard deviation, so that the images compared have unit standard deviation. Thus, the structure comparison function is given by $s(x, y)$, and it is led on these normalized images. The terms x and y are denoted as two non-negative image signals, which have been aligned with each other (e.g. spatial patches extracted from each image).It is important to assert that the three components are independent from each other, and the definition of these is given in [60].

The resulting similarity measure the structure similarity index (SSIM) between two images, given by the **equation D.2**.

$$SSIM(x, y) = [l(x, y)^{\alpha} \cdot c(x, y)^{\beta} \cdot s(x, y)^{\gamma}] \tag{D.2}$$

Therefore, to evaluate the overall image quality it one uses a mean SSIM, named MSSIM, which is given by the **equation D.3**.

$$MSSIM(I_{ref}, I) = \sum_{j=1}^{M} SSIM(x_j, y_j) \tag{D.3}$$

Where x_j and y_j are the image contents at the $j-th$ the local window, and M is the number of local windows in the image.

The other evaluation parameter used to evaluate the reference image and the image resulting from the algorithm is the CPSNR, [61]. Since one of the methods applied in this work is Demosaicing, whose images used are three-dimensional regarding the number of rows, number of columns, and the RGB channels, the common PSNR cannot be used. PSNR is used to evaluate grayscale images, with just two dimensions. Therefore, CPSNR is composite peak-signal-to-noise ratio, which compares the reconstructed images to full colour RGB images. The mathematical formulation used to calculate the CPSNR of a demosaiced image compared to the reference /original image is given in **equation D.4**.

$$CPSNR = 10 \log_{10} \left(\frac{m_I^2}{CMSE} \right) \tag{D.4}$$

Where CMSE is given by the **equation D.5**.

$$CMSE = \frac{1}{3 \times N \times M} \sum_{k=1}^{3} \sum_{i=1}^{M} \sum_{j=1}^{N} \left[I_{ref}(i,j,k) - I(i,j,k) \right] \tag{D.5}$$

Where $I_{ref}(i,j,k)$ is the pixel intensity at location (i,j) of $k-th$ colour component of the original image, and $I(i,j,k)$ of the reconstructed image. And M and N are the height and the width of the image. The parameter k in the images used in this work is referred to the energy bands. The parameter of m_I is the maximum value of the image, since the images were normalized and multiplied by 255, the value of m_I in the reference image is 255.

Appendix E

Inpainting using UNLocBoX toolbox

The Sobolev and Total variation methods described in the previous section have a similar algorithm, whose only difference is the regularization term. In both methods it is necessary to solve a convex optimization problem and as it was shown, it is very time consuming since one needs to find an optimal combination of parameters.

The main problem of using the algorithms referred before happens in the situations where the functions (images) are not smooth. Thus, the algorithm that will be analysed in this section, just like the ones referred, is design to solve a convex optimization problem in the form showed in **equation E.1**, [48].

$$\min_{x \in \mathbb{R}^N} \quad f_1(x) \; + \; f_2(x) \tag{E.1}$$

Equation E.1 can be represented in a more generally form, as the formula given in **equation E.2**.

$$\min_{x \in \mathbb{R}^N} \quad \sum_{n=1}^{K} \; f_n(x) \tag{E.2}$$

Where f_n are lower semi-continuous convex functions from $\mathbb{R}^N$ to $(-\infty, +\infty)$, and f_n have non-empty domains, where the domain of a function is given by the expression in **equation E.3**. This way, f_1 can be defined as a convex and smooth loss function, while f_2 is a lower semi continuous, convex, and non-smooth regulator that induces sparsity.

$$dom \; f \; := \{x \in \mathbb{R}^N \quad f(x) < +\infty\} \tag{E.3}$$

Equation E.2 presents the same formulation as the one showed in the previous section. When both $f_1(x)$ and $f_2(x)$ are smooth functions, gradient descent methods can be used to solve the problem. However, as stated, gradient descent methods cannot be used to solve problems when one of the functions is not smooth.

UNLocBoX is a Matlab convex optimization toolbox that provides a general framework that allows the design of different algorithms, which codes were taken from [62] [48]. This toolbox tries to stay as close to the mathematical problem as possible, which solves the convex

optimization problem of the form given in **equation E.2**. Since Inpainting problems consist in minimizing a regularization, this problem can be solved using this Matlab toolbox, [48] [47] [63]. This toolbox is based on proximal splitting methods, which change the problem into smaller sub problems that can be solved in an iterative way, [48].

UNLocBoX consists in three families of functions, proximity operators which solve small minimization problems and allow a quick implementation of problems; the solvers that are generic minimization algorithms that can work with different combinations of proximity operators in order to minimize functions, and the demonstration files that consist in examples for a better understanding of how to apply the methods, [48] [47] [63]. This toolbox has an unlimited number of convex functions and constraints, which provides a list of useful of proximal and projection operators.

Therefore, the functions provided in this toolbox are able to solve an Inpainting problem, in [47] it is presented the algorithm used to solve the Inpainting problem in this work. As in the methods above, the goal of the method that will be presented is to fill unknown values in order to reconstruct an image close to the original.

In order to perform total variation and Sobolev method using this toolbox, some assumptions are needed in the same way as described in the other methods. First, it is specified the position of the missing data, then it is assumed that the image follows a standard distribution. And since the goal is to work with real data, the method assumes that the known data is subject to some noise δ, which is an expected value of the norm of the noise (standard deviation times square root of number of measurements). Thus, the constraint used to perform the inpainting TV method and the inpainting Sobolev method is given in **equation E.4**, [47] [63].

$$\|Ax - y\|_2 \leq \sqrt{N}\delta \tag{E.4}$$

Where N is the number of known pixels, δ is the noise added to the known data, A is a linear masking operator that is equivalent to the notation used before Φ, x is the vectorised image that will be recovered, and y are the observed noisy pixels. As in the Sobolev and Total Variation described before, in order to simulate the method in images with no presence of noise, the value of δ is 0.

This way, the prior assumption is that the image has a small total variation norm or Sobolev norm. This problem is expressed by the **equation ??** and equation sob, however the TV and Sobolev method using the toolbox uses a constraint. The problem is expressed in the **equation E.5**, [63].

$$\underset{x}{\operatorname{argmin}} \quad \|x\|_{method} \quad \text{subject to} \quad \|Ax - y\|_2 \leq \sqrt{N}\delta \tag{E.5}$$

Where the method tested using the toolbox was Sobolev and total variation regularization, and δ is a free parameter that tunes the confidence to the measurements. Thus, the problem expressed in the equation is TV minimization problem solved with a constraint, however, the optimization theory solution of equation y is equivalent to that of the unconstrained minimization problem given in **equation 5.2**. The advantage of using **equation E.5** is the fact that it takes in consideration the noise level but is it also appropriate for noise-free cases.

The UNLocBoX is based in proximal splitting techniques for solving convex optimization problems, [63]. Proximal operators of a semi-continuous convex function $f : \mathbb{R}^N \to \mathbb{R}$ is defined by the **equation E.6**.

$$prox_f(x) \;:=\; \underset{y\in\mathbb{R}^N}{\operatorname{argmin}} \left\{ \frac{1}{2}\,\|x-y\|^2 \;+\; f(x) \right\} \tag{E.6}$$

The minimization of **equation E.6** has an unique solution for every $x \in \mathbb{R}^N$, so $prox_f$ is well-defined. Thus, proximity operators perform a regularized minimization of the function f, and they are useful because they create a parameter that is a minimizer of equation if for any $gamma > 0$, [47] [63]. The minimizer is demonstrated in **equation E.7**.

$$x^* \;=\; prox_{\gamma(f_1+f_2)}\,(x^*) \tag{E.7}$$

Thus, a proximal splitting algorithm is applied, the term splitting comes from the fact that this method doesn't evaluate directly the proximity operator $prox_{\gamma(f_1+f_2)}(x^*)$, but tries to find a solution to **equation E.7** through sequences of computations involving the proximity operators of the functions separately, [63].

The method applied divides the **equation E.5** into a smaller problem in order to make it easier to solve. **Equation E.5** is composed by two sub-problems which will be solved by its proximity operator, as demonstrated in **equation E.7**. First, the prior that can be TV or Sobolev will be minimized, which is represented in the **equation E.5** by $\|x\|_{method}$, and the second step will be to perform the projection on the fidelity term B2-ball, which is the space of point x satisfying $\|Ax-y\|_2 \;\leq\; \sqrt{N}\delta$.

The first step is the prior norm, which is represented by f_1 taking the notation used in **equation E.5**, this way, $f_1(x) \;=\; \lambda\|x\|_{method}$, where the method can be Sobolev and Total variation. The proximity operator of f_1 is given in **equation E.8**, [63].

$$prox_{f_1,\lambda}\,(z) \;= \underset{z}{\operatorname{argmin}}\;\; \frac{1}{2}\,\|x-y\|_2^2 \;+\; \lambda\|z\|_{method} \tag{E.8}$$

The second step is to minimize f_2 which is represented by the constraint presented in the **equation E.5**, $\|Ax-y\|_2 \;\leq\; \sqrt{N}\delta$. Proximity operators provide a framework to handle constrains using indicative functions, which asserts if the term x belongs to a set C defined by $\|Ax-y\|_2 \leq \sqrt{N}\delta$, [63]. This function has just two outputs values, given in **equation E.9**.

$$i_C \;:\; \mathbb{R}^L \;\to\; \{0,+\infty\} \;\;:\;\; x \mapsto \begin{cases} 0 & \text{if x} \in C \\ +\infty & \text{otherwise} \end{cases} \tag{E.9}$$

The proximity operator of f_2 is given in **equation E.10**.

$$prox_{f_2,\lambda}(z) \;=\; \underset{x}{\operatorname{argmin}}\;\; \frac{1}{2}\|x-z\|_2^2 \;+\; i_c(x) \tag{E.10}$$

This problem has an identical solution as the **equation E.11**.

$$\underset{z}{\text{argmin}} \quad \|x - z\|_2^2 \qquad \text{subject to} \quad \|Az - y\|_2 \leq \delta \tag{E.11}$$

Equation E.11 is a projection on the B2-ball, which, as stated, consists in the set of points that satisfy the constrain $\|Ax - y\|_2 \leq \delta$.

Following the methods used in this research project, a comparison of the two Inpainting approaches will be made which is presented in the Appendix. In this process it will be shown how the two methods showed very similar results, however the computing time of the Inpainting using Sobolev and Total Variation as a constrained problem is much lower than when using the Inpainting as a non-constrained problem.

Appendix F

Comparison between the Inpainting algorithms

As mentioned, the algorithms were applied in two situations: presence and no presence of noise. To compare the two methods the image used to test and compare the two approaches was the Simulated phantom image. The standard Inpainting problem refers to the Inpainting method as a non-constrained problem, and the Inpainting problem using the UNLocBoX toolbox refers to the Inpainting problem as a constrained problem, as explained in the previous chapter. All these simulations were made in grayscale images and the image chosen to perform these tests is presented in **Figure B.2a**.

A mask was applied to the image, and since the final purpose of this work is to compare all the methods, that meant that the mask had to have three channels, that is, 1/3 of the sub-mask values is 1. Thus, when multiplied the mask by the image, the final image will have 1/3 of information. The construction of the mask was made randomly, which means that the mask didn't have a specific pattern and since the generating function used to produce the random pattern never created the same one, each method was repeated 10 times. The results presented in this section correspond to the average of the 10 acquisition repetitions.

Table F.1 presents the evaluation values calculated between the original image, and the image that resulted from the Inpainting algorithm.

Table F.1: Comparison of two Inpainting approaches with no presence of noise

Methods		**SNR**	**MSSIM**	**PSNR**
Standard Inpainting problem	Total Variation method	17.099	0.8981	31.283
	Sobolev method	17.457	0.9049	31.642
Inpainting problem using UNLocBoX toolbox	Total Variation method	16.341	0.8917	30.532
	Sobolev method	17.305	0.9037	31.490

In the noise situation, as demonstrated and explained in the procedure section, an input SNR was introduced in order to calculate the sigma value, which controls the level of noise. For the purpose of comparing the two algorithms, it was chosen a good input SNR which causes a small sigma, and therefore the image submitted to the Inpainting method will be of reasonable quality. In this situation, **Table F.1** demonstrates that the evaluation parameters resulting from the two Inpainting approaches have shown to be very similar. When comparing the values acquired from the two approaches in the Total Variation method, one can notice small difference

in the three evaluation parameters. The same observation can be made in the Inpainting Sobolev method. Thus, in the noiseless case, it is almost possible to say that the two approaches achieve the same result. The difference between them is that in the UNLockBoX the user doesn't need to study and analyse which better tau value should be used.

As stated, in the first Inpainting approach, a study of the parameters was needed, thus several simulations were made in order to find the best ones. First the value of τ was checked, and then several attempts in the value of lambda, λ, were also made. **Figure F.1** and **Figure F.2** is the graphic representation of the variation of SNR with the lambda change.

Figure F.1 and **Figure F.2** were taken from the software Matlab. **Figure F.1** is a graphic representation of the performance evaluation variation, of Inpainting using Total Variation Minimization, with 161 lambda values. The range of lambda values was reached after several attempts. One of the concerns taken into account was that the range of lambda values had to include the lambda value whose image had higher quality. For the Total variation method, the range of lambda value was between 2 and 18, with a step-size of 0.1, this way 161 lambda values were evaluated. For the Sobolev method, the range of lambda used was between 0.01 and 0.8 with a step-size of 0.005, thus 159 lambda values were evaluated.**Figure F.1** and **Figure F.2** shows the variation of the lambda values concerning the Inpainting using Total Variation and Sobolev minimization, respectively.

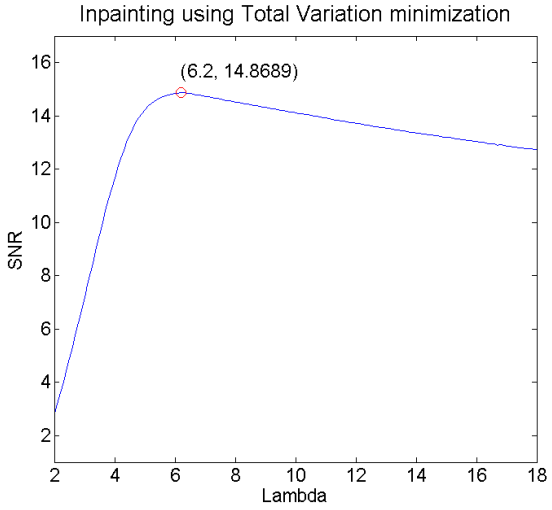

Figure F.1: Graphic representation of the variation between the image quality of the inpainted images and the λ parameter. The Inpainting method used is Inpainting as a non-constrained problem that uses the Total Variation Minimization

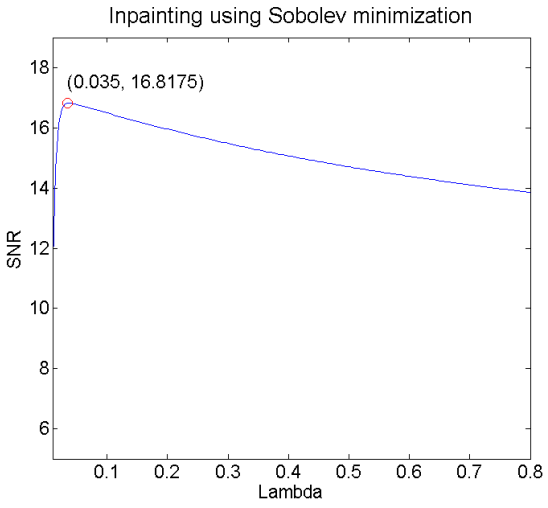

Figure F.2: Graphic representation of the variation between the image quality of the inpainted images and the λ parameter. The Inpainting method used is Inpainting as a non-constrained problem that uses the Sobolev Minimization

In the Inpainting using the Total Variation method, the lambda that presented best SNR value was 6.2, and in the Sobolev method the lambda was 0.035. The Sobolev method achieved the best lambda value that corresponds to a better image quality much faster.

Table F.2 presents the evaluation parameters that result from comparing the two images; the original and the inpainted image.

Table F.2: Comparison of two Inpainting approaches in the presence of noise

Methods		**SNR**	**MSSIM**	**PSNR**
Standard Inpainting problem	Total Variation method	14.875	0.8279	29.059
	Sobolev method	16.817	0.8804	31.0026
Inpainting problem using UNLocBoX toolbox	Total Variation method	16.119	0.8690	30.307
	Sobolev method	16.970	0.8804	31.115

The Sobolev method using UNLocBoX toolbox presents the best results compared to the Total Variation, and when compared to the standard Sobolev method, the difference is notorious. In the noisy case, the conclusion that it is taken is that the Inpainting method using the UNLocBoX presents the best results.

The study of the two Inpainting approaches was made in order to observe which one of the achieved images will have higher quality and how different the results from these two approaches would be. The results shown on **Table F.1** and **Table F.2** proved not to be so different; nonetheless in the noisy case the UnLOCk toolbox presents better results. The computing time of both approaches is long, however in the Inpainting method using the toolbox, the user doesn't need to analyse and find the best parameters, which in itself saves a lot of time.

Since the results are equivalent and it is easier to use the toolbox, the results concerning Inpainting will be achieved using the UnLOcK toolbox.